EXPERIMENTAL INVESTIGATION OF NONEQUILIBRIUM AND SEPARATION SCALING IN DOUBLE-WEDGE AND DOUBLE-CONE GEOMETRIES

BY

ANDREW MARSHALL KNISELY

DISSERTATION

Submitted in partial fulfillment of the requirements
for the degree of Doctor of Philosophy in Aerospace Engineering
in the Graduate College of the
University of Illinois at Urbana-Champaign, 2016

Urbana, Illinois

Doctoral Committee:

Associate Professor Joanna Austin, Director
Professor J. Craig Dutton, Chair
Assistant Professor Marco Panesi
Associate Professor Tonghun Lee

ABSTRACT

Experiments were performed in the Hypervelocity Expansion Tube (HET) and the T5 hypervelocity shock tunnel to investigate geometric and gas composition effects on a double-wedge and double-cone geometry. The high-speed flow over the models results in a complex shock boundary-layer interaction which is known to be sensitive to thermal and chemical nonequilibrium. High-speed shadowgraph and surface heat flux measurements are obtained for both geometries. Surface heat flux measurements of the laminar boundary layer for the double-wedge show good agreement between both facilities with proper nondimensionalization. High-speed shadowgraph imaging is used to study the flowfield startup processes. The shock interactions and separation location exhibit no transient processes once the nozzle reservoir reaches a steady stagnation pressure level in T5. Two of the primary shock-shock interaction types are identified for the double-cone. Augmented heat flux is observed for the Edney Type V interactions with the highest peak heating observed with the nitrogen test gas. However, transient heat flux measurements during the nozzle startup indicate that the peak heat flux is not captured by the thermocouples for the air case due to the highly local nature of heating in this shock configuration.

The boundary-layer separation scaling based on triple-deck theory for a double-wedge is applied to the double-cone geometry. The pressure correlation for the double-cone is found to be in agreement with historical results. No significant response of the separation length to the gas composition, apart from changes in the freestream condition, are observed for the current experiments. In purely laminar interactions no dependence of the scaled separation on Reynolds number is observed. Reattachment heat flux indicates transitional behavior of the separated boundary layer for the high

Reynolds number conditions. A consistent decrease in scaled separation length is found for transitional interactions.

ACKNOWLEDGMENTS

Thanks first goes to my advisor, Professor Joanna Austin. From my initial summer REU position through today you have given me many great opportunities and guidance through my graduate career. Next, I'd like to thank my committee members Professors Craig Dutten, Marco Panesi, and Tonghun Lee for taking the time to provide guidance, suggestions, and critiques of this work. I would also like to thank Professor Hans Hornung at Caltech for sharing his incredible wealth of knowledge about all things related to high-speed gas dynamics.

Thanks goes to my friends and classmates at Illinois. Special thanks goes to Bill Flaherty, Ryan Fontaine, and Andy Swantek who have been great friends, colleagues, and mentors. From teaching me to run the HET to helping with a new diagnostic, I would not be the experimentalist I am today without their help. Also thanks to Todd Reedy, Tommy Herges, and Manu Sharma for help in and around different facilities, learning about high-speed gas dynamics, and debugging MATLAB scripts. Galina Shpuntova and Matt Leibowitz, not only have I had the pleasure of working with you but you have been a strong source of support as we made the trek out West. To everyone else from Illinois that I have had the pleasure of knowing, you have all been great friends both in and out of work.

I want to thank all of the wonderful people I have meet at Caltech with special mention of three individuals. Bryan Schmidt, it was great working with you and getting to know your family and I am very grateful for your assistance in getting T5 operational again. Thanks also to Joe Jewell who spent many hours talking with me as I worked to recommission T5 and understand the underlying physics of the facility. Lastly, the success of this work would not have been possible without the tireless help

of Bahram Valiferdowsi in keeping T5 up and running.

I want to thank my parents for their unwavering support throughout my life. Mom and Dad, you have challenged me to always do my best both in and out of school and never give up no matter what issue may arise. To my brothers, Ben and Joey, I am always so grateful when we find time to get together and I wish you both the best of luck as you both embark on your own new adventures.

Lastly, to Christina, without your love and support I would never have had the courage to finish.

TABLE OF CONTENTS

LIST OF TABLES

LIST OF FIGURES

CHAPTER 1

INTRODUCTION

1.1 Background

Hypersonic shock boundary-layer interactions involve complex interactions between various viscous and inviscid processes [1, 2]. These interactions are of both academic and practical interest as these interaction are very common on high-speed air breathing and re-entry type vehicles, such as the Boeing X-51 [3]. Shock boundary-layer interactions introduce difficulties to the design and control of these vehicles due to potential flow unsteadiness and high levels of peak heating. Thus it is imperative to be able to make accurate predictions of both pressure and heat flux loads on the vehicle surfaces.

The model problem presented is high-stagnation-enthalpy hypervelocity flow over a double-wedge and double-cone geometry. A diagram of the flowfield is shown in Figure 1.1. An incoming laminar boundary layer interacts with a shock system formed by the interaction of an oblique and bow shock. The flow separates forming a complex shock dominated turbulent flow with impingement on the surface. Additional reactions are occurring due to the high temperatures behind the bow shock and in the shock impingement region. This shock-boundary-layer interaction is known to be very sensitive to the thermochemical state of the gas [4–6]. This strong coupling between thermochemistry and shock boundary layer interaction makes the double-wedge and double-cone sensitive test cases for model development [3, 7]. Experiments and numerical simulations have been completed on double-cone and double-wedge flows with the same freestream conditions. Good agreement between experiments and simulations have been found at low enthalpy conditions while poor agreement is

seen at high enthalpy conditions [5–7]. A more detailed overview of these studies is made in the following paragraphs.

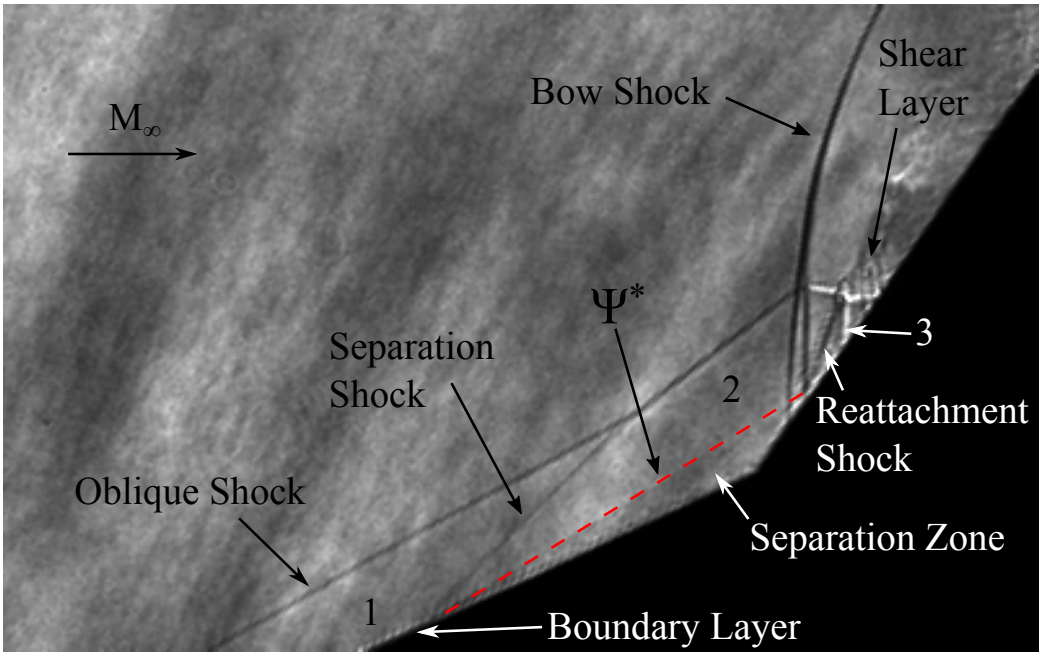

Figure 1.1: Diagram of the flow structure for the double-cone.

Thermochemical nonequilibrium has been identified as one of the key components of the double-wedge and double-cone flow field. Thermochemical nonequilibrium is the umbrella term used to describe chemical and vibrational nonequilibrium characteristics of hypersonic flows. A simple description of the terms is given here. These conditions can be explained by considering the relaxation region behind a normal shock in front of a body in high-speed flow. The normal shock causes an instantaneous increase in temperature, pressure and density. If the shock is sufficiently strong, the post-shock gas will undergo chemical reactions leading to a drop in temperature and an increase in pressure and density. This region of chemical activity is known as the relaxation region. If the distance between the shock and the body is sufficiently larger than the relaxation distance, the gas can be considered to be in equilibrium. The flow is considered to be frozen if the opposite scenario exists, that is the relaxation length is much longer than distance between the shock and the model. In this case the gas has no time for reactions to occur before interacting with

another body. Chemical nonequilibrium exists in the region bounded by frozen and equilibrium conditions. This third case exists when these two length scales are on the same order and now the rate of chemical reactions is required in order to make accurate predictions to the chemical state of the gas. Additionally, the vibrational state of the gas changes at a finite rate due to the transfer of energy by molecular collisions. When the gas temperature jumps dues to the shock, collisions between the molecules redistribute the energy into the vibrational modes. If the gas is given a sufficient length of time, the vibrational energy reaches its equilibrium state. Vibrational nonequilibrium exists in the time during which the vibrational energy is changing. Chemical and vibrational nonequilibrium may be present simultaneously. Additionally, coupling between the two exists, e.g., dissociation rates may be higher for vibrationally exited gases.

Computational and experimental work using the double-cone and double-wedge geometry have focused on improving thermochemical models such that accurate simulations can be made. Previous double-wedge work has shown discrepancies between the size of the separation and an under-prediction of pressure levels between experimental and simulations [8]. Nitrogen dissociation rates could not solely account for the discrepancies and other issues such as freestream modeling, spanwise effects, or unsteadiness were offered as possible explanations. Double-cone studies were completed to remove issues related to the double-wedge geometry [9]. These two studies showed that equilibrium nitrogen dissociation rates for realistic geometries in hypersonic flows were not modeled well. Additionally, nonequilibrium nitrogen dissociation rates were also not well modeled due to poor vibration-dissociation coupling models [9]. In addition to the vibrational-dissociation models, freestream vibrational freezing must be considered to accurately compare simulations with experimental results [5]. The addition of oxygen to the flow field introduces many chemical reactions and species such as NO. Non-Boltzmann distributions of NO have been seen in reacting regions through the second Zel'dovich mechanism [10]. Additionally, poor prediction of oxygen recombination has been theorized as another possible reason for discrepancy at higher-enthalpy air flows [11].

Shock interaction types between an oblique shock and cylinder bow shock were first extensively defined by Edney [12]. In this paper Edney studied augmented heat flux and pressure levels on a cylinder with an oblique shock impingement. The shock interactions were classified into six main groups, Types I-VI. Sanderson [13] studied nonequilibrium effects due to thermochemistry for this flowfield. Olejniczak et al. [14] performed inviscid simulations of a double-wedge and was able to observe four of the shock interaction types. However, there are differences in the interaction structures observed by Olejniczak compared to the interactions as defined by Edney due to constraints placed on the flow by the model geometry. Experimental measurements at low Reynolds number of the double-cone flowfield in a hypersonic blowdown facility showed good agreement with laminar simulations for the separation size and interaction type [15]. Higher enthalpy double-wedge and double-cone experiments have also made observations of the different shock interaction types [16, 17]. Jangadeesh et al. [16] observed unsteady flow for high deflection angles with a double-cone. A type V interaction was observed for a 25°–50° double-cone.

A scaling law for the separated boundary layer of a double-wedge has been developed by Davis and Sturtevant [4]. This scaling law is built by applying triple-deck theory to a base-flow model. The base flow model, introduced by Roshko [18], describes the application of a theory of pressure rise through a shear layer by Sychev [19]. Triple-deck theory has been studied extensively by Stewartson and Williams and describes the region near a boundary layer that separates due to a disturbance in the flow field [20, 21]. Triple-deck theory has also been studied for other geometries such as two-dimensional compression corners and axisymmetric geometries. Rizzetta, Burggraf and Jenson studied separation of boundary layers at two-dimensional compression corners [22]. They note that corner angle, α^*, must be $O(Re^{-1/4})$ for the simplified triple deck formulation to hold. When the angle is smaller, separation does not occur and when the angle is larger a more complicated structure forms, which has been previously analyzed by Burggraf [23]. Triple-deck theory applied to axisymmetric bodies has been studied with applications to cylinders and flared cones [24–28]. Flared cylinders have been the focus of several of these studies [24,25,28]. A brief con-

sideration of geometries with inclined forebodies such as the double-cone was made by Huang and Inger [25].

One important consideration to make is whether three-dimensional effects have an impact on a nominally two-dimensional flow field, such as a planar compression corner. Experimental and theoretical studies of hypersonic compression corners were completed by Holden and Moselle [29]. Two-dimensional flow was determined by observing successively wider models until no change in measurements at the centerline was observed. Rudy et al. [30] completed two-dimensional simulations of the Holden and Moselle experiments. They find that two-dimensional computations do not match the experimental results for highly-separated flow fields. Three-dimensional simulations completed match both the separation length and the time to steady flow indicating that spanwise effects may be important in a nominally two-dimensional flow field. However, simulations completed by Lee and Lewis [31] show that two-dimensional simulations are able to replicate the experimental and three-dimensional simulation results. Hypersonic high enthalpy shock boundary layer interactions in compression corners have been studied by Mallinson, Gai and Mudford [32, 33]. They also note that two-dimensional flow can be achieved even for highly-separated flows.

1.2 Overview of Current Work

The previous work discussed above has shown that thermochemistry and geometry can significantly affect the hypersonic shock-bondary layer interaction over a double-wedge and double-cone geometry. At the conditions being studied the thermochemical effects of oxygen chemistry can be isolated by switching between air and nitrogen test gas. The current work evaluates the effects of gas composition on both viscous and inviscid flow features. Special consideration is taken to study effects on flow establishment and steadiness. The second main goal of the project will be to determine the role of an axisymmetric body-geometry on this scaling parameter. The separation scaling parameter developed previously for the double-wedge geometry is built on an asymptotic theory which assumes a planar flow field. A key component of the

scaling is the incorporation of triple-deck asymptotic theory. This framework will be examined for a double-cone using experimental measurements in two facilities.

Chapter 2 describes the experimental methods used in this study. This includes the model design, facility descriptions, diagnostic techniques used, and the details of flow conditions. Chapter 3 includes analysis of the flow startup and of shock structures through high-speed shadowgraph. Chapter 4 summarizes the heat flux results for the double-wedge and double-cone. Chapter 5 includes an analysis of the separation scaling. Lastly, Chapter 6 contains the conclusions and summary of the work completed.

CHAPTER 2

EXPERIMENTAL SETUP

The model geometries studied and the experimental facilities used are described in this chapter. Details' on both facilities capabilities and operation are provided. The freestream conditions are reported with an explanation of the methods used for their calculation. The measurement techniques used to collect data are described with focus on the setup and equipment used.

2.1 Model Geometries

Two model geometries, a double-wedge and double-cone are used. These geometries were initially chosen due to their historical significance allowing for comparisons to be made with previous experimental and numerical studies.

2.1.1 Double-Wedge

The double-wedge model is a fore wedge angle of 30° and aft wedge angle of 55°. The primary model has a front face length of 50.8 mm, aft face length of 25.4 mm, and span length of 101.6 mm. An image of the double-wedge model is shown in Figure 2.1. The double-wedge is machined from A2 tool steel and is constructed from two parts to allow for easy internal access for thermocouple installation. The double-wedge model was used for tests in the HET and T5. Additional details on the design and construction of the double-wedge model may be found in Swantek [17].

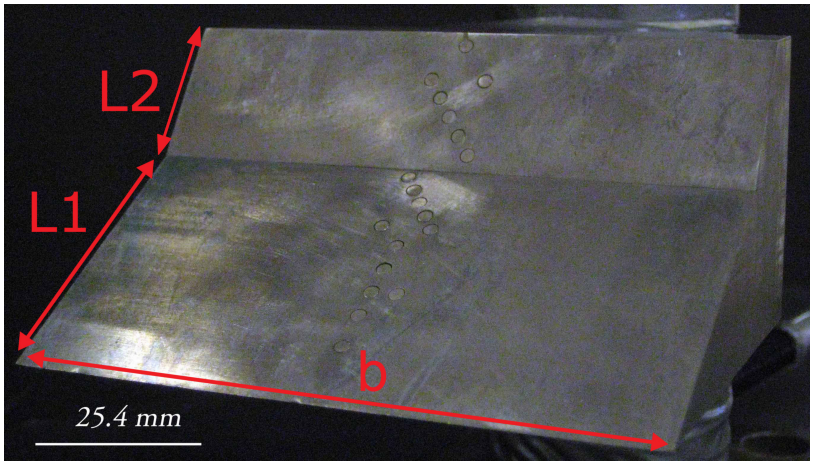

Figure 2.1: Image of double-wedge model. The model is shown before the installation of additional thermocouples for the T5 tests. Image courtesy of Swantek [17].

2.1.2 Double-Cone

The second model geometry used is the double-cone. Two double-cone geometries are used in this study with the primary cone geometry having a front half-angle of 25° and aft half-angle of 55°. The double-cone geometry was chosen to eliminate finite span effects inherent to the double-wedge model.

The 25-55 double-cone model is based on the design of Nompelis et al. [5] Two physical models of this double-cone are used for this work. The first model, constructed by Swantek [34], was used in the HET. This model has a first base diameter of 25 mm and a second base diameter of 63.5 mm. The model is made from A2 tool steel and assembled from two parts to avoid any curvature at the hinge location. No thermocouples are instrumented into the model due to space constraints.

The second 25-55 double-cone model was machined for use in T5. This double-cone model is an enlarged scale model of the HET version. The T5 model has a first base diameter of 48.2 mm and a second base diameter of 122.3 mm, shown in Figure 2.2. The size of the model was increased from the HET double-cone so that thermocouples can be installed into the model. A total of 64 thermocouples are installed to allow for heat flux measurements. The tip is made from molybdenum and is designed to be replaceable in case of damage or wear due to the high heat flux loads present at

the tip.

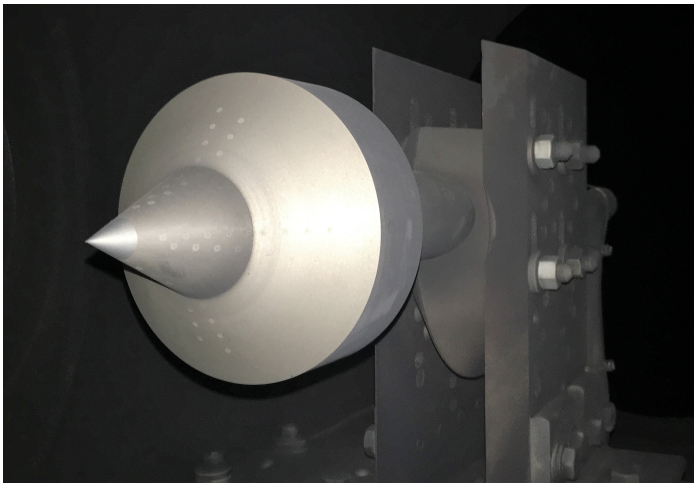

Figure 2.2: T5 25-55 double-cone installed in the test section.

The second double-cone geometry used in T5 has a fore cone half-angle of 25° and aft cone angle of 48°. The first and second base diameters of this model are the same as the other T5 double-cone model. By maintaining the same fore cone geometry, the effects due to reduced flap angle on the triple point interaction and reattachment shock can be isolated. Additionally, thermocouples are only installed onto the aft cone since the fore cone geometry has remained unchanged. Both T5 double-cone models are installed inline with the nozzle axis and with a measured pitch of less than ±0.1°. Through this work both double-cone models will be referenced based on the fore and aft cone half-angles, i.e. the 25-55 double-cone or 25-48 double cone.

2.2 Facility

Experiments are completed in two facilities: the Hypervelocity Expansion Tube (HET) and the T5 free-piston driven reflected-shock tunnel.

2.2.1 HET

An expansion tube is an impulse facility that uses a novel method of gas acceleration to obtain a thermo-chemically clean hypervelocity freestream. The HET is capable

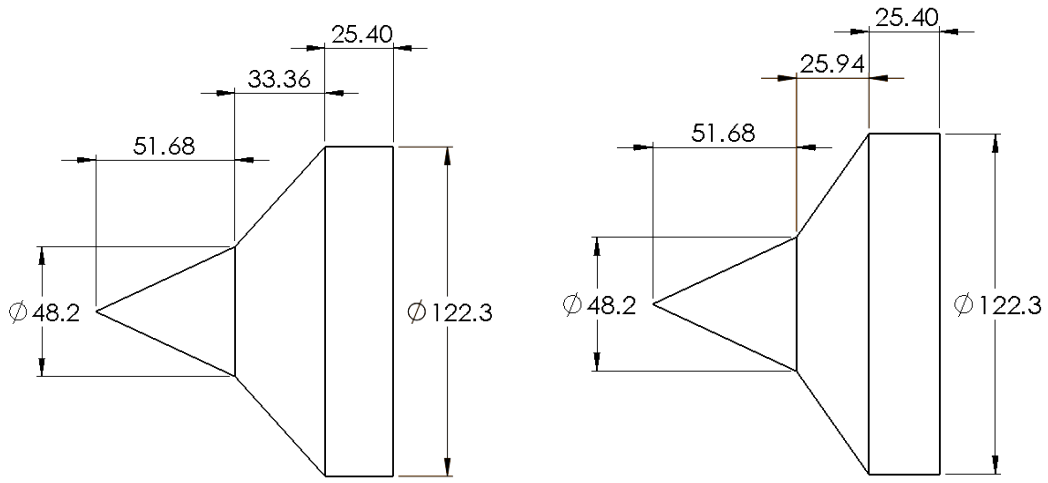

(a) 25-48 Double-Cone (b) 25-55 Double-Cone

Figure 2.3: Diagrams of the 25-48 and 25-55 T5 double-cone models. Dimensions are given in mm.

of obtaining a range of freestream conditions with Mach numbers from 3 to 7.5 and stagnation enthalpies of 2 to 9 MJ/kg. The HET consists of three sections: a driver, driven, and expansion section. The total length of the HET is 9.14 m with an inner diameter of 152 mm and is constructed of 304/304L stainless steel. Two final sections, the test section and dump tank, are located downstream of the expansion section. The models are installed into the test section which connects to the expansion section through a sliding seal. An image of the facility from the test section is seen in Figure 2.4.

The driver and driven sections are separated by an aluminum diaphragm. This diaphragm is made from 5052 aluminum and is varied in thickness to change the driver gas burst pressure. The primary diaphragm ruptures naturally as the driver section is filled with gas, typically helium, which presses the diaphragm against a set of knife blades. Using the knife blades increases the shot-to-shot repeatability and prevents metal shards from detaching and damaging the facility and models downstream. The rupture of the primary diaphragm causes a strong shock wave to travel down the driven section, compressing and accelerating the test gas. The expansion section is initially separated from the driven section by a thin mylar diaphragm. When ruptured

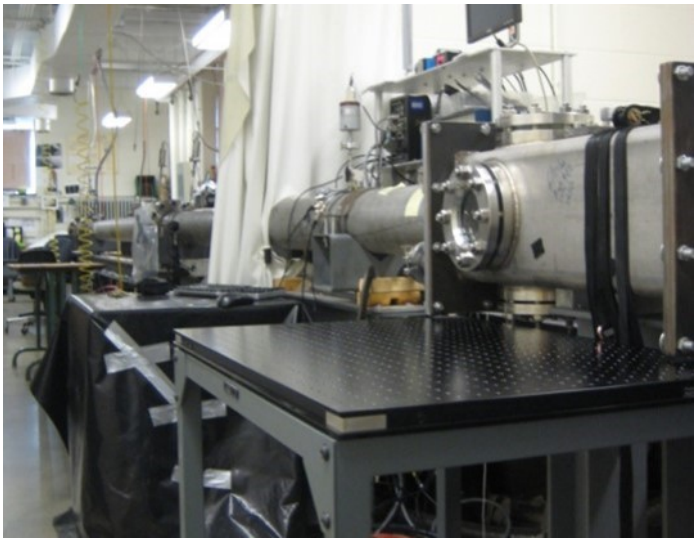

Figure 2.4: Image of HET looking upstream from test section.

by the incident shock, a transmitted shock and unsteady expansion fan form. The unsteady expansion fan further accelerates the shocked test gas to the test condition. The test gas then exits the tube into a test section which has optical access from three sides. Additional details of the facility design, construction, operation and characterization are found in Dufrene, Sharma, and Austin [35].

The HET data acquisition (DAQ) system is comprised of two PXI-6133 data acquisition cards housed in a PXI-1031 chassis. The PXI-6133 card is capable of 8 simultaneous analog inputs with acquisition rates up to 2.5 MHz at 14-bit resolution. Data is recorded at 1 MHz for 30 ms with a pretrigger time of 12 ms. Each DAQ card is connected to a BNC-2110 block which is used to connect with the pressure transducers and heat flux gauges. The DAQ system is controlled through an NI Labview VI running on a Microsoft Windows system. The driver pressure is recorded using a Setra Model 206 pressure sensor. A total of four PCB 113A26 piezoelectric pressure transducers are installed along the tube to measure wave speeds and as a secondary method for triggering the DAQ system. Three MKS capacitance manometers are used to measure the vacuum levels in the driven and expansion section. These three gauges are only used before the experiment is run and are not recorded due to the possibility of damage from the primary shock wave. An additional PCB 113A26 pres-

sure transducer is used in the test section as a pitot probe and is used as the primary trigger for the DAQ system.

2.2.2 T5

The T5 free-piston reflected shock tunnel is another impulse facility that is able to produce a hypervelocity freestream. The two facilities are able to produce overlapping freesteam conditions while utilizing different gas acceleration methods. The T5 facility utilizes a piston to adiabatically compress a helium/argon mixture to high pressure which acts as the driver to a reflected shock tunnel [36]. The facility consists of five main sections: the compression tube, secondary reservoir, shock tube, test section, and dump tank. A diagram of the facility is shown in Figure 2.5. A stainless steel diaphragm initially separates the compression tube and shock tube. This diaphragm is pre-scored to a prescribed depth based on previous experiments to achieve a repeatable burst pressure. The scoring also ensures that the diaphragm breaks in a predictable manner and that no metal petals become detached. A nozzle is located at the other end of the shock tube and slides into the test section. A thin mylar diaphram located within the nozzle throat region is used to separate the shock tube from the test section and dump tank.

To run an experiment, a 120 kg piston in loaded into the end of the compression tube and the entire facility is initially evacuated using a combination of vacuum pumps. The shock tube is then filled with the test gas, typically air, nitrogen, carbon-dioxide or some mixture thereof. The compression tube is filled with a helium/argon gas mixture and the secondary reservoir is filled with compressed air. Once the pressures are set, a fast acting valve, located between the compression tube and secondary reservoir, is opened which allows the compressed gas to empty into the piston space located behind the piston causing it to accelerate down the compression tube. The piston adiabatically compresses the helium/argon mixture in front of it and once the gas reaches a sufficiently high pressure the primary diaphragm bursts, forming a strong shock that travels down the shock tube. The primary shock reflects from the

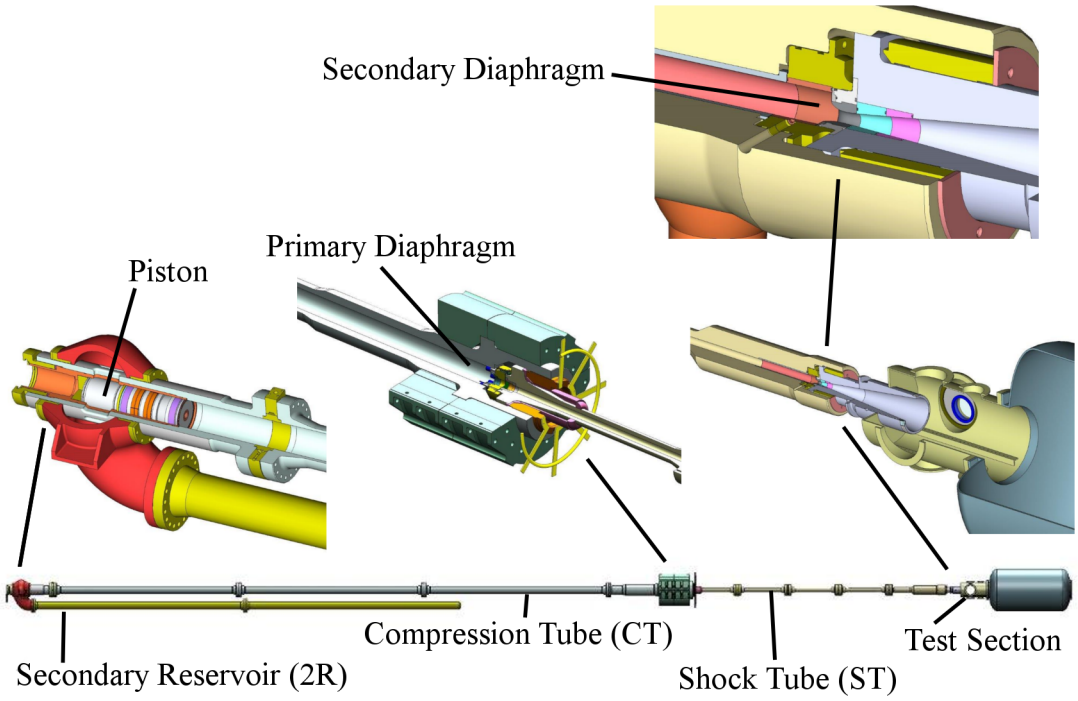

Figure 2.5: Labeled diagram of T5.

end wall forming a high-temperature, high-pressure reservoir of gas. The secondary diaphragm is vaporized by the primary shock and the stagnated gas expands through the nozzle to the final test condition and interacts with the model. The converging-diverging nozzle has a contoured profile with nominal area ratio of 100:1.

The facility is monitored through a series of vacuum gauges and pressure transducers. A total of eight PCB 119M44 dynamic pressure transducers are located along the compression tube and shock tube. Two pressure transducers are located just ahead of the primary diaphragm to measure the burst pressure. A series of four transducers are located along the shock tube to measure the primary shock speed. The final two transducers, located at stations 3 and 4, are used to determine the primary shock speed. An example of the response of the shock timing transducers is shown in Figure 2.6. The other two stations are not used as there is a decrease in shock speed of approximately 15% from the speed measured between stations 1 and 2 to stations 3 and 4. Lastly, two pressure transducers are located just upstream of the nozzle to

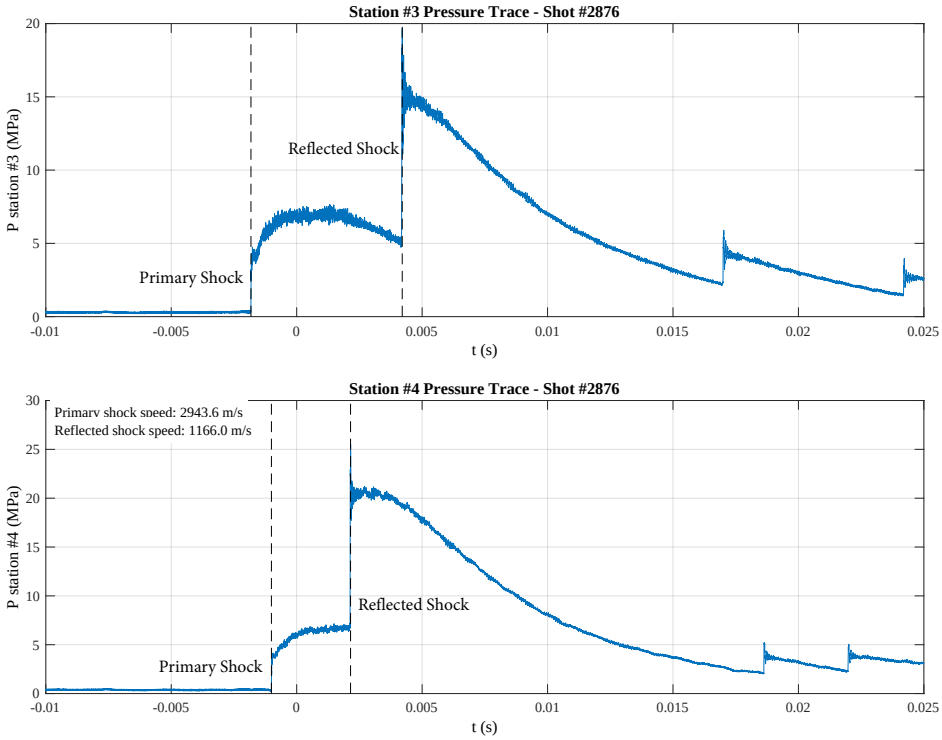

Figure 2.6: Shock Timing Pressure Transducers, Shot 2876

measure the nozzle reservoir pressure with an example of the pressure trace shown in Figure 2.7. The values for these eight pressure transducers are recorded by the DAQ system. The freestream parameters for each run are determined using the measured shock speed and the nozzle reservoir pressure, detailed below in Section 2.3. Vacuum gauges are located along the facility to measure vacuum levels during the pump down process and are isolated from the facility during the run to prevent damage. Static pressure transducers located at the shock tube, compression tube, and secondary reservoir are used when filling the facility. They are also isolated during the run and not recorded by the DAQ system. The fill pressures are written down on the checklist.

The T5 DAQ system was overhauled during the course of this work. The previous DAQ system was a conglomeration of DSP Technology and National Instruments (NI) hardware. This necessitated running two data acquisition programs simultaneously

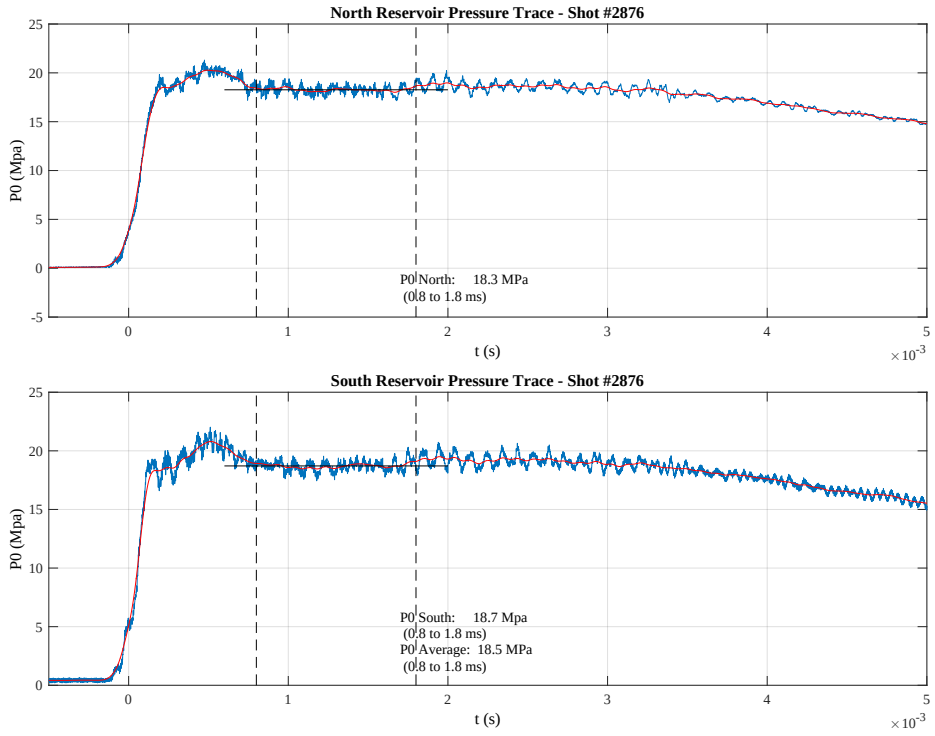

Figure 2.7: Nozzle Reservoir Pressure Transducers, Shot 2876

and added unnecessary complexity to the data reduction process. A new NI chassis and set of PXIe data acquisition cards were purchased to replace the DSP Technology hardware. The new NI system consisted of six PXIe-6368 data acquisition devices housed in a PXIe-1075 chassis. Each PXIe-6368 is capable of acquiring 16 simultaneous analog input measurements up to a rate of 2 MHz with 16-bit resolution. Each card is connected to two BNC-2110 connection blocks. This system is used to collect signals from all of the dynamic pressure transducers used in the facility. It is also used for heat flux measurements if more than 48 thermocouples are installed in the model.

The second, previously existing NI system consisted of 12 PXI-6115 data acquisition devices housed in a PXI-1045 chassis. Each PXI-6115 card is capable of acquiring 4 simultaneous analog input measurements at a rate of 10 MHz with 12-bit resolution.

Each card is connected to one BNC-2110 connection block. This second system is used exclusively for the thermocouple measurements. Two custom built thermocouple amplifiers, each with 48 amplification channels are used. Each amplifier has a user selectable gain of up to 100. For this work, both chassis acquired data at 1 MHz for 30 ms. The data is centered around the primary shock nozzle endwall reflection. Both chassis are controlled through a single NI Labview VI running on a Microsoft Windows system.

The two facilities complement each other and offer overlapping ranges of attainable test conditions. Both facilities are able to reach a range of conditions based on the initial fill pressures of each section and different gas compositions can be used as the test gas for both facilities. However, each facility has its own set of strengths and weaknesses which must be considered when deciding which facility to use for a given study. One of the main benefits of the HET over T5 is that chemical and thermal nonequilibrium in the freestream are minimized due to the method of gas acceleration. The HET uses a single shock and unsteady expansion to reach the test condition. In T5, a reflected shock is used, forming the high-temperature, high-pressure reservoir, which may result in substantial dissociation and vibrational excitation of the gas. The hot, dissociated reservoir gas then expands through a nozzle while the HET does not use a nozzle. As the gas expands through the nozzle, the temperature drops and recombination occurs. However at a certain point the density may drop sufficiently low enough that recombination is no longer able to occur at a fast enough rate and the chemical composition "freezes" to a nonequilibrium composition. The freestream composition is predicted for T5 using the nozzle code but the simulated composition is dependent on having an accurate chemical model.

The HET also has the benefit of being able to be operated by one researcher with each test taking approximately 90 minutes to complete. T5 takes a significantly greater investment in time and money on a per shot basis. A minimum of two people are required to physically run the experiment. The turnaround time of the facility is also significantly longer due to the extensive cleaning required of the nozzle and shock tube, resulting in only one test per day completed on average. Details of the

cleaning procedure are explained by Jewell [37].

However, the HET has several notable disadvantages compared with T5. The models used in the HET are limited in both size and length. In the HET the transmitted shock that precedes the test gas forms a boundary layer in the expansion section. This boundary layer can grow to a significant size and limits the model width to be smaller than the diameter of the tube. The model length is also constrained due to the shorter test time as enough test time must exist for a mean flow to establish. T5 test times are on the order of 1 ms to 2 ms which allows for longer models. Additionally the maximum allowable model size is greatly expanded due to the larger exit diameter of the T5 nozzle compared to the HET. One last benefit of T5 is the much higher stagnation enthalpies that can be achieved.

2.3 Run Condition Selection

The HET is able to achieve a range of stagnation enthalpies and freestream Mach numbers. The current work was completed at one nominal run condition with two test gas compositions. However, the naming scheme introduced by Swantek [17] is used here to maintain continuity between the studies. The first number is in reference to the approximate value for the freestream Mach number and the second value is the approximate stagnation enthalpy. The freestream values are calculated assuming perfect gas and are shown in Table 2.1.

Table 2.1: Nominal HET run conditions.

Condition	P_∞ kPa	T_∞ K	ρ_∞ kg/m^3	U_∞ m/s	M_∞ –	Re_x 10^6/m	h_0 MJ/kg
M7_8 N2	0.784	700	0.00377	3821	7.08	0.440	8.03
M7_8 Air	0.781	709	0.00383	3812	7.14	0.427	7.98

Freestream conditions of shots completed in T5 are shown in Tables 2.2 and 2.3. The run condition in T5 was chosen to overlap the HET condition in order to study effects due to the difference in facility. The initial T5 experiments were completed

using the H8-Re2 conditions, indicating a stagnation enthalpy of 8 MJ/kg and a freestream unit Reynolds number of approximately 2×10^6. The stagnation enthalpy was chosen as the primary parameter to match between T5 and the HET resulting in a match between the freestream velocities. However, not all of the flow parameters can be matched between the two facilities, e.g. the T5 freestream conditions have an elevated pressure and density compared to the HET. A second run condition, the H8-Re6 conditions, was used in T5 with the double-cone models to study the effect of increased Reynolds number at a constant stagnation enthalpy. Air and nitrogen were used as tests gases with the double-wedge and double-cone. Carbon dioxide was used with the double-cone models exclusively.

Table 2.2: Nominal T5 run conditions. Conditions on a shot-by-shot basis are included in Appendix A.

Condition	P_∞ kPa	T_∞ K	$T_{v,\infty}$ K	ρ_∞ kg/m^3	U_∞ m/s	M_∞ –	Re_x 10^6/m	h_0 MJ/kg
H8-Re2 N2	4.5	768	3040	0.0195	3764	6.66	2.16	8.23
H8-Re2 Air	7.6	1108	1116	0.0235	3672	5.45	1.96	8.19
H8-Re2 CO2	12.3	1530	1530	0.0363	3032	4.41	1.95	8.25
H8-Re6 N2	15.7	866	2753	0.0610	3931	6.55	6.52	8.83
H8-Re6 Air	23.7	1117	1118	0.0733	3692	5.49	6.11	8.06

Table 2.3: Nominal T5 run conditions mass fractions. Values designated as '–' have mass fractions less than 1×10^{-9}.

Condition	Y_{N2}	Y_{O2}	Y_{NO}	Y_N	Y_O	Y_{CO2}	Y_{CO}
H8-Re2 N2	0.9980	–	–	2.044×10^{-3}	–	–	–
H8-Re2 Air	0.7317	0.1770	0.0758	–	1.547×10^{-2}	–	–
H8-Re2 CO2	–	0.1152	–	–	3.831×10^{-3}	0.6726	0.2084
H8-Re6 N2	0.9994	–	–	5.736×10^{-4}	–	–	–
H8-Re6 Air	0.7316	0.1883	0.0760	–	4.051×10^{-3}	–	–

The freestream conditions are calculated using a two step process. First, the post-reflect shock conditions are calculated through a MATLAB script using Cantera [38] and the SDToolbox [39]. The shock tube fill pressure, measured primary shock speed, and measured nozzle reservoir pressure are used as inputs into the script. To calculate

the reservoir conditions, an ideal reflected shock is assumed using the initial gas composition, fill pressure, and measured shock speed. The calculated reservoir gas pressure is then corrected to the measured reservoir pressure assuming an isentropic expansion. Further details of the T5 nozzle reservoir calculation may be found in Jewell [37].

The calculated reservoir conditions are then used as the initial conditions for the UMNAEM nozzle code [40]. The nozzle code solves the axisymmetric chemically-reactive, vibrationally-active, Navier-Stokes equations. The nozzle wall turbulent boundary layer is modeled using the Spalart-Allmaras turbulence model [41] with the Catris and Aupoix compressibility correction [42]. The invisicd fluxes are calculated using Steger-Warming flux splitting [43] with the van Leer limiter [44] giving second-order space accuracy. The implicit time-splitting DPLR method is used for time integration [45]. The structured nozzle grid contains 492 x 219 cells in the axial and radial directions respectively. Freestream values are extracted from the simulation after convergence along the nozzle centerline at the exit plane.

2.4 Diagnostics

A combination of surface measurements and optical diagnostics is used in this study.

2.4.1 Heat Flux

Surface heat flux measurements are made using fast-response coaxial thermocouples. The gauges were developed by Sanderson [13] for use in T5 and implemented into the HET by Flaherty [46]. The gauges are Type E (constantan-chromel) thermocouples and are flush mounted to the surface of the model. The gauges are made from two components with the outer electrode having a diameter of 2.4 mm and the inner electrode having a diameter of 0.635 mm. The contact area between the two electrodes over which the measurement is made has a diameter of 0.787 mm. The gauges have a response time on the order of 1 µs. A total of 19 gauges were originally installed in

the double-wedge model for the experiments completed in the HET. An additional 6 thermocouples have been installed for experiments completed in T5. Locations of the thermocouples are shown in Table 2.4. The new thermocouples used in the T5 tests are D1, D2, and I1-I4.

Table 2.4: Normalized location of coaxial thermocouples on the double-wedge model. Streamwise distance is normalized by the first wedge face length, L=50.8 mm, and x referenced to the leading edge and measured along the streamwise axis. The spanwise location is measured from the model centerline and normalized by the width of the model, W=101.6 mm.

TC #	Name	x/L	z/W
1	A	0.173	0
2	B	0.3031	0
3	C	0.390	0
4	C1	0.390	0.0405
5	D	0.476	0
6	D1	0.476	0.078
7	D2	0.476	0.15625
8	E	0.563	0
9	F	0.636	-0.0405
10	F1	0.636	0.0405
11	G	0.686	0.02025
12	H	0.736	0
13	I	0.786	-0.02025
14	I1	0.786	0.0625
15	I2	0.786	0.125
16	I3	0.786	0.1875
17	I4	0.786	0.25
18	J	0.837	-0.0405
19	K	0.900	0.04625
20	L	0.938	0.023
21	M	0.976	0
22	N	1.014	-0.023
23	O	1.052	-0.04625
24	O1	1.052	0.04625
25	P	1.123	0

A total of 64 thermocouples are installed into the T5 25-55 double-cone model with the locations shown in Table 2.5. The streamwise distance is measured along the cone surface for both the fore and aft cone thermocouples and referenced to the cone apex. The distances are normalized by the fore cone face length, L=56.97 mm. The gauges are installed radially in groups of 16 at four azimuthal angles. Thermocouples within each group are staggered along two azimuthal angles separated by 15° to allow for increased thermocouple density than what would possible if they were installed in a straight line. This pattern was chosen for gauge redundancy and to allow for azimuthal effects to be studied.

A total of 13 thermocouples are installed into the 25-48 double-cone model. Thermocouples are only installed on the aft cone as the fore cone remained the same

Table 2.5: Normalized location of coaxial thermocouples on the 25-55 double-cone model. Streamwise distance, s, is referenced to the cone apex and measured along the model surface and is normalized by the fore cone face length, L=56.97 mm. The azimuthal location is set with bank A at the top of the model and measured clockwise when facing the model.

Bank	TC #	s/L	θ (deg)	Bank	TC #	s/L	θ (deg)
A	1	0.4278	0	C	1	0.4278	180
A	2	0.4956	15	C	2	0.4956	195
A	3	0.5640	0	C	3	0.5640	180
A	4	0.6318	15	C	4	0.6318	195
A	5	0.7002	0	C	5	0.7002	180
A	6	0.7681	15	C	6	0.7681	195
A	7	0.8365	0	C	7	0.8365	180
A	8	0.9043	15	C	8	0.9043	195
A	9	0.9727	0	C	9	0.9727	180
A	10	1.0595	0	C	10	1.0595	180
A	11	1.1273	15	C	11	1.1273	195
A	12	1.1957	0	C	12	1.1957	180
A	13	1.2635	15	C	13	1.2635	195
A	14	1.3319	0	C	14	1.3319	180
A	15	1.3997	15	C	15	1.3997	195
A	16	1.4681	0	C	16	1.4681	180
B	1	0.4278	90	D	1	0.4278	270
B	2	0.4956	105	D	2	0.4956	285
B	3	0.5640	90	D	3	0.5640	270
B	4	0.6318	105	D	4	0.6318	285
B	5	0.7002	90	D	5	0.7002	270
B	6	0.7681	105	D	6	0.7681	285
B	7	0.8365	90	D	7	0.8365	270
B	8	0.9043	105	D	8	0.9043	285
B	9	0.9727	90	D	9	0.9727	270
B	10	1.0595	90	D	10	1.0595	270
B	11	1.1273	105	D	11	1.1273	285
B	12	1.1957	90	D	12	1.1957	270
B	13	1.2635	105	D	13	1.2635	285
B	14	1.3319	90	D	14	1.3319	270
B	15	1.3997	105	D	15	1.3997	285
B	16	1.4681	90	D	16	1.4681	270

dimensions as the 25-55 double-cone which had been built first. It was determined that the laminar prediction was sufficiently accurate for the conditions studied. Thus effort was made to increase the thermocouple density on the aft body to determine the nature of the flow in the post-reattachment region. Thermocouples are installed along two staggered rays along the aft body. The thermocouple locations, shown in Table 2.6, are measured axially along the model surface and normalized by the fore cone face length, L=56.97 mm.

Table 2.6: Normalized locations of coaxial thermocouples on the 25-48 double-cone model. Streamwise distance, s, is the distance along measured along the model surface and is normalized by the fore cone face length, L=56.97 mm.

TC #	s/L	θ (deg)
1	1.0557	15
2	1.1115	0
3	1.1533	15
4	1.2090	0
5	1.2508	15
6	1.3065	0
7	1.3483	15
8	1.4040	0
9	1.4458	15
10	1.5016	0
11	1.5434	15
12	1.5991	0
13	1.6409	15

The signal from the thermocouples is passed out of the test section into an amplifier with a nominal amplification factor of 100. This signal is then recorded by the data acquisition system at 1 MHz. The temperature is determined from the voltage using the standard NIST tables. The heat flux is then determined using a spectral decomposition method described in detail by Sanderson [13] and Davis [47]. A summary of this method is given below.

The heat flux is measured at specific points through the thermocouple response. These thermocouples are governed by the one-dimensional heat flux equation with

the following boundary conditions:

$$\frac{\partial^2 T}{\partial x^2} = \frac{1}{\alpha}\frac{\partial T}{\partial t} \tag{2.1a}$$

$$T(x,0) = T_i, \qquad T(0,t) = T_i + \Delta T(t) \tag{2.1b}$$

$$\left.\frac{\partial T(t)}{\partial x}\right|_{x\to\infty} = 0, \qquad \left.\frac{\partial T(t)}{\partial x}\right|_{x\to 0} = \dot{q}(t) \tag{2.1c}$$

where T is the temperature, x is the spatial coordinate normal to the surface, α is the thermal diffusivity, t is time, and $\dot{q}$ is the heat flux. Note that $\alpha = k/\rho c$ where k is the thermal conductivity, ρ is the density, and c is the specific heat of the material.

A solution to this equation is given as

$$\Delta T(x,t) = \int_0^t g(x, t-\tau)\, \dot{q}\, d\tau \tag{2.2}$$

where ΔT is the change in temperature and $g(x,t)$ is an impulse function given by

$$g(x,t) = \sqrt{\frac{\alpha}{\pi k^2 t}} \exp\left(\frac{-x^2}{4\alpha t}\right), \quad t > 0 \tag{2.3}$$

where x is the junction thickness. The acquired time sequence of temperature data is assumed to be a convolution of the true temperate change over time with noise. The discrete Fourier transform is taken of the solution in order to isolate the heat flux component. The heat flux solution is then found by taking the inverse Fourier transform and is represented by,

$$\dot{q} = FFT^{-1}\left[\frac{\Phi Z}{G}\right] \tag{2.4}$$

where Φ is the filter function, Z is the Fourier transform of the noisy temperature time sequence, and G is the Fourier transform of the impulse function, g. A lowpass Butterworth filter with a cutoff of 20 kHz was used. Past work has shown that the majority of the heat flux information is carried below this frequency [13, 47]. Additionally the temperature signal must be zero-padded so that it is at least four

times its original length to avoid acausal errors [47]. TODO: DEFINE ACAUSAL ERRORS

The physical properties of the thermocouple and the junction depth have been measured in previous studies. Davis showed that it is sufficient to use the average properties of the thermocouples calculated from data from Sundqvist [48]. The average values of the properties are $\alpha = 5.49 \times 10^{-6}\,\mathrm{m^2/s}$ and $k = 20\,\mathrm{W/mK}$ at $300\,\mathrm{K}$. A junction depth of $1\,\mu\mathrm{m}$ is used for the calculations, based on measurements completed by Davis [47]. Note that this method of heat flux calculation is specific to the thermocouple designed by Sanderson and not a general solution method for standard thermocouples.

Uncertainty in the mean heat flux value is due to three main sources: uncertainty in material properties, errors in the NIST thermocouple conversion tables, and uncertainty due to fluctuations during the test. The materials properties have an uncertainty of 8% and the conversion tables have an uncertainty of 1.7% as detailed by Davis [47]. Uncertainty due the heat flux fluctuations is accounted for by calculating the 95% confidence interval for the mean heat flux for each thermocouple [46]. The three sources of uncertainty are combined and included in the results as the error bars in the mean heat flux figures.

During the data analysis process a discrepancy was discovered between the experimental heat flux and the laminar boundary layer heat flux prediction for the 25-55 double-cone model. The laminar boundary layer theory, see Section 4.1.1, predicted a heat flux that was two to three times higher than the experimentally measured values. Through a process of elimination it was determined that the an unknown material had been unknowingly substituted during the production of the outer thermocouple pieces. The raw stock material used by the machinist for producing the thermocouples was obtained and sent to the supplier to determine the unknown material. The supplier was able to determine that the unknown material was alumel by using an Innovex XRF positive material identification analyzer. Alumel is composed of 95% nickel with small amounts of silicon, aluminum, and manganese [48] and is typically used as the negative leg of a K type thermocouple. Thus, when combined with the in-

ner electrode, made from constantan, a hybrid $E^{-}K^{-}$ thermocouple had been created. Since this is not a standard thermocouple type, electromotive force (emf) versus temperatures curves are not available and a custom lookup table was built. This lookup table was created using the single leg thermoelement values found in ASTM E230 standards [49]. Additionally, the thermal properties of alumel and constantan used in the heat flux calculations, $\alpha = 6.905 \times 10^{-6}\,\mathrm{m^2/s}$ and $k = 25.95\,\mathrm{W/mK}$ at $300\,\mathrm{K}$, are obtained from Sundqvist [48].

2.4.2 Schlieren

Single frame and high-speed schlieren images have been obtained in the HET. The single frame images are obtained using a PCO.1600 camera illuminated by a Xenon 437B nanopulser. The nanopulser has a pulse width on the order of 20 ns. High-speed images in the HET are obtained using a Photron SA-5 with a custom built white-light LED light source. Typical high speed images are acquired at 100 kHz with a 1 µs exposure time. The HET setup uses $\lambda/4$, 108.0 mm, f/10 parabolic mirrors in the standard Z-type setup with one turning mirror. A diagram of the setup is shown in Figure 2.8.

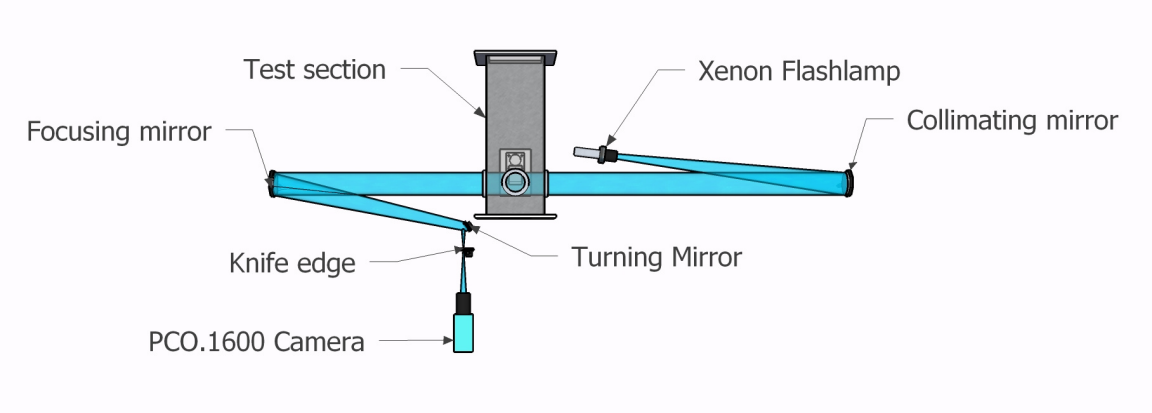

Figure 2.8: Diagram of HET schlieren setup.

High-speed shadowgraph images have been obtained in T5 using the Shimadzu HPV-X2, shown in Figure 2.9. This camera allows for framing rates up to 10 MHz at a constant 400×250 pixel resolution for up to 256 frames. Due to the frame limit

constraint, framing rates at 100 kHz, 200 kHz, and 1 MHz are used to capture different phenomena in the T5 tests. A different light source is used in the T5 experiments due to the luminescence behind the shocks making the use of a white light source for schlieren impractical. A custom built pulsed laser source developed by Parziale et al. [50] is used. A Sony SLD1332V laser diode is paired with a PicoLAS LDP-V 03-100 UF3 driver module to produce light at 670 nm, shown in Figure 2.10. The pulse length was varied between 40 ns to 85 ns depending on the level of zoom required. At higher levels of zoom, a longer pulse length is required to account for the loss of light at the camera. The light from the diode is collimated using a F810SMA-780 collimator and expanded using a -100 mm focal length plano-concave lens. The standard T5 mirror setup is used with the 203.2 mm, f/15 collimation mirrors, a schematic of which is shown in Figure 2.11. A 670 nm optical bandpass filter is used in front of the camera to prevent luminescence from overexposing the CCD while allowing the laser light to pass. Even with the bandpass filter, some flow luminescence is observed in the images, especially in the impingement region of the double-cone.

Figure 2.9: Image of the Shimadzu HPV-X2 camera used for the high-speed shadowgraph images obtained in T5.

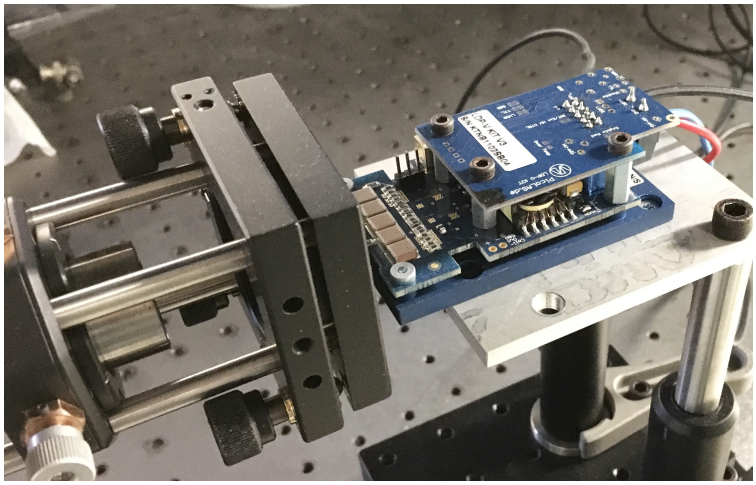

Figure 2.10: Image of Sony SLDV1332V laser diode and PicoLAS LDP-V 03-100 UF3 driver module. The diode is located within the laser diode adapter in the left-center of the image. Additionally, the F810SMA-780 collimator is seen on the left side of the image.

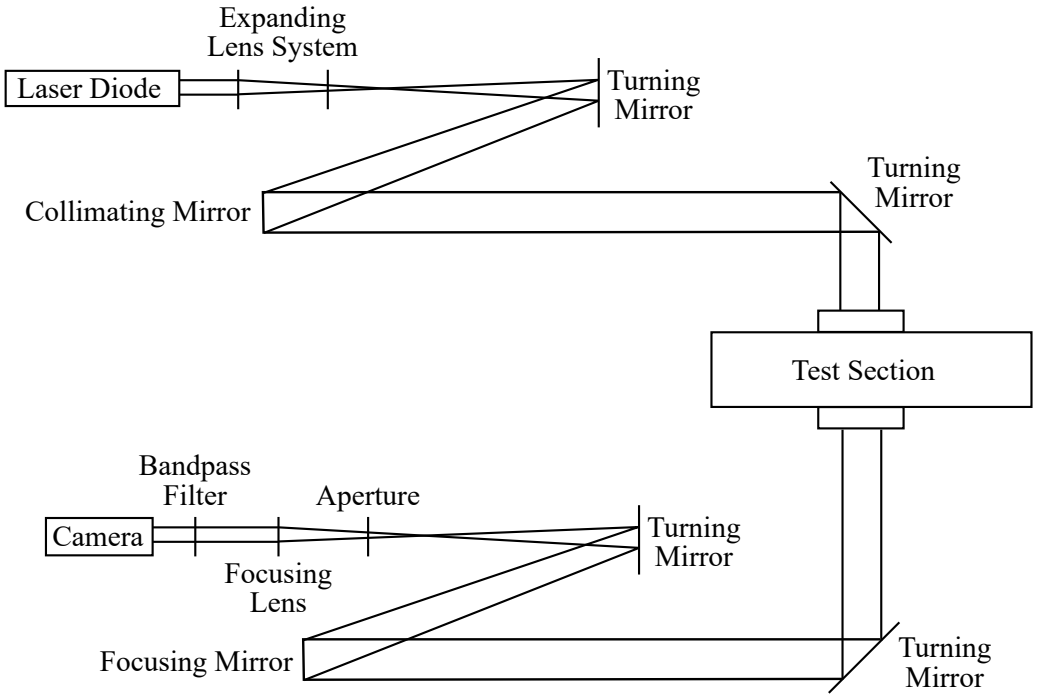

Figure 2.11: Schematic of T5 shadowgraph setup.

CHAPTER 3

HIGH-SPEED SHADOWGRAPH RESULTS

High-speed shadowgraph images are obtained for the double-wedge and double-cone in T5. These images are used to observe and measure the startup process for the flow over the model. Additionally, measurements are taken of the shock structures such as the triple point for shock-shock interaction analysis and of the separated boundary layer for the separation scaling model.

Two sets of high-speed shadowgraph images have been obtained for the low-pressure conditions for the double-wedge in T5. High-speed shdowgraph images were obtained for the all of the T5 run conditions for the double-cone. Two framing rates are required due to the camera having a finite number of frames in order to get a full understanding of the temporal evolution of the flow. The first set of images was obtained at a lower framing rate, typically 100 kHz–200 kHz. The lower framing rate is used to observe the startup process and ensure the flow structure reaches a stable configuration. The second set of images was obtained at a higher framing rate, typically 1 MHz. The higher framing rate allows for analysis of the transient structures, such as those seen in the shear layer.

3.1 Facility Startup

The flow startup process in T5 differs from the HET flow startup process due to the difference in gas acceleration method. The HET accelerates the test gas first through a moving shock and then an unsteady expansion wave. The test gas then exits the acceleration tube without a nozzle into the test section and flows over the model. In T5, the test gas is compressed and heated through a strong incident and reflected

shock and then expands through a nozzle into the test section. Discussion of the HET flow startup process for the double-cone and double-wedge may be found in Swantek [17].

High-speed shadowgraph is used to observe the flow startup process in T5. A measure of the flow establishment time is made using these images. In order to obtain a meaningful establishment time we must take into account the gas acceleration method and tunnel startup process. In T5, the gas processed by the primary shock is expanded through the nozzle into the test section. The reservoir pressure takes a finite amount of time to reach a steady stagnation pressure as recorded by the pressure transducers just upstream of the throat, see Figure 2.7. This pressure rise typically takes place over approximately 400 µs–500 µs at which point the stagnation pressure remains steady for 1 ms–2 ms. Typically, the stagnation pressure overshoots the steady stagnation pressure before relaxing to the test time pressure level. The maximum pressure overshoot ranges from 5%–8% higher than the steady test time pressure and can add up to an additional 400 µs in startup time. Since the shock tube reservoir takes a finite amount of time, up to 900 µs, to reach the steady test time pressure, it has been measured for each experiment and designated as $t_{reservoir}$. Additionally, the flow takes a finite amount of time to expand through the nozzle and an estimation of the nozzle flow through time of 250 µs is designated as t_{nozzle}. This time is based on axisymmetric calculations using the centerline velocity and previous experimental work [51]. The establishment times, $t_{establishment}$, determined from the images are found using the following:

$$t_{establishment} = t - t_{reservoir} - t_{nozzle} \tag{3.1}$$

where t is the time of experiment acquisition referenced to the primary shock reflection.

3.1.1 Double-Wedge

A sequence of images showing the evolution of the double-wedge flowfield during startup is shown in Figure 3.1 for the H8-Re2 Air condition. Due to the large number of images collected during each run, only a selection of images is included which shows the highlights of the startup process. Unless otherwise noted, the times listed in this section are referenced from the primary shock reflection from the nozzle endwall.

The first image, Figure 3.1a, shows that the formation of the oblique and bow shock has started. Approximately 60 µs later, Figure 3.1b, the bow shock and oblique shock have become stronger but have not reached their final location. At this point the bow shock is at its furthest downstream location. The separation shock is also visible at this point and the separation begins to grow. In Figure 3.1c the bow shock is seen moving upstream causing the transmitted shock to also move upstream. It reaches a max upstream location at 0.64 ms as shown in Figure 3.1d. The bow shock then retreats and reaches an established location at 750 µs and remains at this location through the duration of the steady test time.

For the double-wedge the bow shock is unaffected by the separation shock due to the small size of the separated boundary layer near the hinge. The separation reaches an established size by 0.85 ms based on movement of the separation location as seen in the images. The bow shock and separation exhibit oscillations in their location and size respectively. For shot 2851 the reservoir filling time is measured as $t_{reservoir} = 900\,\mu s$ which is longer than the longest measured startup process observed in the shadowgraph images. This has two possible implications. The first is that the response of the shock tube reservoir pressure transducer does not accurately reflect the actual nozzle reservoir pressure response due to either the response time being too slow or due to the finite filling time required for the transducer measurement volume. This is unlikely as the transducers used, PCB Model 119M44, have a rise time of less than 2 µs. The more likely explanation is that the flow evolution occurs sufficiently fast in response to the changing freestream conditions that the external flow features are never in a non-equilibrium shock configuration with respect to the

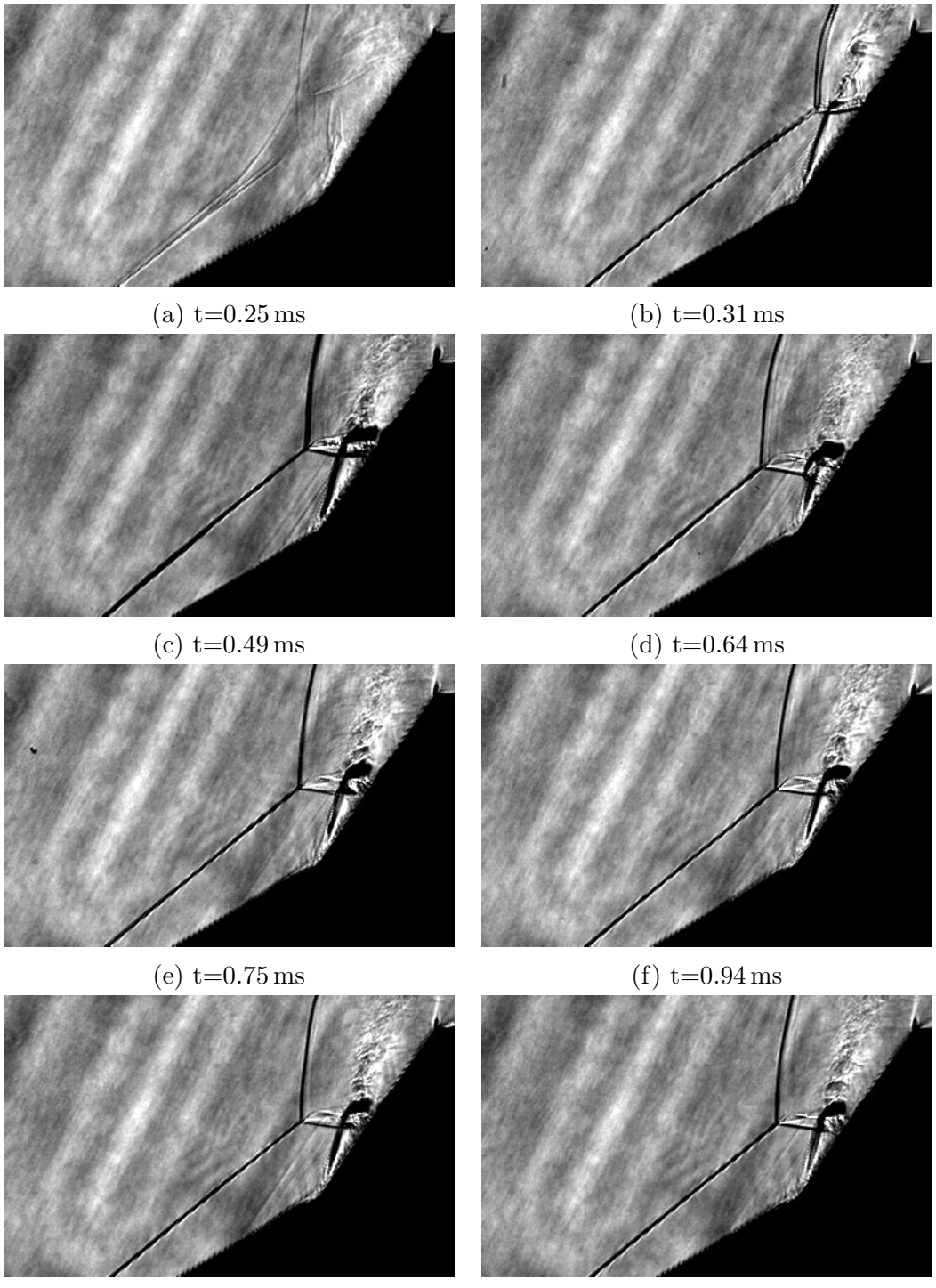

(a) t=0.25 ms (b) t=0.31 ms

(c) t=0.49 ms (d) t=0.64 ms

(e) t=0.75 ms (f) t=0.94 ms

(g) t=1.70 ms (h) t=2.13 ms

Figure 3.1: T5 double-wedge startup process, Shot 2851. All times are referenced from primary shock endwall reflection. The viewing area is 55.7 mm × 34.8 mm.

instantaneous freestream conditions.

3.1.2 Double-Cone

The startup process of the double-cone is qualitatively similar to the double-wedge. A labeled shadowgraph image of the flow over the 25-55 double-cone is shown in Figure 3.2. The nature of the established flowfield is detailed further in Section 3.2 where the wave types with the assistance of shock polar diagrams. However, there are small differences in the intermediate processes between the nitrogen, air, and carbon dioxide test gas and also between the low and high pressure condition with all five conditions presented here. A sequence of images showing the evolution of the double-cone flowfield during startup is shown in Figure 3.3 for the H8-Re2 nitrogen condition. The first image, Figure 3.3a, shows the oblique and bow shock forming and is fully formed 35 µs later. Unlike the double-wedge the separation starts away from the corner and is seen to form simultaneously with the leading oblique shock. The bow shock initially starts back on the aft cone but rapidly moves forward and reaches a steady location by 0.30 ms. The separation initially begins to shrink and reaches a minimum size at 0.395 ms as seen in Figure 3.3d. The separation then expands and reaches its final established size at approximately 0.75 ms. During the remainder of the test time the separation location oscillates over a distance of 2.2 mm. Again the reservoir fill time for this shot is longer than the establishment time with $t_{reservoir}$ =1 ms.

The flowfield startup evolution of the double-cone for the H8-Re2 air condition is shown in Figure 3.4. Similarly to the nitrogen condition, the oblique and bow shock are visible and fully formed by 255 µs. Unlike the nitrogen case, the separation initially starts near the hinge and rapidly expands outwards. During the startup process the separation zone never shrinks in size. The structure on the aft cone through startup has a different configuration than the nitrogen case. The reattachment shock is seen to be steady with no oscillations in Figure 3.4c. In the post-impingement region a wave is seen emanating from the surface and reflects off the slipline formed at the

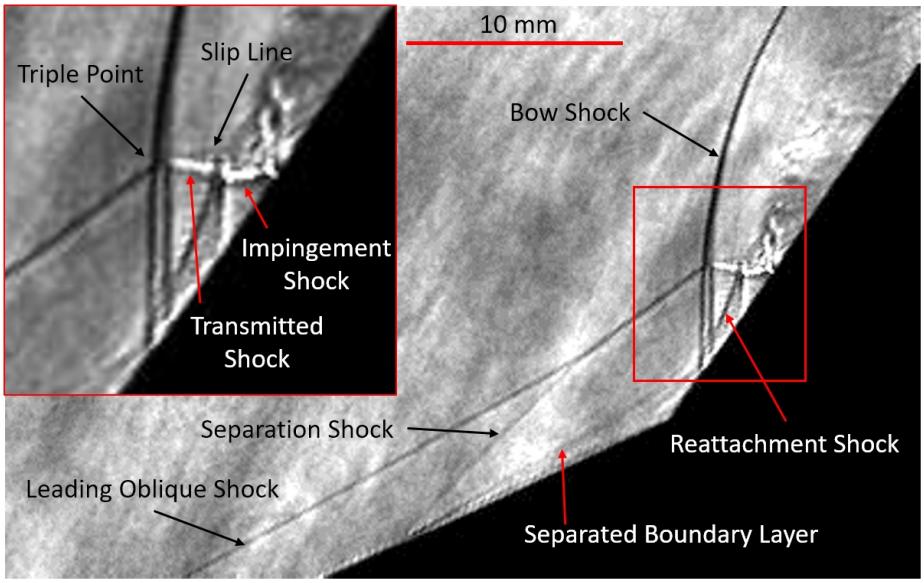

Figure 3.2: Labeled image of established flowfield for 25-55 double-cone.

primary triple point of the main oblique shock and the bow shock. Over the span of the next 20 µs the laminar nature of the structure breaks down.

The start of this breakdown is seen in Figure 3.4d where several changes to the flow field are seen to simultaneously occur. The wave which reflects off the shear layer breaks down into a series of repeating waves which convect downstream. The breakdown progresses and after approximately 25 µs no apparent structure is observed. Additionally we observe a series of waves behind the separated shock. In the videos these waves appear to emanate from the reattachment shock and oscillate between the separation shock and the reattachment shock. These oscillations in the reattachment shock persist for the remainder of the test. As time progresses the separation location moves upstream and reaches the test time location by 0.765 ms as seen in Figure 3.4f. As the separation shock moves forward the triple point formed by the intersection of the separation and bow shock moves downstream. This causes the transmitted impingement shock to move downstream as well as the size and shape of the post bow shock structure remains constant through the test. For this shot the test time reservoir pressure level was reached at 1.015 ms (accounting for the nozzle flow through time). Thus the separation has found a stable configuration before the

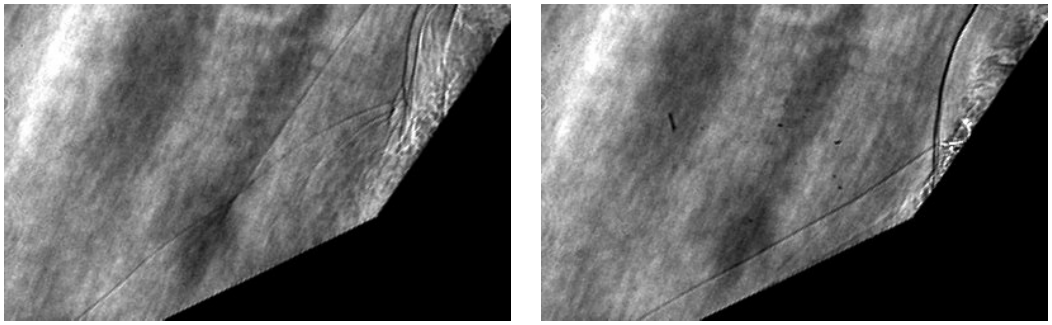

(a) t=0.24 ms

(b) t=0.275 ms

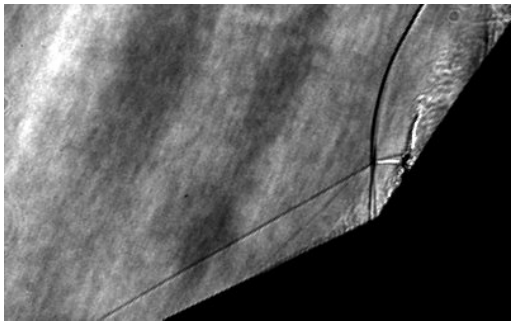

(c) t=0.325 ms

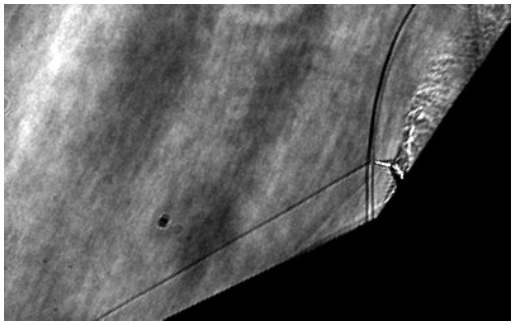

(d) t=0.395 ms

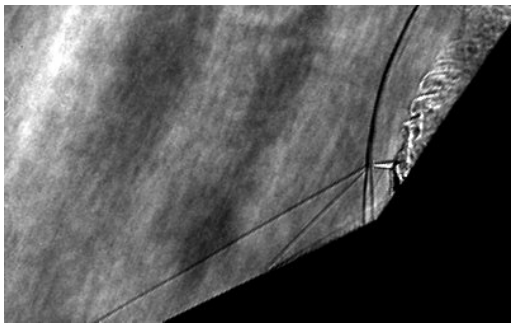

(e) t=0.46 ms

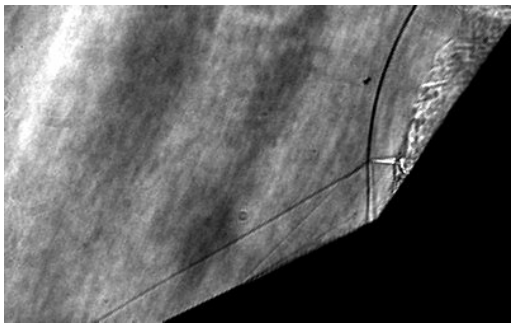

(f) t=0.63 ms

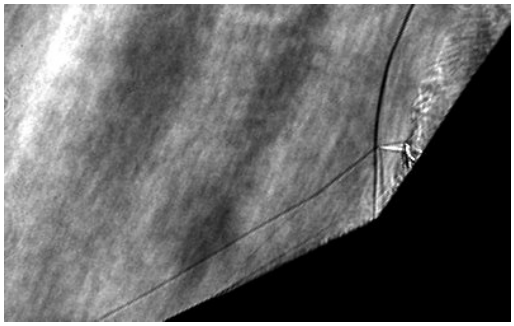

(g) t=1.085 ms

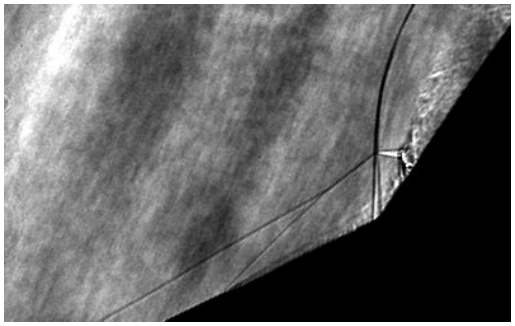

(h) t=1.415 ms

Figure 3.3: T5 25-55 H8-Re2 nitrogen double-cone startup process, Shot 2856. All times are referenced from primary shock endwall reflection. The viewing area is 42.7 mm × 26.7 mm.

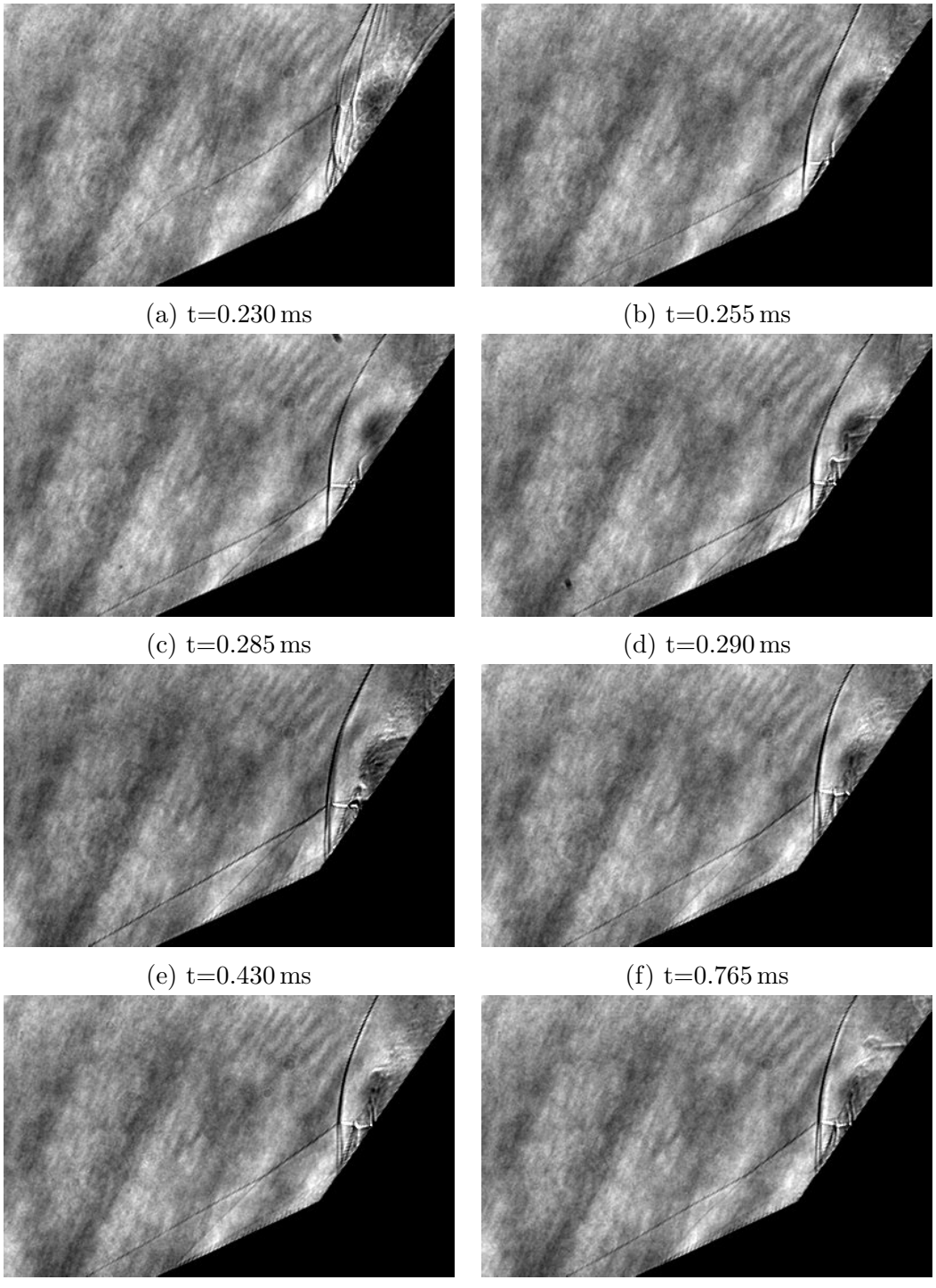

(a) t=0.230 ms (b) t=0.255 ms

(c) t=0.285 ms (d) t=0.290 ms

(e) t=0.430 ms (f) t=0.765 ms

(g) t=1.155 ms (h) t=1.440 ms

Figure 3.4: T5 25-55 double-cone H8-Re2 air startup process, Shot 2858. All times are referenced from primary shock endwall reflection.

reservoir pressure has stabilized.

The H8-Re2 carbon dioxide startup process is shown in Figure 3.5, shot 2875. Note that the shocks are rather difficult to see for this shot due to issues with focusing the camera from resetting up the shadowgraph system. The startup process is similar to the other two gas compositions. The primary difference is in the growth pattern of the boundary layer separation. The separation is initially small such that the separation shock does not interact with the leading oblique shock until 700 µs. At this point the separation grows outward until it reaches its maximum size at 1.05 ms while simultaneously the nozzle reservoir experiences a local minimum in stagnation pressure. The stagnation pressure then rises slightly and levels off for approximately 400 µs over which the measurements are made. As the pressure rises in the reservoir the boundary layer separation retreats slightly upstream and then remains steady. Through this process the structure of the shock-shock interaction remains constant, however the location of the triple point shifts due to the interaction of the separation shock with the leading oblique shock.

The double-cone startup process for the H8-Re6 nitrogen run condition is shown in Figure 3.6. The high and low pressure shots have the same general shock structure. At the start of the test the oblique and bow shock form at 260 µs with the oblique shock reaching its established location at 320 µs. The separation is initially not visible for this condition. It first appears 410 µs after the test start and is initially located close to the corner. It grows to its established size over a span of 350 µs where it remains for the remainder of the test. The separation shock for this condition does not intersect the leading oblique shock due to the smaller separation size. It also does not appear to strongly influence the triple point transmitted shock. There are no changes in the overall flow structure once the separation location stabilizes.

The double-cone startup process for the H8-Re6 air run condition is shown in Figure 3.7. The startup begins similarly to the H8-Re6 nitrogen condition in the time it takes for the oblique and bow shock to form and stabilize in position. The major difference from the nitrogen case is that the separation is observable from the beginning of the test and is located away from the hinge. Over the next 980 µs the

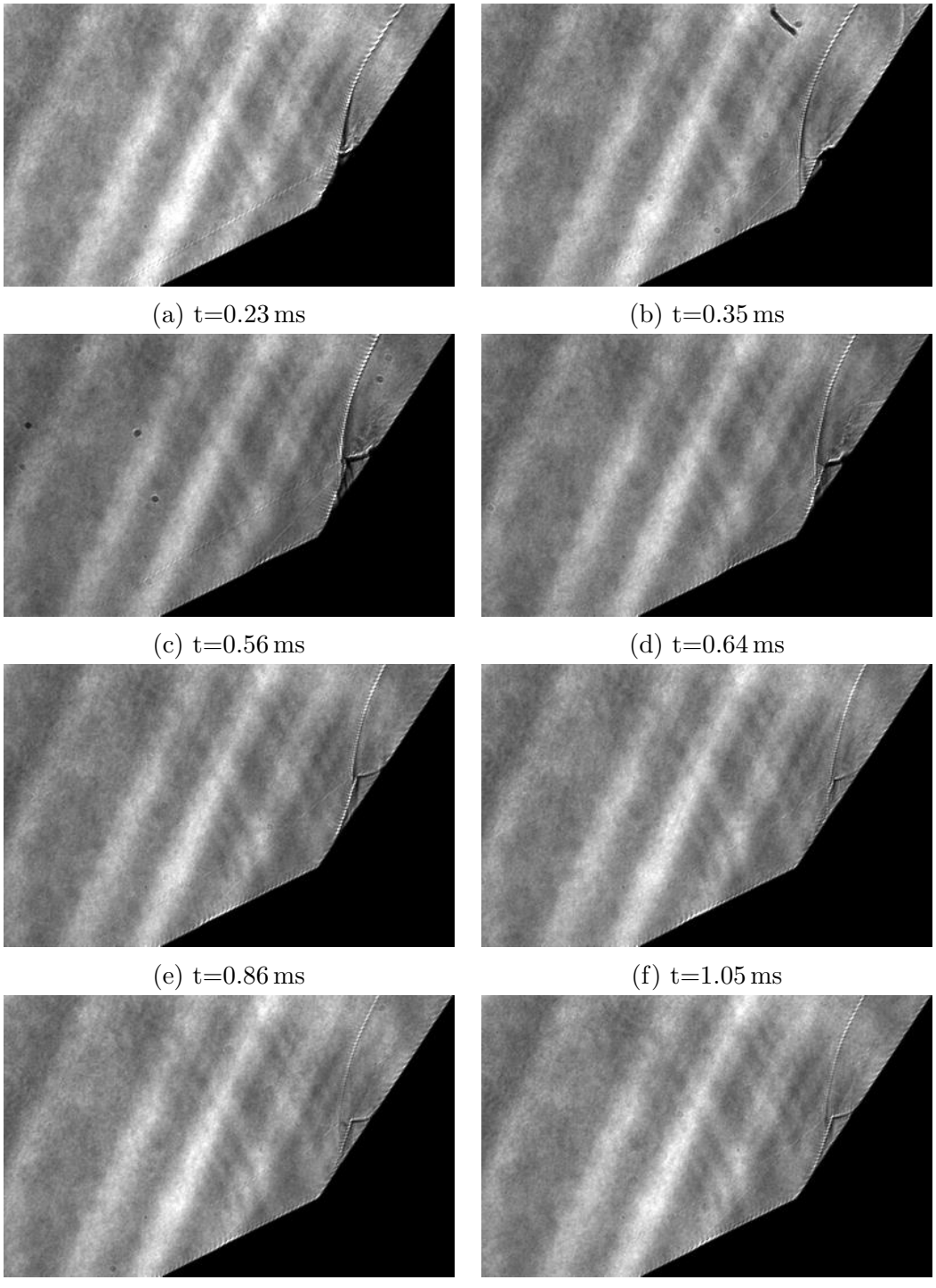

(a) t=0.23 ms (b) t=0.35 ms

(c) t=0.56 ms (d) t=0.64 ms

(e) t=0.86 ms (f) t=1.05 ms

(g) t=1.20 ms (h) t=1.41 ms

Figure 3.5: T5 25-55 double-cone H8-Re2 CO2 startup process, Shot 2875. All times are referenced from primary shock endwall reflection.

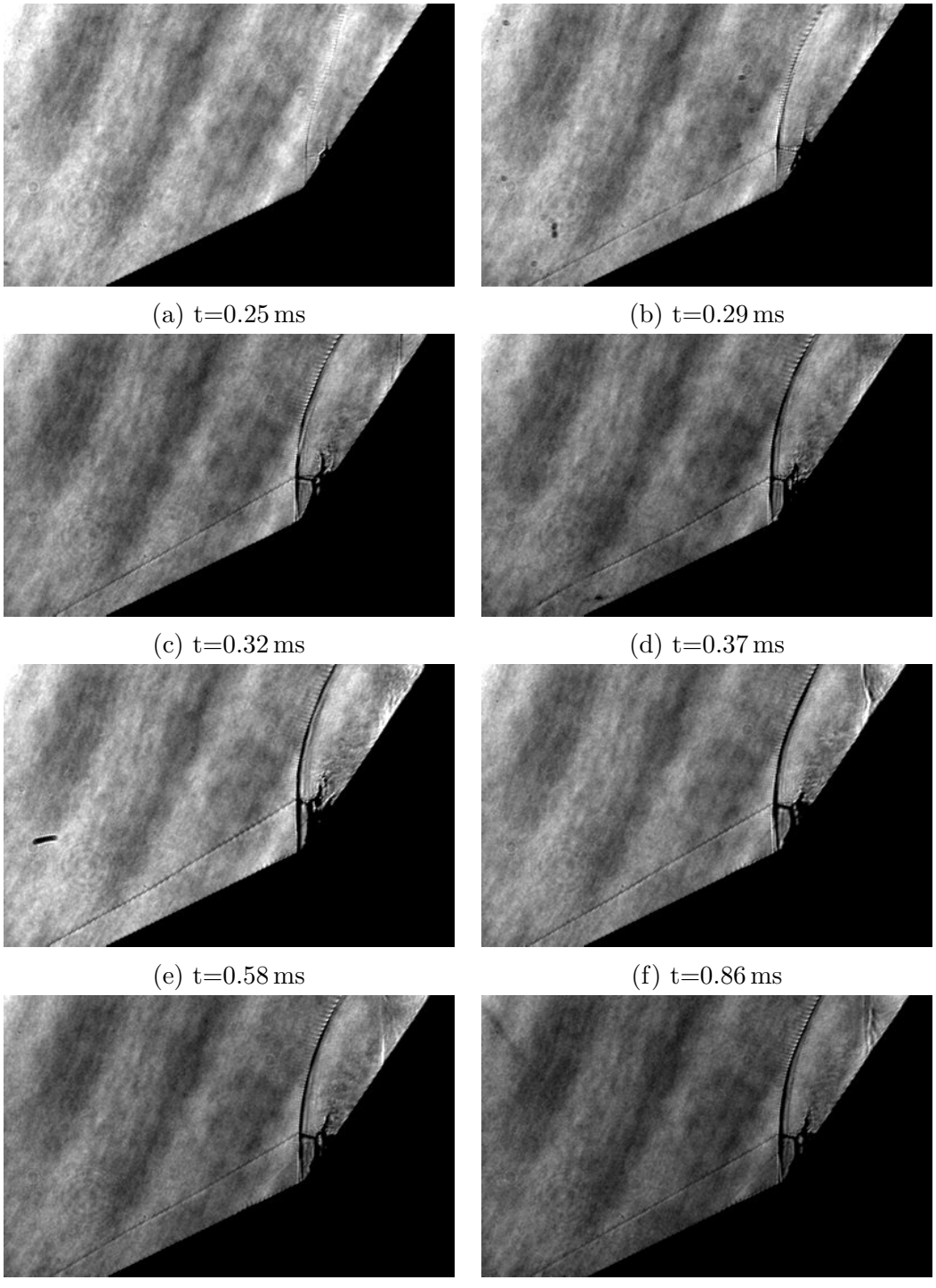

(a) t=0.25 ms (b) t=0.29 ms

(c) t=0.32 ms (d) t=0.37 ms

(e) t=0.58 ms (f) t=0.86 ms

(g) t=1.19 ms (h) t=1.45 ms

Figure 3.6: T5 25-55 double-cone H8-Re6 nitrogen startup process, Shot 2862. All times are referenced from primary shock endwall reflection.

separation oscillates a distance of 5.8 mm to 8.8 mm away from the hinge. Through the remainder of the test the separation oscillates over a distance of less than 1 mm. Like the nitrogen case, once the separation reaches its test time location, no other changes in the shock interactions are observed.

The startup process for the 25-48 double-cone is examined next. A labeled shadowgraph image of the important flow features for the 25-48 double-cone is shown in Figure 3.8. The shadowgraph images showing the flow startup are found in Figure 3.9. All of the test conditions studied with the 25-48 double-cone admit very similar startup processes to one another so only the H8-Re2 air test condition will be examined here. Supersonic flow establishes over the model by 260 µs with the completed formation of the fore and aft oblique shocks. The boundary layer separation is also apparent at this time. Over the next 150 µs the forebody oblique shock steepens and the separation location moves upstream. From this point on there are only small oscillations in the separation location and no movement of the forebody oblique shock. The remaining changes that the flow undergoes are in regards to the shock interaction region. From 500 µs to 750 µs the shock interaction weakens slightly by the curvature of the bow shock at the triple point becoming less noticeable until a purely oblique shock is seen over the aft part of the model. Again, all of these changes in the flow structure finish at the same time as the pressure reaches its steady value.

There is one unique phenomenon for the carbon dioxide experiments during the startup. The oblique shock slowly grows until approximately 500 µs when it abruptly jumps to a larger angle where it remains for the remainder of the test. A similar jump in oblique shock angle has been seen in previous HET experiments when the contact surface between the expanded test gas and shocked expansion gas passes by the model. In the T5 CO2 experiments this jump is most likely due to the contact surface between the air initially located in the nozzle and dump tank while the carbon dioxide is initially located within the shock tube.

The startup shadowgraph images show that the definition of the startup time must be precisely defined due to the interconnected nature of the flow structures. The primary flow inviscid flow structures, the leading oblique shock, triple point and bow

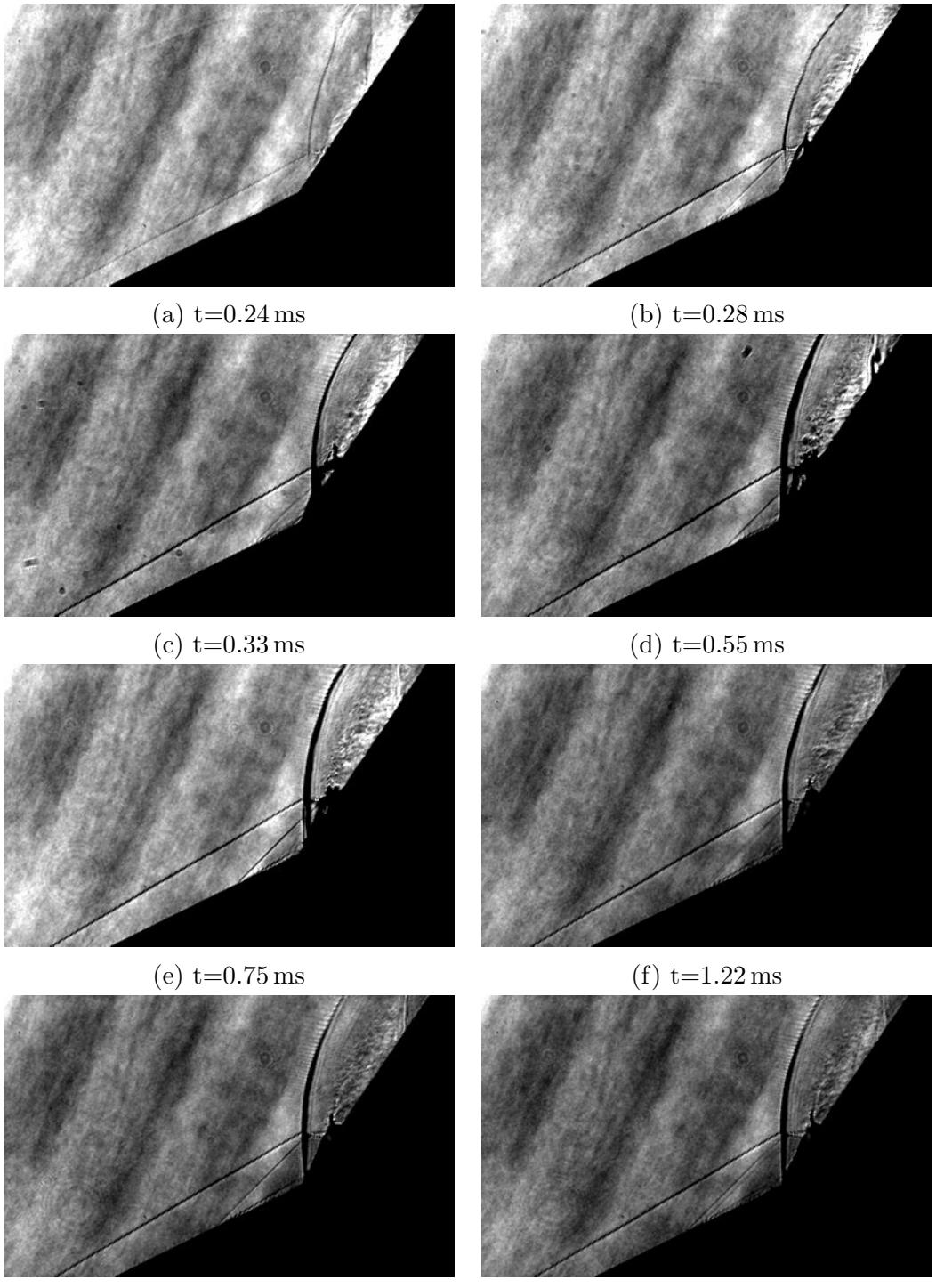

(a) t=0.24 ms (b) t=0.28 ms

(c) t=0.33 ms (d) t=0.55 ms

(e) t=0.75 ms (f) t=1.22 ms

(g) t=1.36 ms (h) t=1.53 ms

Figure 3.7: T5 25-55 double-cone H8-Re6 air startup process, Shot 2861. All times are referenced from primary shock endwall reflection.

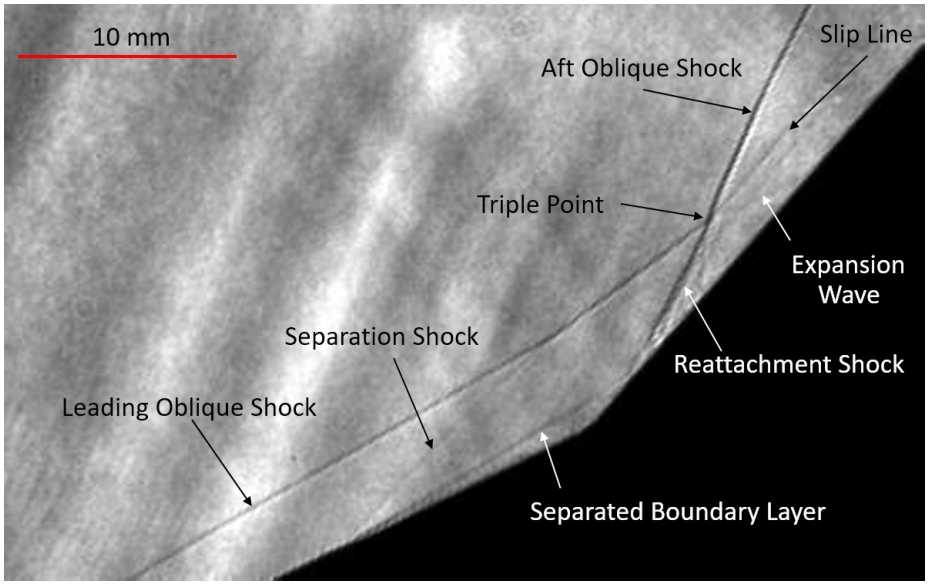

Figure 3.8: Labeled image of established flowfield for 25-48 double-cone.

shock, may be used in some cases. However, the triple point location is observed to be influenced by the separation shock when the separation becomes sufficiently large. With the 25-55 double-cone the separation shock of the high Reynolds number cases does not interact with the bow shock. This leads to a shorter establishment time for the triple point. At lower Reynolds number the separation is seen to impact the triple point interaction location and is then directly linked to the boundary layer separation location. Additionally, the physical starting process of the tunnel must be considered. In conclusion, the T5 stagnation pressure rises to its test time value gradually enough such that the flow over the model is able to adjust in sync with the pressure change.

3.2 Shock Interactions

The shock interaction type has been observed to drastically affect surface heat flux and surface pressure [14]. The interaction type is observed to vary based on test condition and both deflection angles.

Previous work on shock interactions by Olejniczak et al. [14] examined shock interactions over a double-wedge using inviscid simulations. They observed four of the

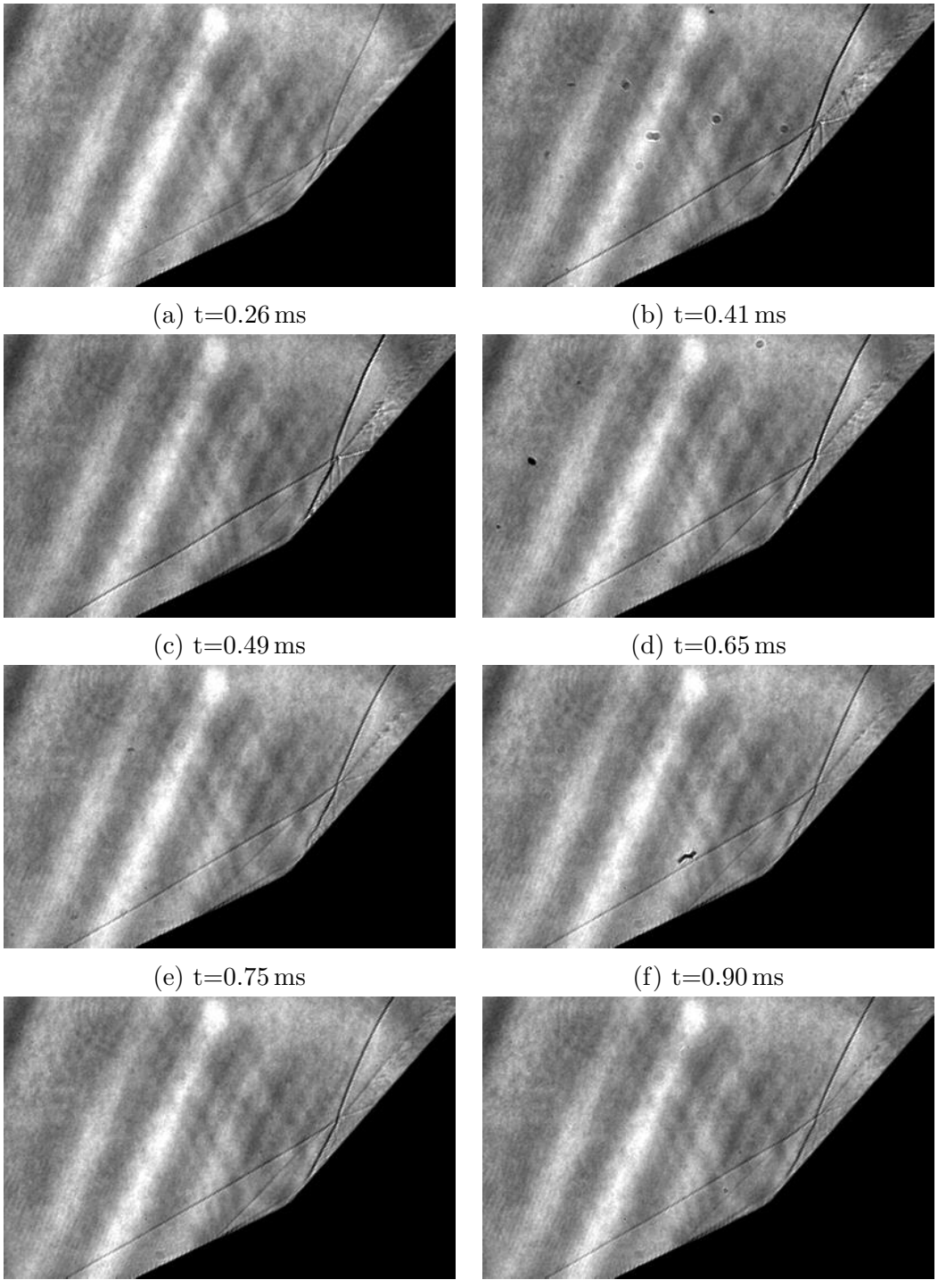

(a) t=0.26 ms (b) t=0.41 ms

(c) t=0.49 ms (d) t=0.65 ms

(e) t=0.75 ms (f) t=0.90 ms

(g) t=1.05 ms (h) t=1.30 ms

Figure 3.9: T5 25-48 double-cone H8-Re2 Air startup process, Shot 2878. All times are referenced from primary shock endwall reflection.

six interaction types. However only three of the interactions, types IV, V, and VI, were observed in the high Mach number simulations (M>3.5). Additional sub-types were defined for the type VI and type IV interactions. Type VI interaction sub-types are classified based on the state of the post-bow shock gas. The strong type VI is defined as when the oblique shock becomes strong enough such that a small pocket of subsonic flow exists near the triple point. If the deflection angle is increased further, the oblique shock becomes curved near the triple point and the subsonic region grows forming the supercritical type VI interaction. A secondary type IV interaction occurs at high flap deflection angles such that the transmitted shock impinges directly on the surface of the front wedge.

The interaction transitions are primarily a function of the incoming Mach number, first and second body deflection angles, gas composition, and ratio of surface lengths. Experimental and numerical studies have examined the transition locations as a function of these parameters [14, 52]. Experimental double-wedge studies have shown the type VI to V transition occurring close to the maximum deflection angle for the freestream conditions [52]. The model in this previous study was made from two pieces with a small gap at the hinge location to prevent boundary layer separation. Schlieren images were used to determine the interaction type as the aft wedge was swept for a range of deflection angles. However, the inviscid numerical studies showed the VI-V and V-IV transition occurring at a much lower flap angle that what was reported in the experiments [14]. The design of the experimental model and viscous effects were cited as probable causes for the discrepancy. The VI-V transition was determined through the method of characteristics by determining when the deflection of region 4 reaches the maximum deflection angle for the freestream conditions. However, there exists a small range of flap deflection angles over which the deflection occurs such that the two sub-type VI interactions exist within this region. The V-IV transition was determined through repeated simulations and can not be found analytically. This transition occurs at a slightly larger flap deflection angle than the freestream maximum deflection angle. Wright et al. [15] made observations of the shock interaction type for double-cones at low enthalpies.

In the current work two different interaction types are observed in the experimental results. In order to classify the interactions into different types, observations from the schlieren images are used in conjunction with pressure deflection (pθ) shock polar diagrams. In the current work the type VI interaction is observed with the 25-48 double-cone and type V interaction is observed with the 25-55 double-cone. The differences between the two flowfields will be discussed here through the use of shock polar diagrams.

The shock polar diagrams show the locus of all possible solutions for a given incoming flow which encounters a shock or expansion. Here the pressure change is plotted for a given deflection angle. For this document, upward (counter-clockwise) deflections are indicated as positive deflections while downward (clockwise) deflections are indicated as negative. The plots are created by sweeping through all possible wave angles which are bounded by a Mach wave and normal shock. The markers are placed by calculating the post-shock conditions using the measured wave angles of the triple point incoming oblique shock, the reattachment shock, and the bow shock. An additional marker is placed on the plot indicating the deflection of the slip line as measured from the shadowgraph image. The wave angles are measured using ImageJ [53].

It is important to note that only approximate results can be obtained using these pressure-deflection diagrams for the double-cone geometry. Pressure relaxation effects affect both the pressure and local flow deflection angle behind a shock in the axisymmetric flow field. Thus the results are only valid in a small region near the interaction. The double-wedge is not immune to problems as care must also be taken due to changing post-shock conditions of the curved bow shocks.

As mentioned previously the type VI interaction occurs with the 25-48 double-cone geometry. Edney [12] found that this interaction occurs when an oblique shock interacts with a bow shock above the sonic location. This interaction results in an expansion wave and shear layer. No distinct rise in heat flux is observed as the shear layer does not impinge on the model surface. A schematic of the diagram in the context of the double-cone is shown in Figure 3.10. Two variants of the type VI interaction are observed for the double-cone in the T5 experiments based on the location of the

separation shock (not shown in the schematic). In the more common version, seen in Figure 3.11, the separation shock interacts with the leading oblique shock resulting in a stronger transmitted shock and weak slip line. This interaction is observed for the low Reynolds number condition tests with the 25-48 double-cone. The second, less common version has the separation shock intersecting the reattachment shock and is only observed in the high Reynolds number experiments.

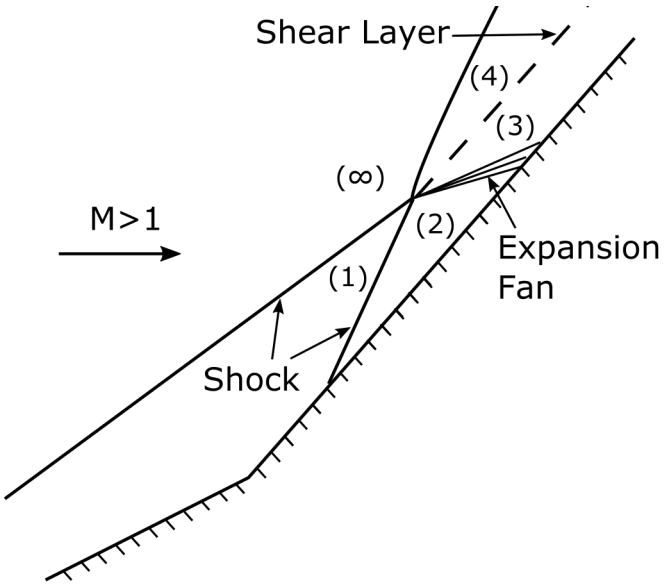

Figure 3.10: Schematic of type VI interaction with labeled regions for shock polar diagrams.

The shock polar diagrams for the H8-Re2 air and H8-Re2 carbon dioxide conditions are shown in Figures 3.11 and 3.12. Both conditions result in the standard type VI interaction and the resulting pressure deflection plot is very similar between the two. The first oblique shock causes a deflection to approximately 25° and the gas travels along the shock polar to state 1. The gas is then shocked and deflected upward as it travels through the reattachment shock to state 2. The gas must then expand to reach a matching deflection angle with the measured shear layer deflection angle reaching state 3. The gas in state 3 must match the post bow shock conditions that determine state 4. Here the local angle near the triple point of the aft obliqe shock is measured. Frozen and equilibrium oblique shock calculations using the measured wave angle are made to bracket the possible post shock states. The frozen and equilibrium polars

for freestream conditions are shown in solid and dashed gray lines respectively.

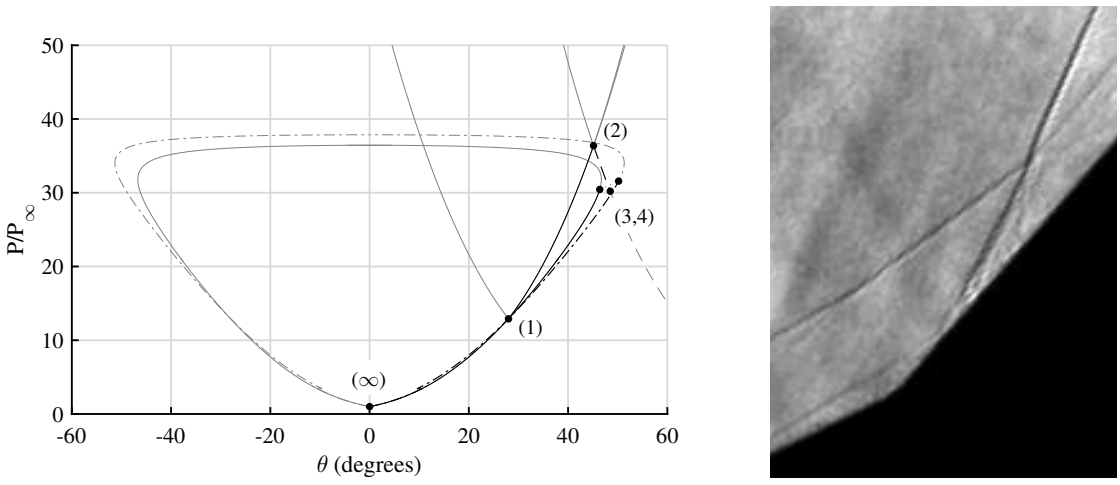

(a) (b)

Figure 3.11: Shot 2879, H8-Re2 Air 25-48 double-cone

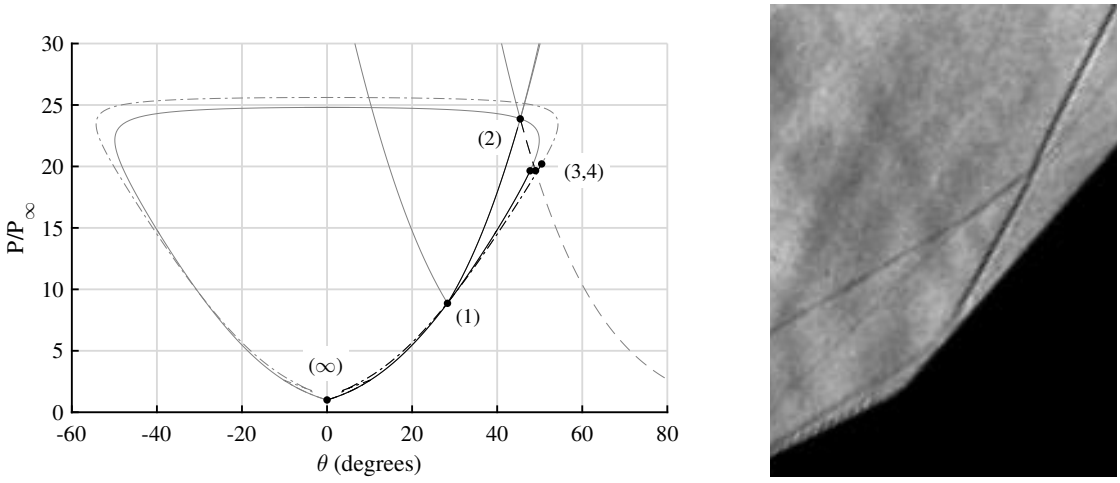

(a) (b)

Figure 3.12: Shot 2881, H8-Re2 CO2 25-48 double-cone

The shock polar diagram for the H8-Re2 nitrogen condition is shown in Figure 3.13. This interaction is an example of the strong Type VI interaction as the matching condition is located above the sonic point on the shock polar. This is a result of the curvature of the aft shock wave near the triple point.

The shock polar diagram for the H8-Re6 air condition is shown in Figure 3.14. In this configuration the separation shock intersects the reattachment shock below the

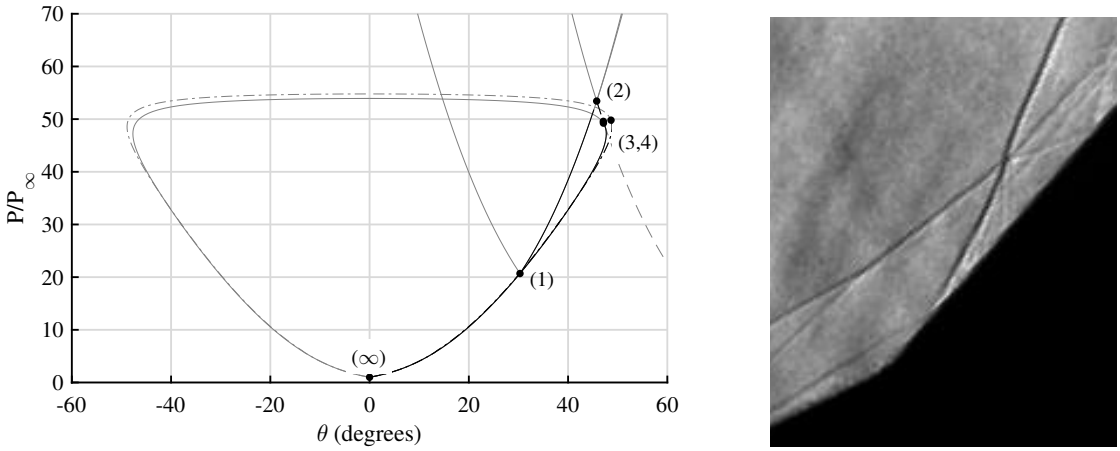

(a) (b)

Figure 3.13: Shot 2877, H8-Re2 N2 25-48 double-cone

primary triple point, as seen in Figure 3.14b. While there must be an increase in the reattachment shock strength due to the separation shock intersection, no change in the shock angle is observed in the images. Notably, the matching condition points between states 3 and 4 show the post aft shock conditions being close to equilibrium compared to the other shock-polar diagrams. The conclusion that the high Reynolds number air condition is in equilibrium in the post-shock region could be made. Intuitively this makes sense as this condition is the most likely to be in equilibrium due to the increased density allowing for increased reaction rates. However, this is a dubious argument due to the sensitivity of the polars to the measured wave angles. Small changes in the measured wave angles can lead to significant differences in the shock polar diagram. Thus we must reiterate that the diagrams are only intended to show trends of the shock interactions in these nonequilibrium flow fields.

The shock interactions of the 25-55 double-cone model are observed to be type V interactions. The change in interaction type is due to the larger pressure rise across the reattachment from states 1 to 2. As documented by Olejniczak [14] as the flap angle is increased the pressure rise across the reattachment shock becomes larger than what a single shock can provide. The type V interaction is defined by the appearance of the seven shock structure. A schematic of the interaction is

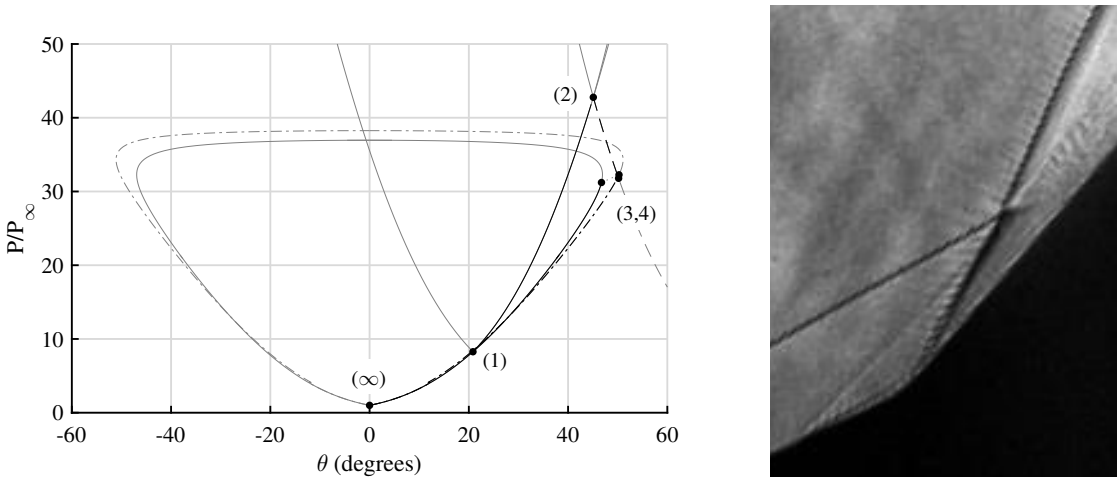

(a) (b)

Figure 3.14: Shot 2882, H8-Re6 Air 25-48 double-cone

shown in Figure 3.15c. Significantly this leads to shock impingement on the model surface behind the reattachment shock. In section 4.3 we show that this shock has a significant local effect on the surface heat flux.

A showdowgraph image of a type V interaction is shown in Figure 3.15b. The image is cropped and magnified to showcase the complex shock interaction region. The main triple point formed by the bow shock and leading oblique shock forms a transmitted shock and shear layer separating states 1 from 2 and states 2 to 3 respectively. In the shadowgraph image, a shear layer is just barely visible above the transmitted shock. Note, the black lines extending downward from the triple point are not additional transmitted shocks but actually are out-of-plane projections which are discussed at the end of Section 5.2.2. The resolution of the image is not good enough to determine the exact nature of the interaction between the reattachment shock and transmitted shock.

An attempt is made to illustrate the nature of the flowfield on a qualitative basis. The shock polar for the interaction is shown in Figure 3.15a. The primary triple point is simpler than the type VI interaction. The flow is first deflected upwards across the first shock to state 1 and is calculated from the measured oblique shock angle. The second shock deflects the gas back toward the body to match the shear layer

deflection angle at state 2 which calculated using the measured shock angle between states 1 and 2. The nearly normal bow shock imparts only a slight upwards deflection to the flow. The state 3 calculation is based on the measured normal shock angle and good matching is found between states 2 and 3.

Several major assumptions are made in order to progress any further with creating the pressure-deflection diagram that are not realistic to a real axisymmetric flowfield. Namely, we assume constant flow properties within region 1 so that we can perform an oblique shock calculation to determine state 6. While this assumption is not true for conical flows, it allows for a qualitative assessment of the flow to be made. Using this assumption we can determine the approximate flow deflection and pressure rise from the measured reattachment shock angle determining state 6. By examining the schematic and shadowgraph image we see that the flow comes together to roughly the same flow deflection. In terms of the shock polar this means that we must have approximate matching across a normal shock from state 1, up the right leg of the shock polar for state 2 and up the left leg of the shock polar for state 6. At this point the flow becomes extremely complex, even in the planar case, and can no longer be described by polar diagrams.

Despite the assumptions made in regards to the flow conditions of region 1, the shock polars are in reasonable agreement with the nonequilibrium inviscid triple cone simulation of the shot considered. The specifics of the triple cone simulations are given in Section 5.2.2. Table 3.1 shows the normalized pressure and flow deflection angles calculated using the shock polar diagram and extracted from the inviscid triple cone simulations for shot 2860. Good agreement is seen with the pressure calculations and reasonable agreement is seen between the flow deflection angles. This is not to say that this can be applied across all shots and conditions as the assumptions of constant properties in the post shock regions may not hold far from the shock. Any increase in size of regions post-shock regions may increase the errors associated with assuming constant properties as this is a conical flowfield.

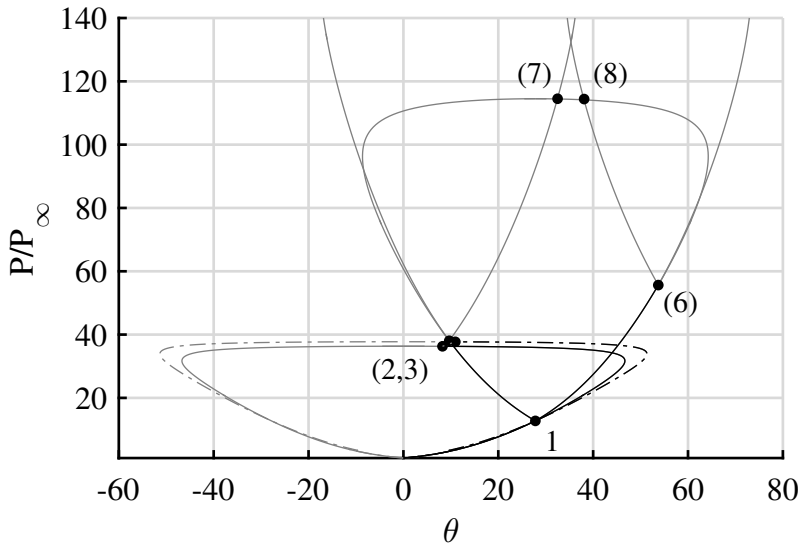

(a) Shock polar diagram

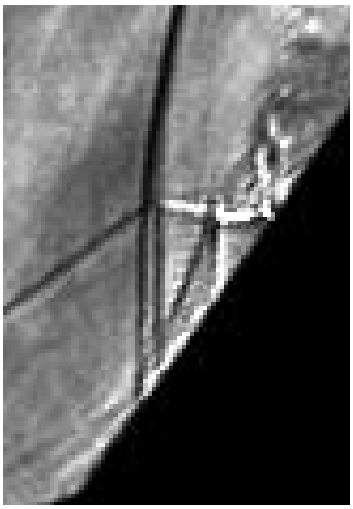

(b) Shadowgraph image of Type V interaction

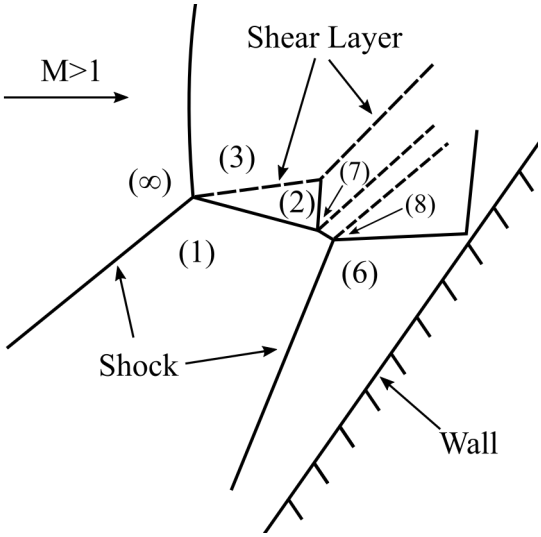

(c) Schematic of Type V interaction

Figure 3.15: Shock-polar for shot 2860, H8-Re2 Air 25-55 double-cone

Table 3.1: Comparison of property values for regions 7 and 8 for the Type V shock interaction for Shot 2860. The values are extracted from the inviscid triple cone simulations and calculated with shock polars from experimental measurements.

State	Method	P/P_∞	θ (deg)
7	Experimental Shock Polar	114	32.5
	Triple Cone Simulation	117	29.8
8	Experimental Shock Polar	114	38.1
	Triple Cone Simulation	113	35.1

3.3 Bow Shock Standoff

The location of the shock interaction triple point is partially controlled by the location of the bow shock in the 25-55 double-cone. Previous work [34] has shown a large standoff distance for a nitrogen test gas compared to an air test gas. The standoff distance is measured in reference to the base of the aft cone for the 25-55 double cone model The standoff distances are shown in Table 3.2. The increase in standoff distance for the nitrogen gas can be explained by considering the mean density ratio across the bow shock.

Table 3.2: Bow shock standoff distance and post-shock mean density ratio. Distance is measured along the model centerline and is referenced to the base of the aft cone.

Shot	Test Gas	Standoff Distance, Δ (mm)	δ (mm)	$\rho_\infty/\bar{\rho}$
2853	N2	26.2	2.84	0.145
2854	N2	26.4	2.44	0.145
2855	N2	26.3	2.61	0.145
2856	N2	26.1	2.39	0.146
2857	Air	24.0	1.90	0.131
2858	Air	23.9	1.89	0.130
2859	Air	24.0	1.96	0.130
2860	Air	23.9	2.10	0.129

Studies have shown the shock standoff distance to be a function of the mean density ratio for a variety of body shapes including spheres [54] and cones [55, 56]. The

funcitonal relationship is,

$$\Delta \propto \frac{\rho_\infty}{\bar{\rho}} \tag{3.2}$$

where Δ is the standoff distance, ρ_∞ the freestream density, and $\bar{\rho}$ the post-shock mean density. The post-shock mean density is found by performing one-dimensional nonequilibrium normal shock calculations using Cantera [38] and the SDToolbox [39]. The reaction rate data is obtained from Gupta et al. [57]. The mean density is determined by averaging over a distance, δ, that is set to be the axial distance between the normal shock and the shear layer. In the current study, the standoff distance is also found to increase with increasing density ratio.

As will be discussed later in Section 4.3, the location of the shock impingement on the surface determines the peak heating location. The shock impingement location is influenced by the triple point location which is partially determined from the bow shock standoff distance. As the bow shock moves further out from the body, the triple point shifts closer to the model apex. Thus, by understanding how the bow shock responds to changes in freestream conditions an estimation of the impact on the peak heating location can be made.

CHAPTER 4

MEAN HEAT FLUX RESULTS

Surface heat flux is measured through the use of the fast-response coaxial thermocouples. The surface heat flux profile can be broken down into four general sections: the laminar boundary layer, separated flow region, reattachment-impingement region, and post-reattachment region. Each section has a distinct heat flux response that will be explained in the following sections. The laminar boundary layer is the only portion of the flow that is easily described by theory and computations. Thus simulations and theoretical predictions are performed for the laminar boundary layer to compare with the experimental results. Including these results serves two purposes: to ensure the thermocouples are working as expected and to confirm the freestream parameters are calculated correctly.

The first section of this chapter explains the methods used to calculate the laminar boundary layer heat flux. Next the double-wedge heat flux results from the HET and T5 are discussed. Lastly, the T5 double-cone heat flux results are analyzed.

4.1 Theoretical and Computational Heat Flux

4.1.1 Laminar Heat Flux Correlation

Laminar boundary layer heat-flux predictions are made for all cases using the methods outlined in Anderson [58]. For an incompressible laminar boundary layer the skin friction coefficient, c_f is given as:

$$c_f = \frac{0.664}{\sqrt{Re_x}} = \frac{\tau_w}{\frac{1}{2}\rho u_e^2} \tag{4.1}$$

where Re_x is local Reynolds number based on the boundary-layer edge properties. A similar relation for the skin friction in compressible boundary layers is found through the use of a reference temperature, T^*, in place of the boundary-layer edge temperature, T_e. Using this method we get the following skin friction coefficient equation,

$$c_f^* = \frac{0.664}{\sqrt{Re_x^*}} = \frac{\tau_w}{\frac{1}{2}\rho^* u_e^2} \tag{4.2}$$

where

$$Re_x^* = \frac{\rho^* u_e x}{\mu^*}. \tag{4.3}$$

As shown in Meador and Smart [59], equation 4.2 can be rearranged for τ_w,

$$\tau_w = \frac{0.664}{\sqrt{Re_x^*}} \frac{1}{2} \rho^* u_e^2 \tag{4.4}$$

and substituted into equation 4.1 giving

$$c_f = \frac{0.664}{\sqrt{Re_x}} \sqrt{C^*} \tag{4.5}$$

where C^* is the Chapman-Rubesin parameter,

$$C^* = \frac{\rho^* \mu^*}{\rho \mu}. \tag{4.6}$$

The Stanton number, St, can be related to the skin friction through the Reynolds analogy, assuming a self-similar boundary-layer, as shown here:

$$\frac{St}{c_f} = \frac{Pr^{-2/3}}{2} \tag{4.7}$$

where Pr is the Prandtl number. Substituting in equation 4.5 and rearranging, the following relation is obtained,

$$St = \frac{0.332}{\sqrt{Re_x}} \sqrt{C^*} Pr^{-2/3} \tag{4.8}$$

Additionally, the heat flux, q_w can be calculated using the Stanton number through the following relation,

$$St = \frac{q_w}{\rho_e u_e (h_{aw} - h_w)} \tag{4.9}$$

where ρ_e and u_e are the density and velocity at the boundary-layer edge, h_{aw} is the adiabatic-wall enthalpy, and h_w is the wall enthalpy. Combining equations 4.8 and 4.9 a relation for q_w is found:

$$q_w = \frac{0.332}{\sqrt{Re_x}} \sqrt{C^*} Pr^{-2/3} \rho_e u_e (h_{aw} - h_w). \tag{4.10}$$

As mentioned previously the incompressible boundary-layer relations can be corrected to account for compressibility effects by using a reference temperature, T^*. The choice of reference temperature has been studied by many researchers [59–64]. Young and Janssen [63] found that for Mach numbers greater than 5 and with an isothermal wall the reference temperature equation should be as follows,

$$\frac{T^*}{T_e} = 1.28 + 0.023 M_e^2 + 0.58 \left(\frac{T_w}{T_e} - 1 \right) \tag{4.11}$$

which is then used for determining C^*.

The last variable that needs to be determined is the adiabatic-wall enthalpy, h_{aw}. From Anderson [58], h_{aw} is defined as,

$$h_{aw} = h_e + r \frac{u_e^2}{2} \tag{4.12}$$

where h_e is the boundary-layer edge enthalpy and r is the recovery factor. For a laminar boundary layer $r = \sqrt{Pr}$. Additionally, we know that,

$$h_0 = h_e + \frac{u_e^2}{2} \tag{4.13}$$

where h_0 is the stagnation enthalpy. Rearranging equation 4.13 for h_e and substituting into equation 4.12 we get a relation for h_{aw} in terms of the stagnation enthalpy and

edge velocity,

$$h_{aw} = h_0 - (1 - r)\frac{u_e^2}{2} \tag{4.14}$$

which can be substituted into equation 4.10 to get wall heat flux. For the wedge the edge conditions are found easily after performing oblique shock calculations. The cone boundary-layer edge conditions are found using a script developed that uses the Taylor-Maccoll method as outlined in Anderson [65]. Equation 4.8 must be modified due to the Mangler transformation in that an additional factor of $\sqrt{3}$ must be included such that the Stanton number equation for the cone is as follows,

$$St = \frac{0.332\sqrt{3}}{\sqrt{Re_x}}\sqrt{C^*}Pr^{-2/3}. \tag{4.15}$$

This equation is used in place of equation 4.8 with the rest of the analysis remaining the same.

4.1.2 Turbulent Heat Flux Correlation

Compressible turbulent boundary layer heat flux correlations are made for the aft cone conditions to assist in determining the nature of the post-reattachment boundary layer. The development of this correlation is outlined by White [66] with the key points outlined below.

Assuming the Reynolds analogy holds true for turbulent flows we start with the skin friction correlation for incompressible flow,

$$c_{f,incomp} = \frac{0.455}{\ln^2(0.06Re_x)} \tag{4.16}$$

White and Christoph [67] used the boundary layer inner variables to extend the skin friction analysis to compressible flows. Through their analysis a stretching transformation is made such that the compressible correlation is related to the incompressible as follows,

$$c_{f,comp} = \frac{1}{F_c}c_{f,incomp}(Re_x F_{Re_x}) \tag{4.17}$$

where

$$F_c = \frac{T_{aw}/T_e - 1}{\left(\sin^{-1} A + \sin^{-1} B\right)^2} \tag{4.18}$$

and

$$F_{Re_x} = \frac{1}{\sqrt{F_c}}(\mu_e/\mu_w)(T_e/T_w)^{1/2} \tag{4.19}$$

The values of A and B were originally defined by van Driest [68] who had developed a similar turbulent skin friction correlation. They are given as:

$$A = \frac{2a^2 - b}{(b^2 + 4a^2)^{1/2}} \qquad \text{and} \qquad B = \frac{b}{(b^2 + 4a^2)^{1/2}} \tag{4.20}$$

with a and b being defined as:

$$a = \sqrt{\frac{\gamma - 1}{2} M_e^2 \frac{T_e}{T_w}} \qquad \text{and} \qquad b = \left(\frac{T_{aw}}{T_w} - 1\right) \tag{4.21}$$

The adiabatic wall temperature is,

$$T_{aw} = T_e + r\frac{U_e^2}{2c_p} \tag{4.22}$$

where the recovery factor for turbulent flow is $r = \sqrt[3]{Pr}$ as given by Dorrance [61]. The remaining factor is to transform the flat plate correlation to one for a cone which is approximately

$$c_{f,cone} = 1.1 c_{f,plate} \tag{4.23}$$

At this point we can relate the turbulent skin friction to the heat flux through Equations 4.7 and 4.9

4.1.3 Single Cone/Wedge Simulations

Simulations are completed of a single wedge or cone geometry for every test case using DPLR2D as packaged within the STABL software suite. DPLR2D is a 2D/axisymmetric reacting compressible Navier-Stokes CFD solver [45]. STABL is the Stability

and Transition Analysis for hypersonic Boundary Layers computational suite which has been developed at the University of Minnesota [69].

Two grids were designed to replicate the fore wedge and fore cone. The grid consisted of 400 streamwise and 400 wall normal grid cells. A grid convergence study was completed to ensure the wall heat flux results were not affected with an increase in the number of grid cells used. A sample grid showing every tenth grid line in the streamwise direction and every twentieth grid line in the wall normal direction shown in Figure 4.1.

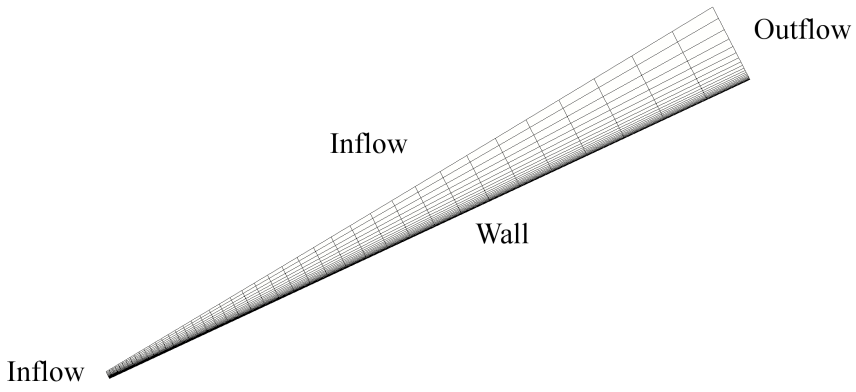

Figure 4.1: Image of cone grid used for viscous single cone simulations used to extract the laminar boundary layer heat flux. Every tenth grid line in the streamwise direction and every twentieth grid line in the wall normal direction is shown.

To solve for a specific case the freestream density, temperature, vibrational temperature, velocity, and gas mass fractions are entered into the solver input file. The left and top boundaries are an inflow boundary condition and set to freestream values. The bottom boundary is set to be a no-slip isothermal wall with wall temperature of 300 K. The right boundary is set to be an zero-gradient outflow condition.

The solution is considered converged when the root mean square of the density residual reaches less then 1×10^{-12}. After the solution is converged, the post-processing function outputs a file in Tecplot format and is viewed using Paraview. A sample image of the pressure and temperature fields is shown in Figure 4.2. The wall heat flux is calculated using the STABL post-processing software and is saved into a

csv data file to be used when plotting the experimental mean heat flux.

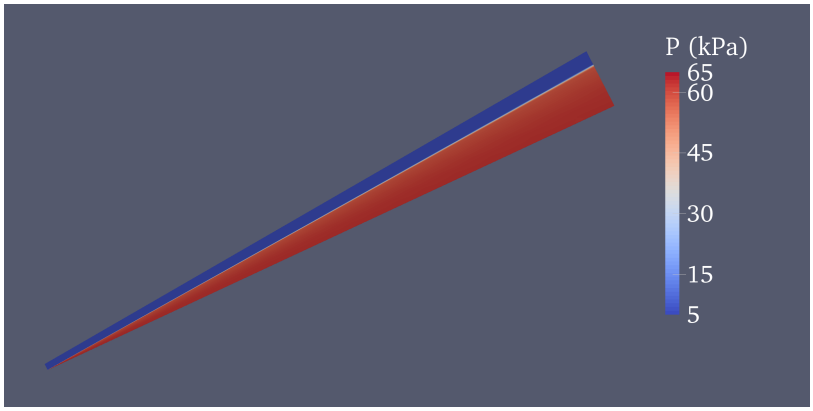

(a) Pressure

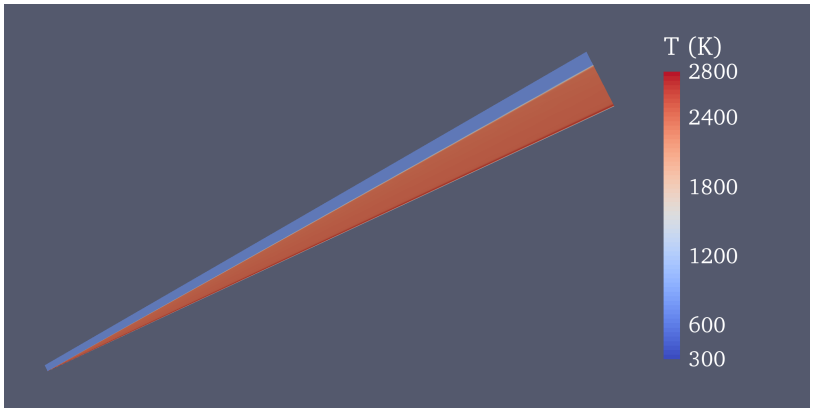

(b) Temperature

Figure 4.2: Pressure and temperature fields from DPLR of shot 2853.

4.2 Mean Heat Flux Double-Wedge

New heat flux measurements for the double-wedge are completed in T5. These new measurements are compared with previous HET experimental results of Swantek [34]. Since the same model was used in the two facilities we can easily quantify differences due to the change in facility and run condition.

The T5 double-wedge mean heat flux results for air are shown in Figure 4.3. Each individual symbol indicates the mean heat flux for one of the thermocouples. The error bars indicate the mean heat flux uncertainty as described in Section 2.4.1.

Additionally, shadowgraph images with thermocouple locations indicated are included for each case to make comparisons between the heat flux and flow structures easier.

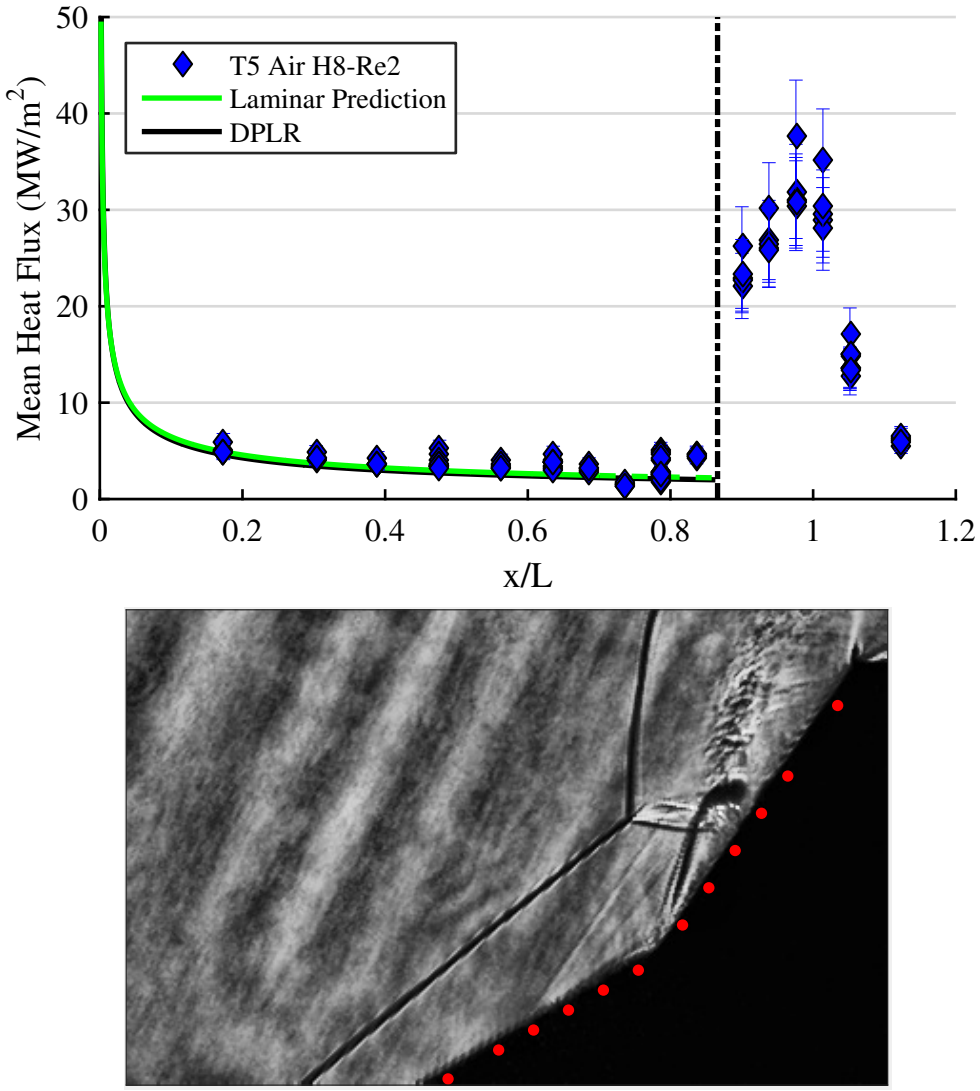

Figure 4.3: Mean heat flux and labeled shadowgraph for the H8-Re2 air condition with the double-wedge in T5. Shadowgraph from shot 2851.

The mean heat flux shows a laminar boundary layer on the front wedge through the first seven thermocouples. At this point the heat flux response drops due to the flow separation. This separation location is in agreement with the shadowgraph images as the separation shock is seen emanating between the seventh and eighth thermocouples. The heat flux level rises through the separation region. A large

increase in heat flux is observed due to the flow reattaching just downstream of the first thermocouple on the aft wedge. The heat flux continues to rise over the aft wedge and peaks at the thirteenth thermocouple. The transmitted shock that impinges on the surface near this thermocouple is the likely cause of the augmented heat flux.

The mean heat flux is compared with the double-wedge results from the HET in Figure 4.4. The heat flux is nondimensionalized by the Stanton Reynolds number relation using freestream conditions as typically done when comparing heat flux,

$$St_\infty \sqrt{Re_\infty} = \frac{\dot{q}}{\rho_\infty u_\infty (h_0 - c_p T_w)} \sqrt{\frac{\rho_\infty u_\infty x}{\mu_\infty}} \tag{4.24}$$

where $\dot{q}$ is the measured heat flux. With this nondimensionalization good agreement is found between the HET and T5 heat flux for the laminar region.

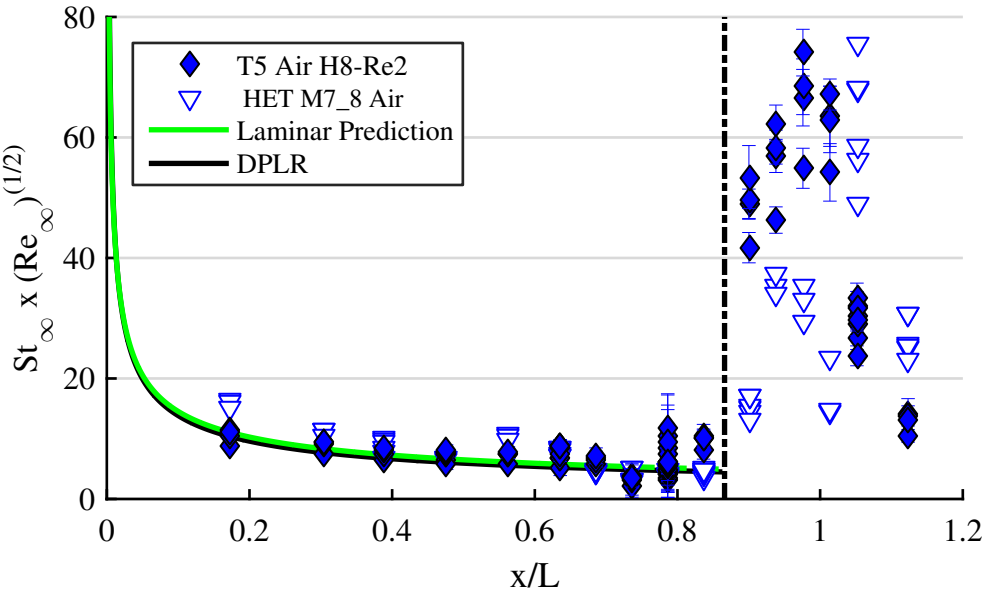

Figure 4.4: Normalized mean heat flux for double-wedge in T5 and the HET.

The mean heat flux results for the H8-Re2 nitrogen experiments with the double-wedge are shown in Figure 4.5. Again the first four to five thermocouples appear to show heat flux levels in agreement with the laminar boundary layer prediction. However, there is a markedly different heat flux response within the separated region. There is no obvious drop in heat flux indicating a boundary layer separation. Instead

there is a large increase in heat flux with a steady rise through the hinge to the thirteenth thermocouple where peak heating is found. Peak heating is located at the same location as the air condition but the magnitude is lower. The heat flux then drops in a similar manner to the air case.

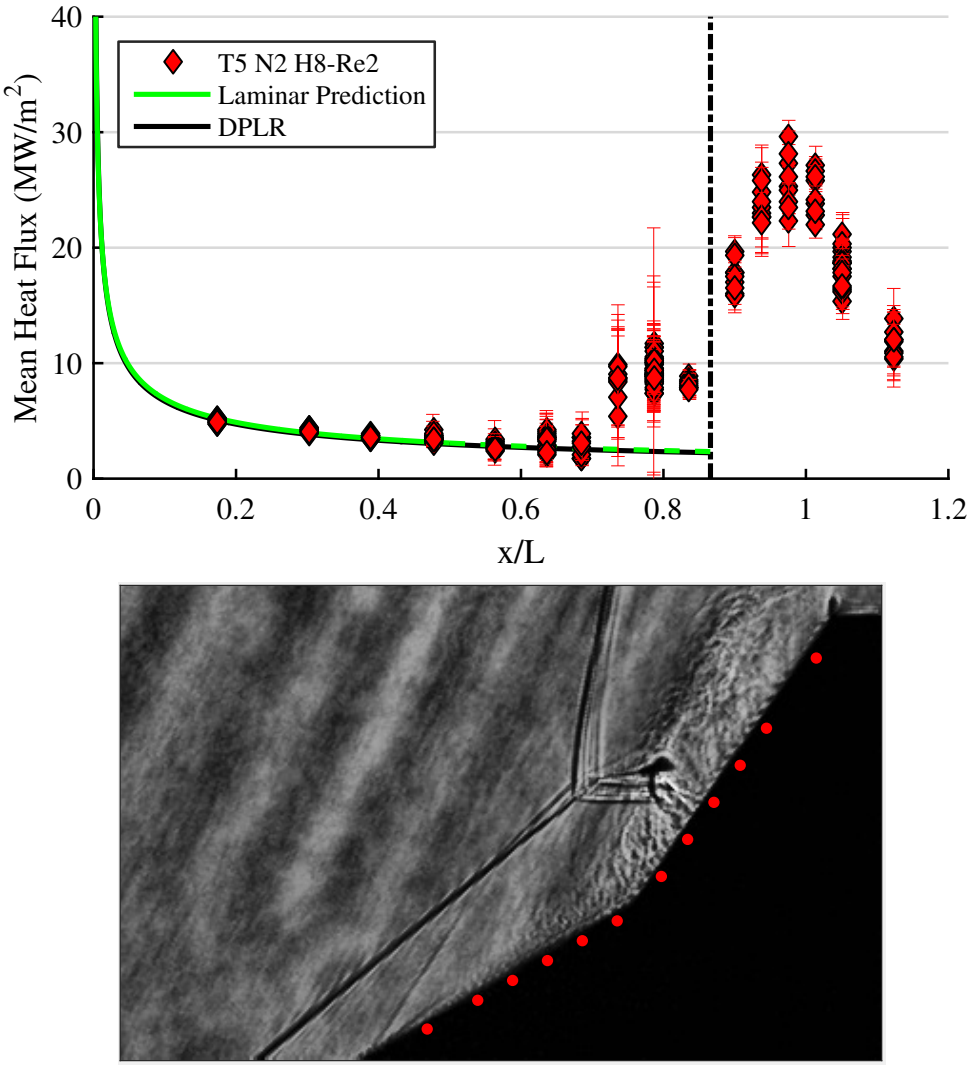

Figure 4.5: Mean heat flux and shadowgraph for the H8-Re2 N2 run condition with the double-wedge in T5. Shadowgraph from shot 2852.

A large difference is clearly seen in the shadowgraph image of the "established" flow field of the nitrogen condition when compared to the air. First, while the thermocouples indicate a laminar boundary layer, it is obvious from the shadowgraph movies that the separation location does not remain at one location throughout the test. The

fluctuations in the fourth and fifth thermocouples are up to five times larger than the fluctuations in the first three thermocouples. The separation location, or some spanwise portion of it, moves upstream and fades away several times throughout the test coinciding with the large fluctuations. The nature of the separated boundary layer is noticeably different for nitrogen than in air. The initial laminar boundary layer is seen to rapidly grow in size and large turbulent structures grow as it turns upward at the hinge.

In his thesis, Davis [47] includes shadowgraph and holographic interferogram images with heat flux measurements for double-wedge experiments completed in T5. The shot most similar to the present model configuration and nitrogen run condition is shot 1750. The image shows a clearly defined separation and reattachment shock. Additionally, there is no large increase in the heat flux after separation as in the current data. As Davis points out, these facts point to a steady flowfield.

While the cause for this discrepancy between the current and historical data is currently unresolved, two possible explanations are as follows. First, the unsteady separation may have remained undiscovered without the high-speed images that were taken in the present experiments. The unsteady separation may be present in the historical data but just not apparent through the single frame images. The second possible reason for the discrepancy may be due to the size of the model. While the current double-wedge model and Davis's model have the same aspect ratio, the overall size of the current model is smaller. The narrower model may allow finite span effects that have a larger impact on the flowfield compared to Davis's model.

4.3 Mean Heat Flux Double-Cone

Heat flux measurements for both double-cone models are completed in T5 using all three test gases. A total of nine data sets spanning two models, three test gases, and two Reynolds numbers allows for several comparisons to be made. For the 25-55 double-cone, four shots were completed for air and nitrogen at the low Reynolds number condition and two shots were completed for each test gas at the high Reynolds

number condition. For the 25-48 double-cone, two shots were completed for air and nitrogen at the low Reynolds number condition and two shots were completed using air at the high Reynolds number condition. Two carbon dioxide shots for both models were completed.

The heat flux results for each run condition are shown separately below along with a shadowgraph frame with the thermocouple locations indicated. In the mean heat flux figures each individual symbol indicates the mean heat flux for an individual thermocouple and the error bars indicate the standard deviation of the heat flux fluctuations through the steady test time. The thermocouple locations are given as the distance along the model surface normalized by the fore cone face length. The laminar heat flux prediction and DPLR heat flux results are included in the figure as the green and black lines, respectively. The dashed portion of the laminar prediction indicates the separated flow region as measured from the shadowgraph images. Additionally, the vertical dashed line indicates the hinge location. The shadowgraph images are labeled with the thermocouple locations. As the shadowgraph image focuses on the corner region several thermocouples for both models are not visible. Unless otherwise noted the field of view for the images in this section are approximately $42.8\,\mathrm{mm} \times 26.8\,\mathrm{mm}$.

As with the previous chapter we will first show the results for the 25-48 double-cone and then the 25-55 double-cone as the Type VI interaction has a simpler influence on the surface heat flux. Experiments were originally completed with the 25-55 double-cone which featured thermocouples located along the fore and aft bodies. The 25-48 model was created later to study the effects due to a reduced flap angle. Initial results with the 25-55 double-cone showed that the laminar prediction was sufficiently accurate for the fore-cone when compared to the measured heat flux. Additionally the separation location could be accurately measured using the shadowgraph images and was in agreement with the separation location as indicated by the heat flux drop. As the fore-body of this 25-48 model was identical to the 25-55 model, it was decided to only instrument the aft-body. Laminar predictions and DPLR heat flux results are included in the figures to anchor the aft heat flux results for the 25-48 double-cone.

The H8-Re2 nitrogen heat flux results are shown in Figure 4.6 with the correspond-

ing shadowgraph image shown below the plot. A sharp rise in heat flux corresponding to the flow reattachment is seen between the first and second thermocouple. The peak heat flux for the 25-48 double-cone is shown in Table 4.1. Included in the table is the location of peak heating and the standard deviation of the heat flux at that thermocouple during the test time. Peak heating for nitrogen is located at the second thermocouple. The heat flux experiences a steady relaxation in value through the fourth thermocouple. There is a drop in heat flux at the fifth thermocouple which is located close to where the expansion wave can be seen to interact with the model surface. The expansion wave reflects off of the model surface and interacts with the shear layer. The heat flux level remains approximately constant through the remaining thermocouples.

Table 4.1: Mean peak heat flux levels for T5 25-48 double-cone.

Condition	Shot	TC #	s/L	q_{peak} MW/m^2	σ_{peak} MW/m^2
H8-Re2 N2	2876	2	1.111	21.71	1.69
	2877	2	1.111	22.24	1.32
H8-Re2 Air	2878	2	1.111	18.51	1.89
	2879	2	1.111	20.37	1.95
H8-Re2 CO2	2880	2	1.111	21.58	2.77
	2881	2	1.111	20.96	1.21
H8-Re6 Air	2882	1	1.056	64.94	5.32
	2883	1	1.056	90.04	7.40

A notable feature seen in the shadowgraph image is the Kelvin-Helmholtz vorticies that emanates from the primary triple point. These vorticies appear approximately 3.5 mm downstream of the triple point roughly between the fifth and sixth thermocouples and continuously forms during the test. However no correlation between the breakdown and the heat flux results is readily observed. The spectral content of the heat flux shows no distinct peak that may correspond with the observed shear layer breakdown.

The H8-Re2 air heat flux results are shown in Figure 4.7. The heat flux signature is similar to the nitrogen case, however, the measured peak heat flux is lower than

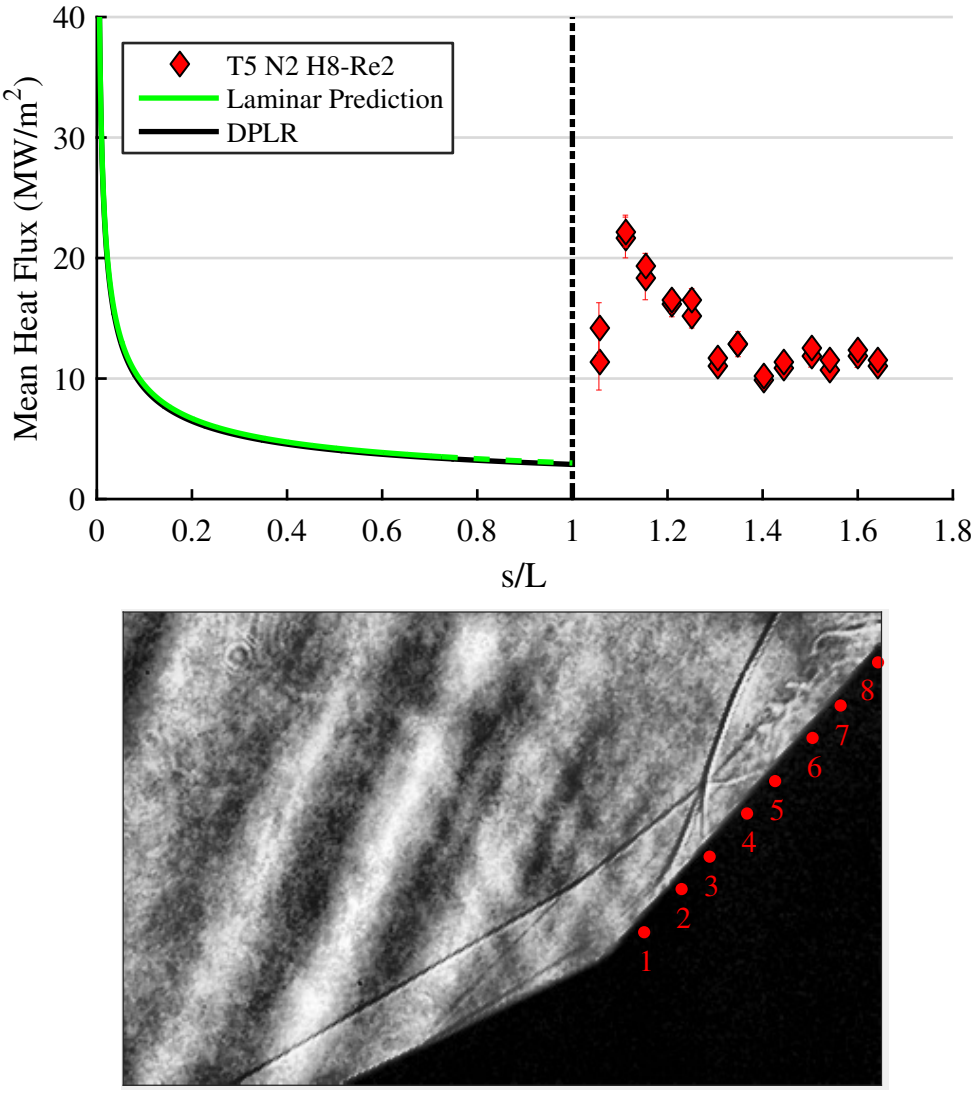

Figure 4.6: Heat flux and labeled shadowgraph for the H8-Re2 nitrogen run condition with the 25-48 double-cone. Shadowgraph from shot 2877.

the nitrogen case and the peak is not as well defined. In this case the mean peak heat flux is measured at the third thermocouple but there is less than 2% difference between the second and third thermocouples. For comparison, there is up to a 17% difference between the second and third thermocouples for the nitrogen condition. This may indicate that the separated boundary layer from the front cone may not have completely reattached at this point. Absent other flow interactions, the heat flux level should begin to drop after it reattaches to the aft cone surface. The heat flux levels decrease through the fifth thermocouple as would be expected by a laminar boundary layer. The heat flux level drops between the fifth and sixth thermocouples, again due to the expansion wave emanating from the triple point. The reflected expansion is not nearly as strong as the nitrogen case and only occasionally appears in the shadowgraph images. Lastly, the heat flux recovers to the same level as in the nitrogen case.

The H8-Re2 carbon dioxide heat flux results are shown in Figure 4.8. This heat flux response is very similar to the air case but at a slightly higher level. The measured peak heating is only slightly lower on average than the nitrogen condition. There is a large drop in the heat flux level in between the fifth and sixth thermocouple due to the expansion wave.

The H8-Re6 air heat flux results are shown in Figure 4.9. Peak heating occurs at the first thermocouple which is also where the reattachment location is located. The heat flux relaxes over the next three thermocouples similar to the low Reynolds number conditions. The expansion wave interacts with the surface between the fourth and fifth thermocouples. A significant drop in heat flux is observed after the expansion. The percentage rise in heat flux through the remaining thermocouples is small at 5% compared to the lower Reynolds number case at 14%.

The 25-55 double-cone results are considered next. First, each individual case is described and then an analysis of effects due to changes in the gas composition and Reynolds number is performed. The peak mean heat flux for the 25-55 double-cone is also tabulated for each shot, see Table 4.2. However, the strong type V interaction obscures the peak heat flux due to the reattaching boundary layer. Instead the

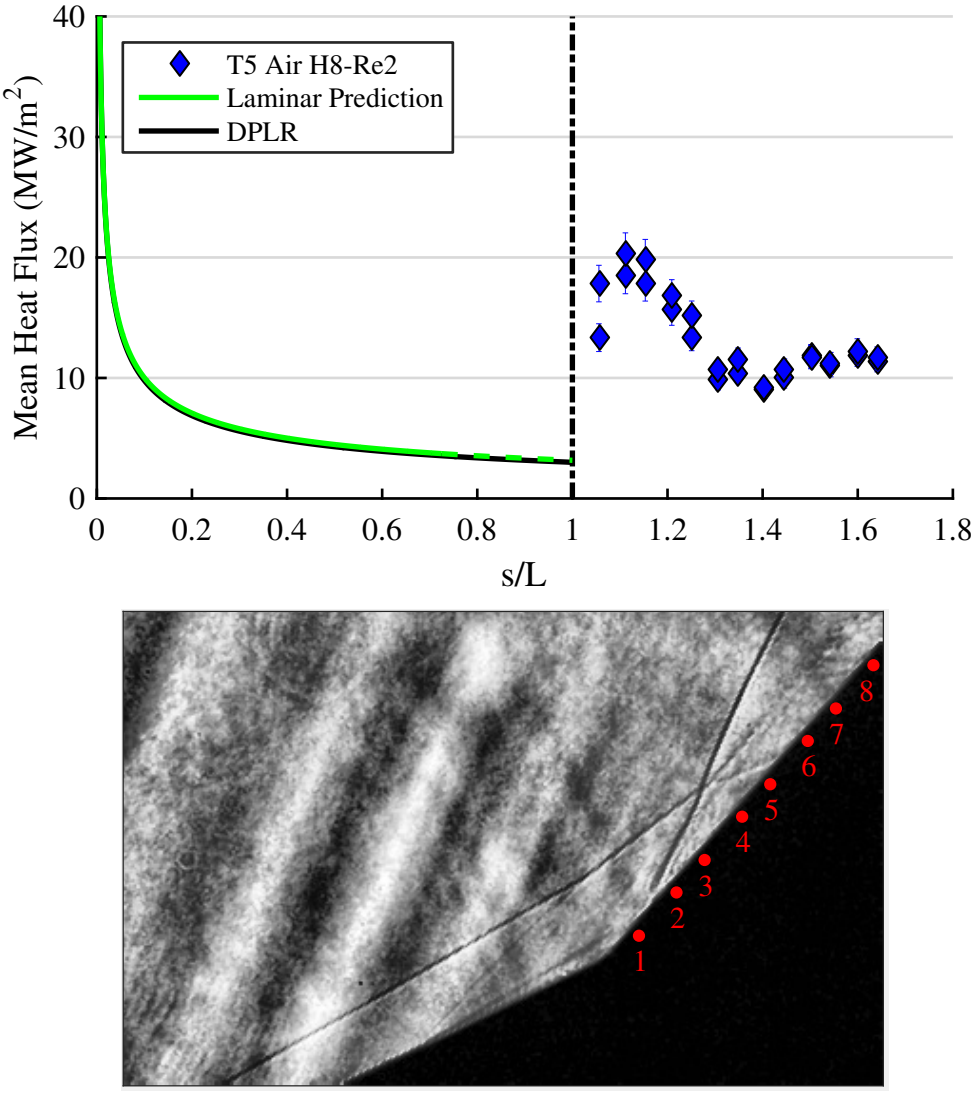

Figure 4.7: Heat flux and labeled shadowgraph for the H8-Re2 air run condition with the 25-48 double-cone. Shadowgraph from shot 2879.

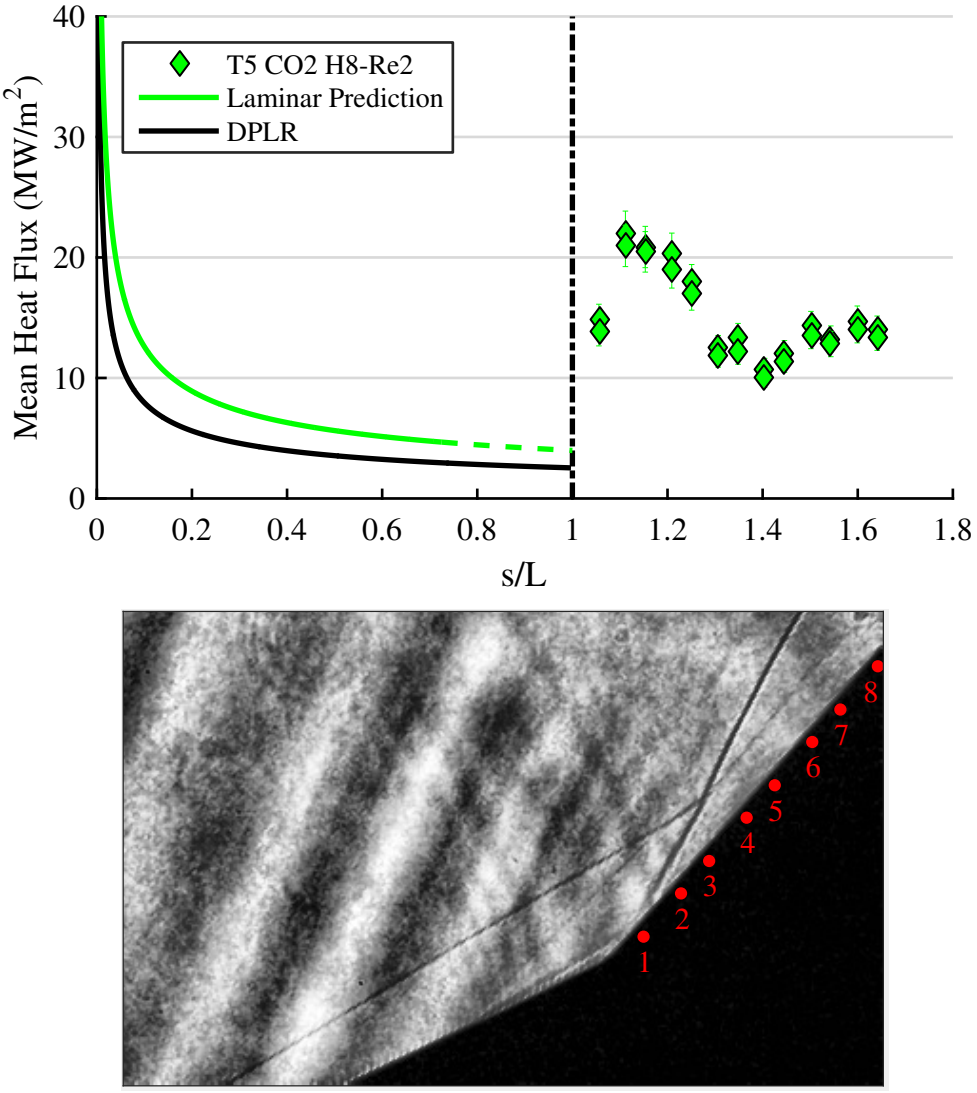

Figure 4.8: Heat flux and labeled shadowgraph for the H8-Re2 carbon dioxide run condition with the 25-48 double-cone. Shadowgraph from shot 2881.

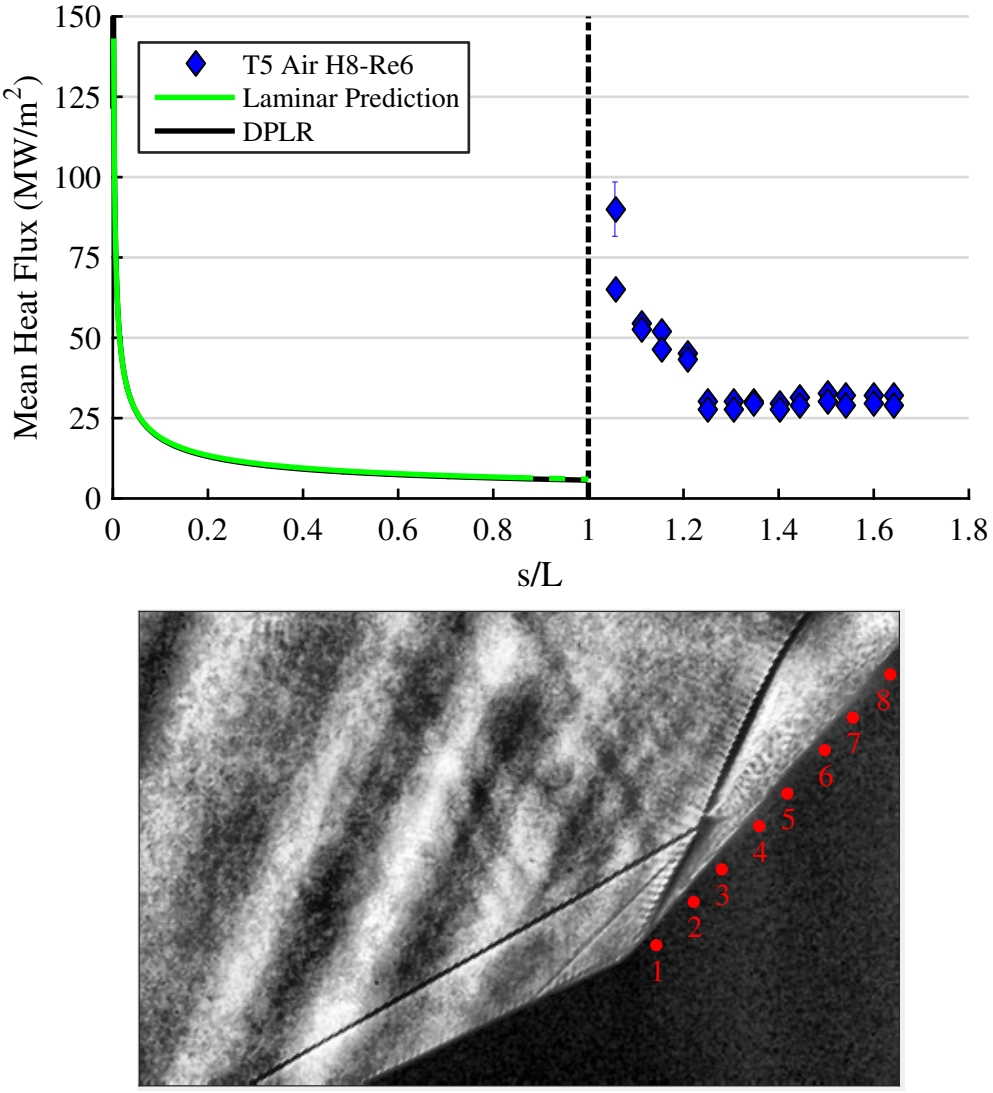

Figure 4.9: Heat flux and labeled shadowgraph for the H8-Re6 air run condition with the 25-48 double-cone. Shadowgraph from shot 2882.

Table 4.2: Measured peak mean heat flux level for T5 25-55 double-cone. The highest heat flux due to the reattaching boundary layer is included if it is lower than the peak heat flux in the last three columns.

Condition	Shot	TC #	s/L	q_{peak} MW/m^2	σ_{peak} MW/m^2	TC # reattach	$q_{reattach}$ MW/m^2	$\sigma_{reattach}$ MW/m^2
H8-Re2 N2	2853	A11	1.127	56.3	10.21	B10	29.8	7.58
	2854	A11	1.127	58.0	10.59	C10	36.0	4.59
	2855	A11	1.127	55.7	10.39	B10	37.9	6.20
	2856	A11	1.127	54.8	8.94	C10	32.1	5.82
H8-Re2 Air	2857	A12	1.196	32.8	6.99	B10	29.4	7.45
	2858	D10	1.060	32.2	4.70	–	–	–
	2859	D11	1.127	31.3	11.86	C10	30.3	4.96
	2860	B11	1.127	30.3	1.86	D10	27.9	4.46
H8-Re2 CO2	2874	C10	1.060	31.2	5.27	–	–	–
	2875	C10	1.060	40.2	7.43	B10	30.7	5.84
H8-Re6 N2	2862	C10	1.060	115.1	6.66	–	–	–
	2864	C10	1.060	126.7	10.62	–	–	–
H8-Re6 Air	2861	B11	1.127	96.5	8.59	C10	91.7	4.92
	2863	B11	1.127	116.4	9.57	C10	106.9	5.57

peak is located somewhere near the impinging shock. If the peak heat flux due to the reattaching boundary layer is not the peak heat flux, it is also measured and included. In addition, as will be discussed below, the actual peak heat flux is highly localized and may not be captured due to the finite measurement region of the thermocouple. Thus we must note that the peak heat flux tabulated must be considered a minimum level of peak heating. Thus it is not necessarily an error if a simulation predicts higher peak heat flux.

First shown in Figure 4.10 is the mean heat flux for the N2 H8-Re2 condition. The heat flux along the fore cone follows a square root dependence indicative of a laminar boundary layer. Indeed, good agreement is observed between the first five thermocouples and the theoretical and DPLR results. The mean heat flux drops between the fifth and sixth thermocouple indicating that separation has occurred. Observation of the separation location is also made in the labeled shadowgraph image. In the separation region the heat flux level rises toward the hinge location. The separation reattaches to the aft cone near the tenth thermocouple and results in an increase in heat flux. During startup the heat flux at this thermocouple is higher

than during test time due to the reattachment initially occurring closer to the hinge. The peak in heat flux is seen at the eleventh thermocouple which is located just downstream of the impingement. The heat flux level drops drastically for the last five thermocouples.

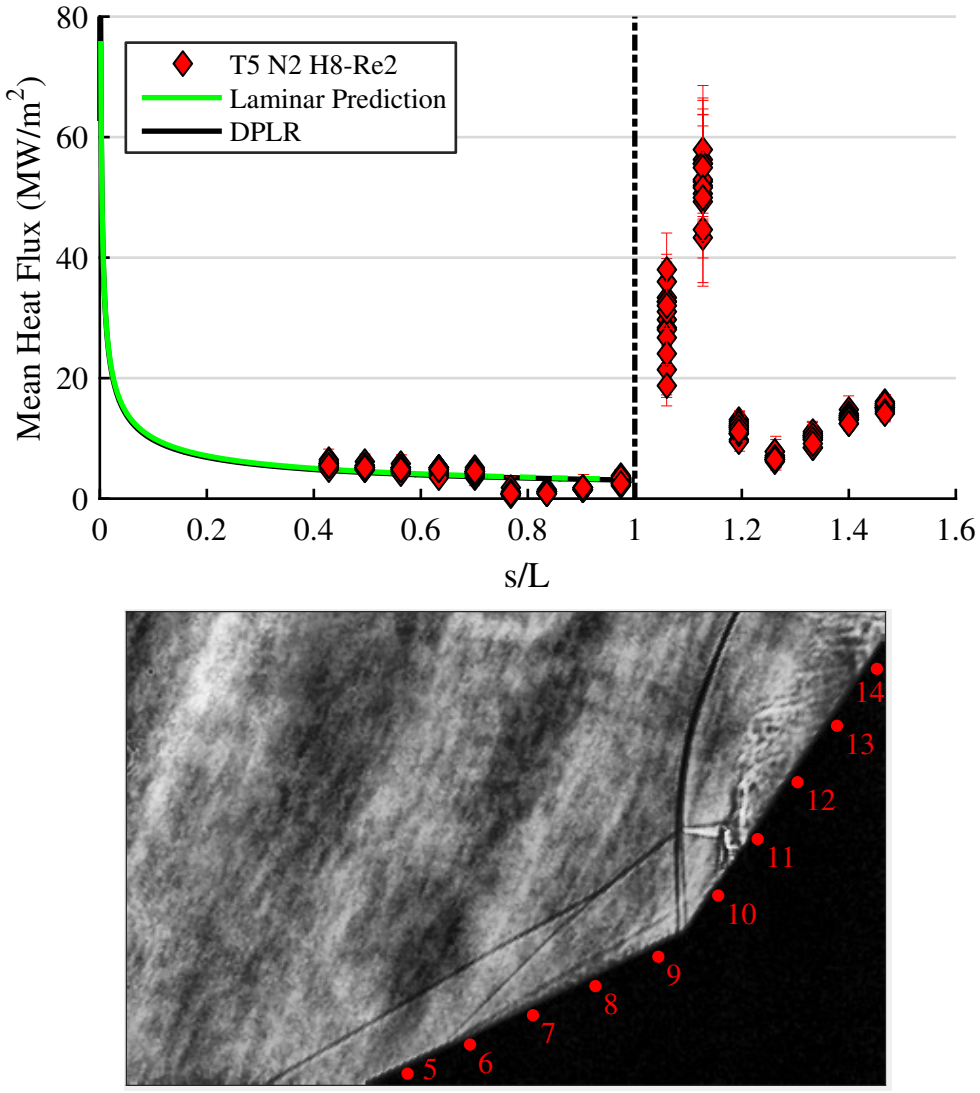

Figure 4.10: Heat flux and labeled shadowgraph for the H8-Re2 nitrogen run condition with the 25-55 double-cone. Shadowgraph from shot 2856.

The mean heat flux results for the high pressure nitrogen shots are shown in Figure 4.11. In this shot we again see good agreement of the laminar boundary layer heat flux with theory and computational results. The boundary layer separation oc-

curs closer to the hinge for this case and only two thermocouples on the fore cone are located in the separation region, in agreement with the shadowgraph image. The separated boundary layer also reattaches closer to the hinge such the first aft thermocouple is located in the post-reattachment and impingement shock region. Due to the small size of the shock structure it is difficult to determine what is directly above the thermocouple. The heat flux drops and recovers similar to the low pressure case.

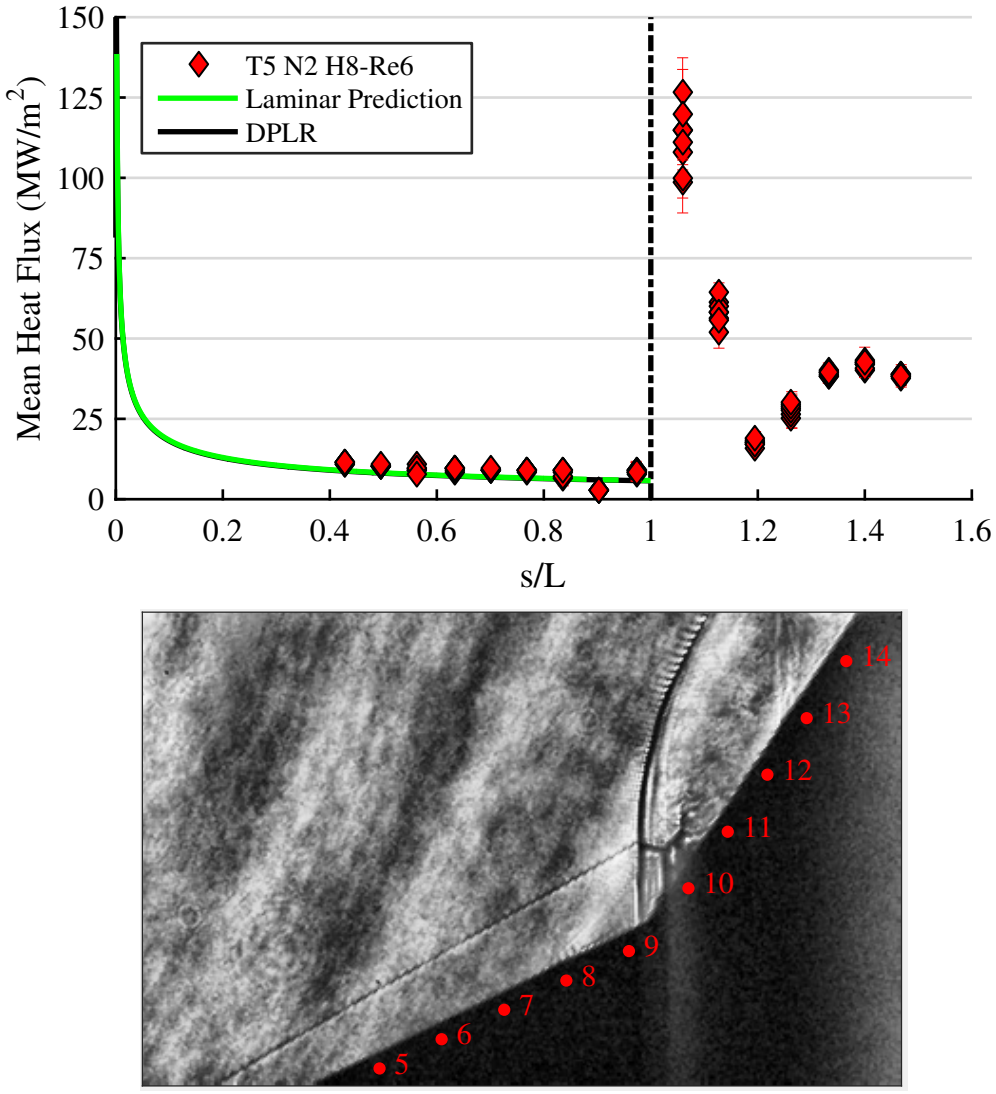

Figure 4.11: Heat flux and labeled shadowgraph for the H8-Re6 nitrogen run condition with the 25-55 double-cone. Shadowgraph from shot 2862.

In Figure 4.12 the mean heat flux and shadowgraph image of the H8-Re2 air case

is shown. Again the laminar boundary layer shows good agreement with theory and DPLR results. Separation occurs in between the fifth and sixth thermocouples as seen by the drop in heat flux. This is also observed in the labeled shadowgraph image. The heat flux level increases as the thermocouples get closer to the hinge. The first three thermocouples on the aft cone have a constant heat flux level. The reattachment has shifted up the aft cone and begins just downstream of the tenth thermocouple. For this case we can also easily observe the impingement shock in between the eleventh and twelfth thermocouple. The heat flux level drops significantly for the last four thermocouples.

Figure 4.13 shows the mean heat flux and shadowgraph image of the H8-Re6 air case. Again, good agreement of the laminar boundary layer heat flux with theory and computational results is seen for this condition. As with the high pressure nitrogen condition, the separation occurs ahead of the eighth thermocouple resulting in the decrease in heat flux as this location. The first two thermocouples on the aft cone have a constant heat flux level. The boundary layer reattachment occurs just upstream of the tenth thermocouple. For this case we can also easily observe the impingement shock near the eleventh thermocouple which results in peak heating occurring near this thermocouple. The heat flux level drops significantly for the last five thermocouples.

The H8-Re2 carbon dioxide heat flux results are shown in Figure 4.14. This overall heat flux response is very similar to the air case but at a slightly higher level. The measured reattachment heating is only slightly lower on average than the nitrogen condition and slightly higher than the air condition.

Comparison of mean heat flux results between air and nitrogen at the same nominal test condition is shown in Figures 4.15 and 4.16. The mean heat flux in the laminar boundary layer is in agreement between air and nitrogen. In both figures the theoretical and DPLR results are for the nitrogen condition. The heat flux in the separated region are in good agreement with each other. The two conditions are also in agreement on the aft cone for the last four thermocouples.

The main area where the mean heat flux results diverge between the two gases for

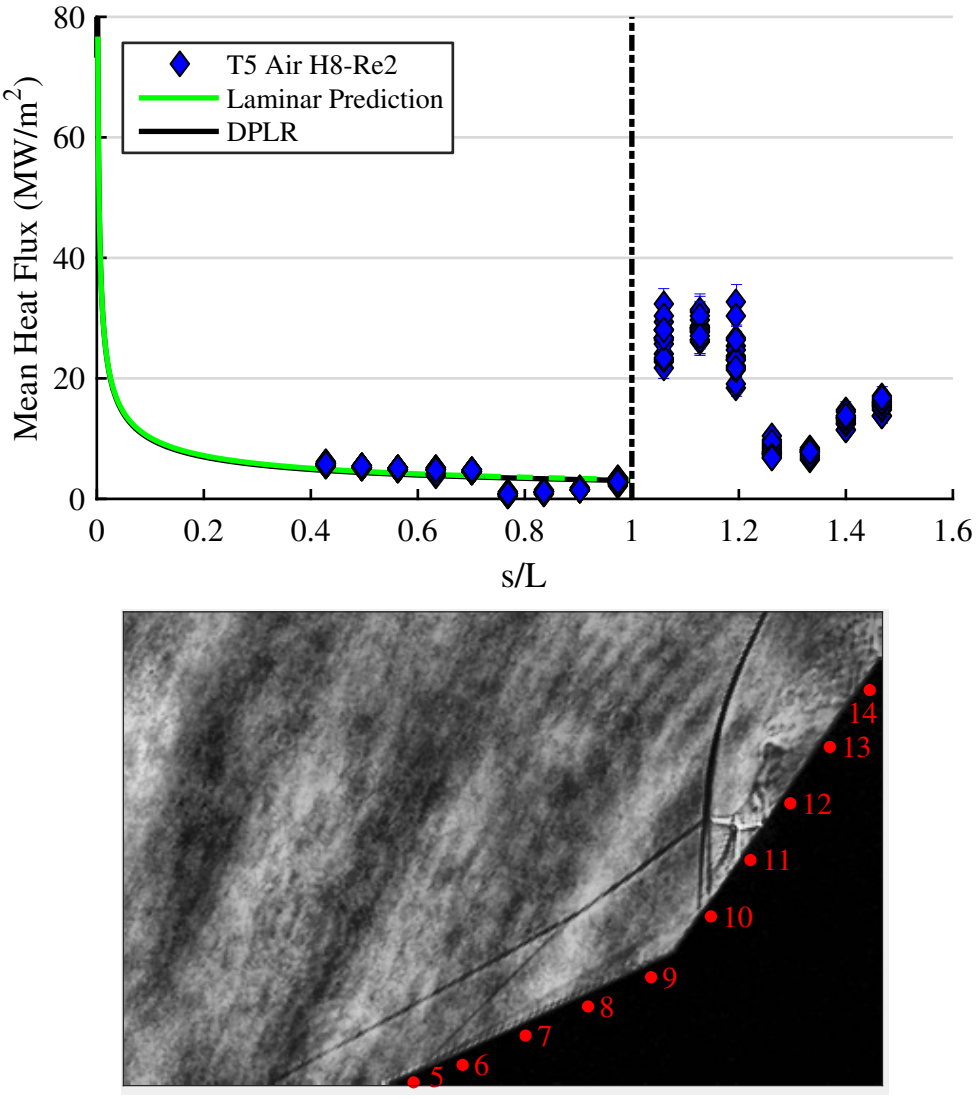

Figure 4.12: Heat flux and labeled shadowgraph for the H8-Re2 air run condition with the 25-55 double-cone. Shadowgraph from shot 2860.

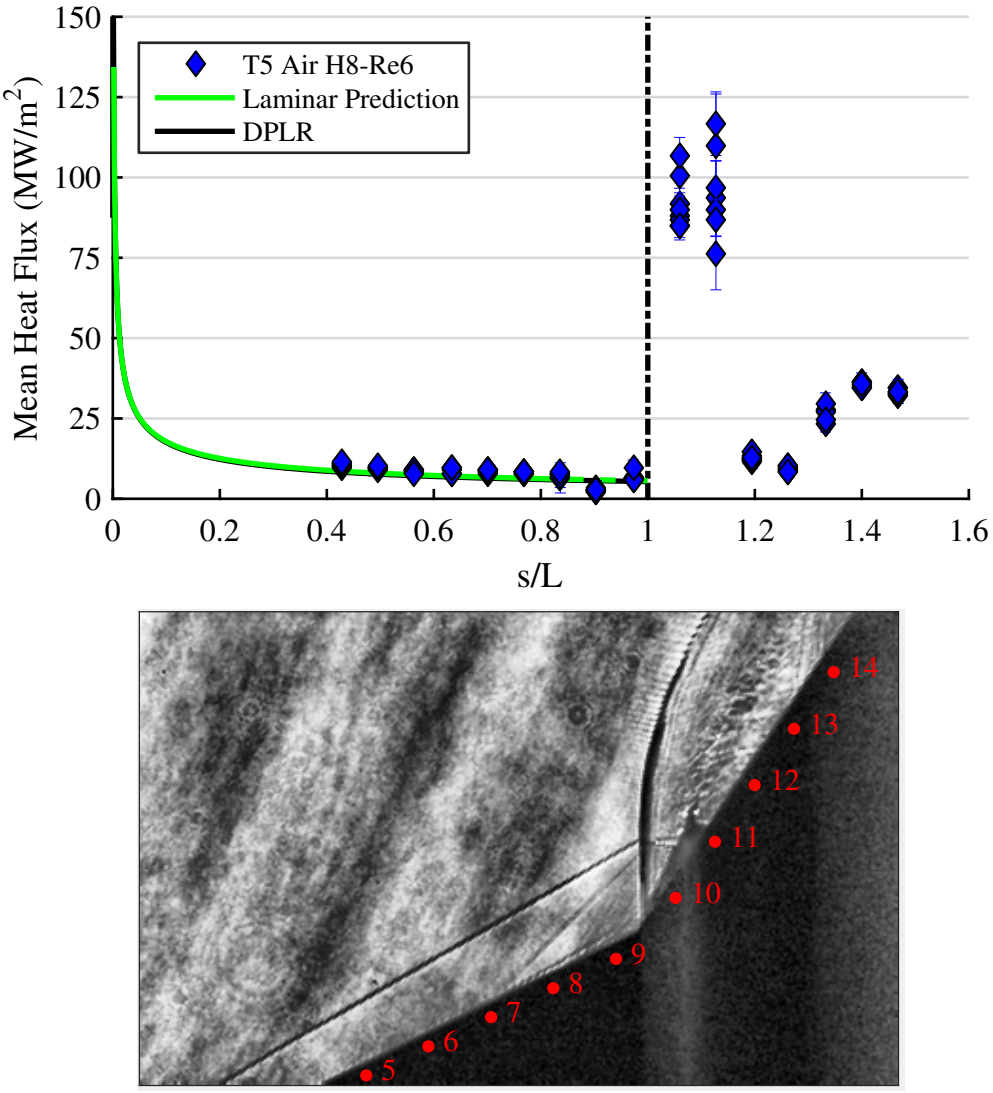

Figure 4.13: Heat flux and labeled shadowgraph for the H8-Re6 air run condition with the 25-55 double-cone. Shadowgraph from shot 2861.

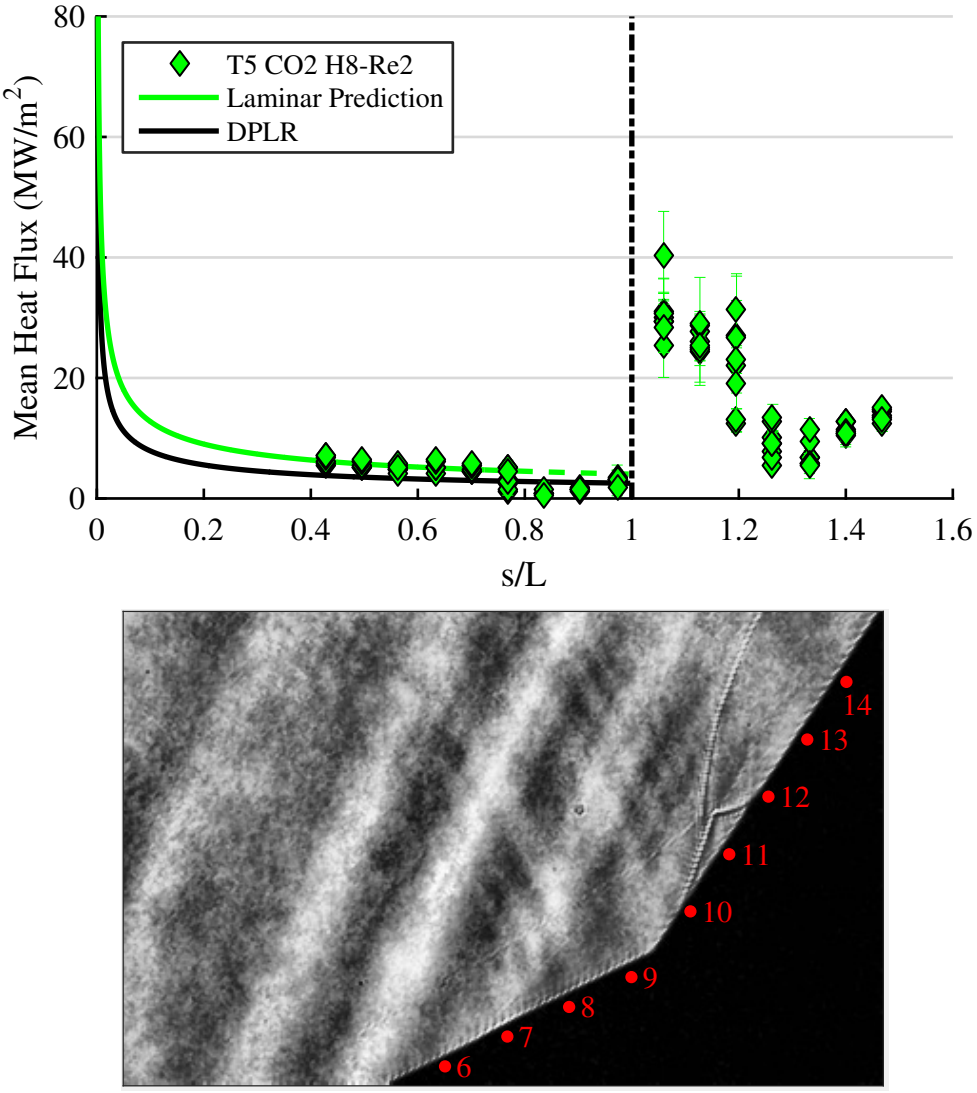

Figure 4.14: Heat flux and labeled shadowgraph for the H8-Re2 carbon dioxide run condition with the 25-55 double-cone. Shadowgraph from shot 2875.

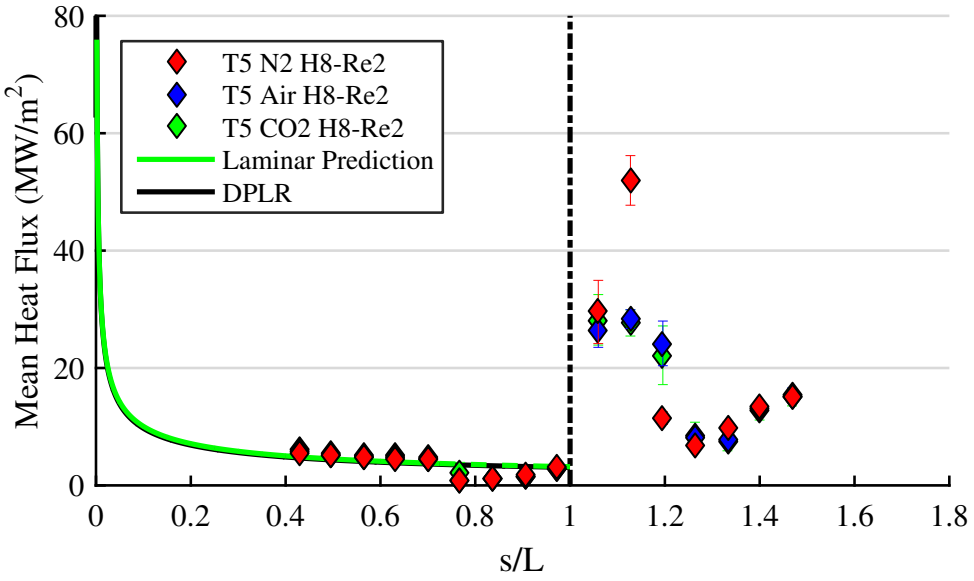

Figure 4.15: Mean heat flux comparison of gas composition for the H8-Re2 condition with the 25-55 double-cone. The laminar prediction and DPLR results are based on the air condition. The symbols are the mean of the mean heat flux values for a given gas composition and the error bars indicate the standard deviation of the mean heat fluxes.

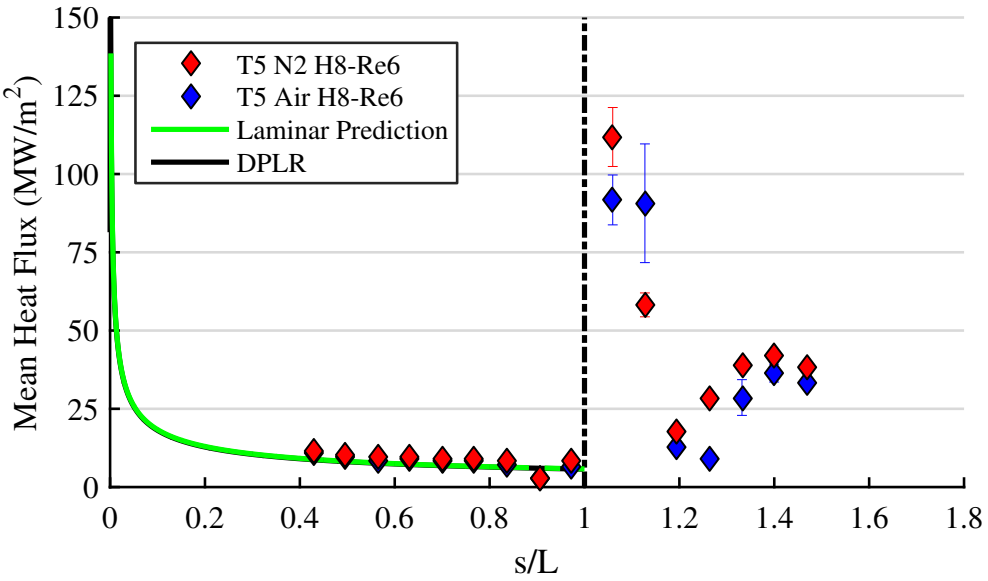

Figure 4.16: Mean heat flux comparison of air and nitrogen for the H8-Re6 condition with the 25-55 double-cone. The laminar prediction and DPLR results are based on the air condition. The symbols are the mean of the mean heat flux values for a given gas composition and the error bars indicate the standard deviation of the mean heat fluxes.

both test conditions is near peak heating. In the lower Reynolds number case we see the peak heating of nitrogen to be approximately twice the peak heating found in the air condition. This is believed to be due to the fact that the thermocouples measure the heat flux at a discrete location and over a finite area. Peak heating may not be captured by the thermocouple if the heating were to occur sufficiently far enough away from the measurement area. Thus with these experimental results we can make a statement on the minimum peak heating value. However, the true peak heating value may actually be higher than what is reported. When comparing computational results, it is not necessarily an issue if the computational peak heat flux is higher than the experimental heat flux. Instead, the simulation should be compared to the experimental heat flux at the location of the gauges. At that location, the data should match.

A demonstration of how the location of the shocks may make a big difference to the peak heating measured is shown by examining the startup heat flux for the H8-Re2 air condition. The heat flux trace for thermocouple A-11 for shot 2858 is shown in Figure 4.17 with four shadowgraph images focusing on the reattachment region. In the shadowgraph images the red dots are sized to give an approximation for the inner electrode diameter which can be used as an approximation for the area where the measurement is made. In the plot, the four open red circles are matched in time to the four shadowgraph images below. During the startup process the heat flux is measured to rise up to $75\,\mathrm{MW/m^2}$ and remains at this extremely high heat flux level for approximately $100\,\mu\mathrm{s}$. During this time we observe in the shadowgraph images the transmitted shock impinges directly on top of the thermocouple. In Figure 4.17c we see that the transmitted shock has shifted well downstream of the thermocouple. Due to this shift in the shock location we see the heat flux rapidly drops to the test time value of $20\,\mathrm{MW/m^2}$ in less than $100\,\mu\mathrm{s}$. This shows how a small change in the shock location can lead to a large change in the heat flux. It should be noted that the next downstream thermocouple never reaches the same transient heat flux level seen in thermocouple 11.

The difference in peak heat flux between air and nitrogen for the high Reynolds

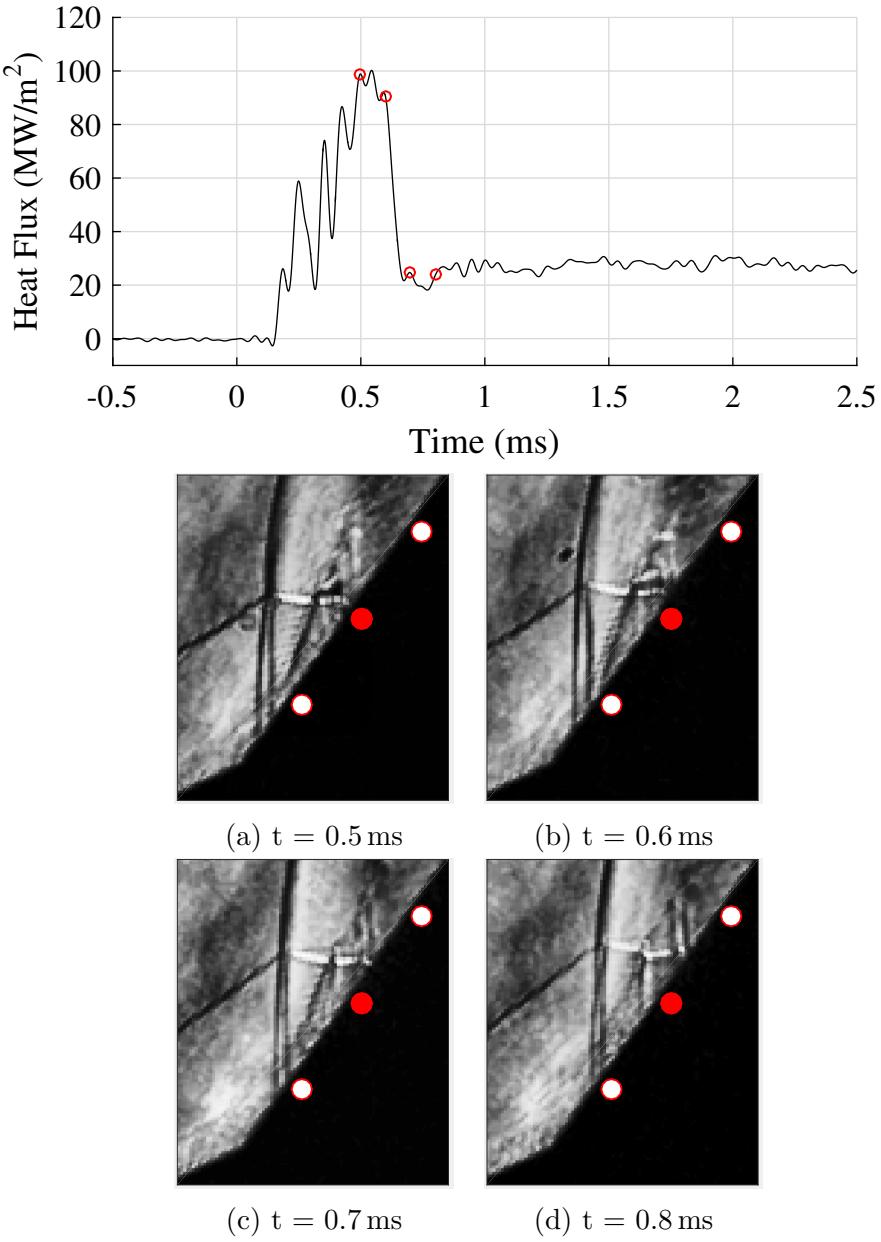

(a) t = 0.5 ms (b) t = 0.6 ms

(c) t = 0.7 ms (d) t = 0.8 ms

Figure 4.17: Shot 2858, Air H8-Re2. On top is the heat flux for the A-11 thermocouple on the double-cone. The open red circles correspond to the shadowgraph images below the plot. Below are four equal time spaced shadowgraph images cropped to the hinge location. The red dots shows the location of the thermocouples and gives an approximation for the diameter of the inner electrode. The plot shows a rapid drop in heat flux between 0.6 ms and 0.7 µs. This corresponds to when the transmitted shock moves downstream and no longer impinges on the model surface at thermocouple 11. The total visible area of each image is approximately 10 mm × 12.5 mm.

number condition can be explained by examining the reattachment and transmitted shock structure. In the nitrogen case the reattachment shock and transmitted shock are located atop the tenth thermocouple. The reattachment shock in the air case is located slightly farther downstream such that it covers both the tenth and eleventh thermocouple. As demonstrated previously, the location of the shocks in relation to the thermocouples can have a significant effect on the measured heat flux. Another contribution to the difference in location of peak heating in the higher Reynolds number cases may be due to the slight configuration change of the reattachment-transmitted shock structure.

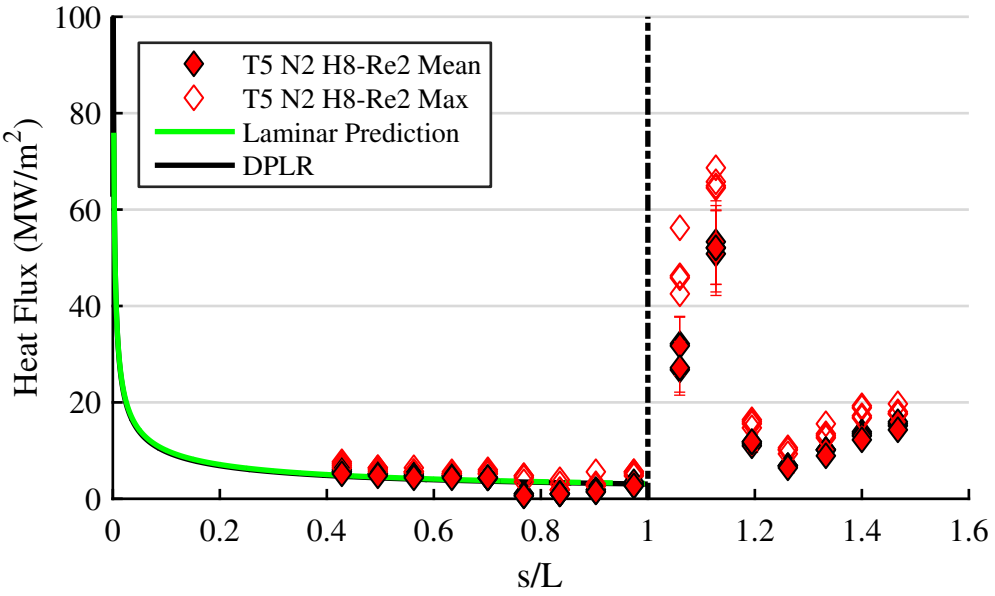

Figure 4.18: Normalized mean heat flux for double-cone in N2 for T5.

The final comparisons for the heat flux can be made by considering changes in Reynolds number while maintaining the same test gas which is shown in Figure 4.20 for nitrogen and in Figure 4.21 for air. The laminar prediction and DPLR results are based on the low Reynolds number condition for both test gases. In these figures the heat flux has been normalized through the Stanton Reynolds number relation used previously in Section 4.2. As expected, performing the normalization collapses the laminar boundary layer heat flux. Additionally, the change in separation length between the conditions is clearly observed. Again the main differences between the

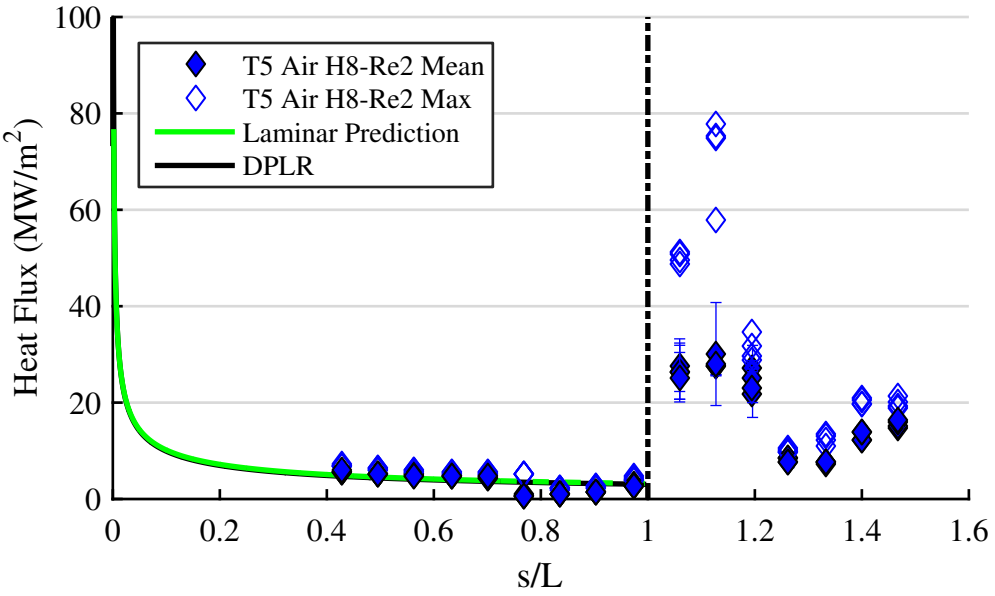

Figure 4.19: Normalized mean heat flux for double-cone in air for T5.

conditions for each gas are found in the peak heating region. For nitrogen the peak heating has the same relative magnitude for the high and low Reynolds number but is located at different thermocouples. This difference in location is simply a matter of the slight difference in the location of the reattachment and transmitted shock locations. However, there are significant differences in the peak heating levels for the air condition with the higher Reynolds number case having normalized peak heating value approximately 2.5 times higher than the low Reynolds number case. The definitive cause of this discrepancy is unclear but one possible reason could again be that peak heating is occurring away from one of the thermocouples.

In summary, mean heat flux results have been presented for the double-wedge in T5 and the HET and the double-cone in T5. The laminar prediction matches well for double-wedge and double-cone for all conditions. Heat flux extracted from DPLR results matches well for air and nitrogen but a discrepancy is observed for carbon dioxide conditions. This discrepancy is observed in previous results [37] and is currently unresolved. The separation location can be determined through the shadowgraph images or the heat flux (with lower resolution).

In the low Reynolds number condition, higher peak heating was observed with the

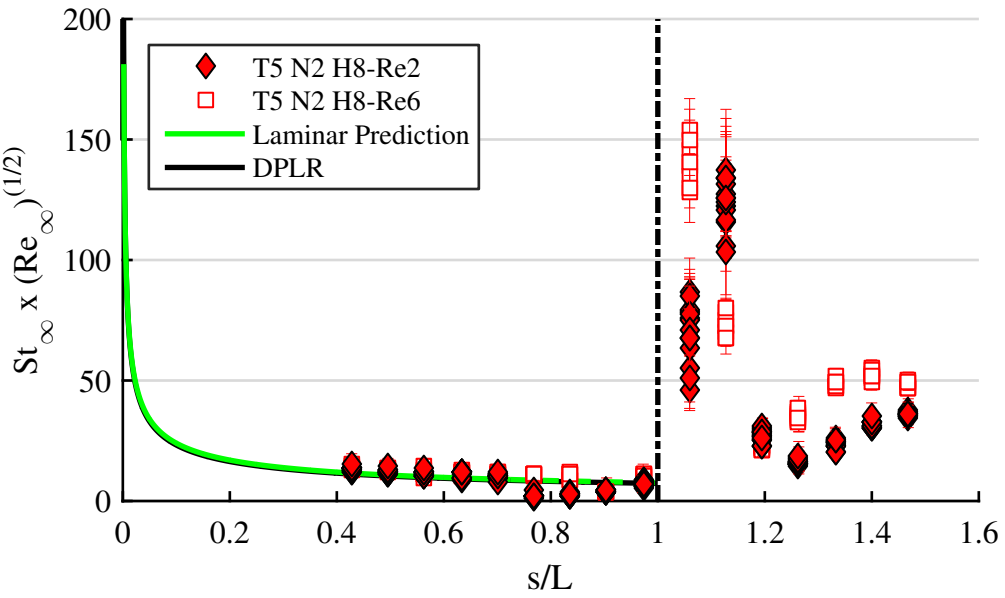

Figure 4.20: Normalized mean heat flux for double-cone in N2 for T5.

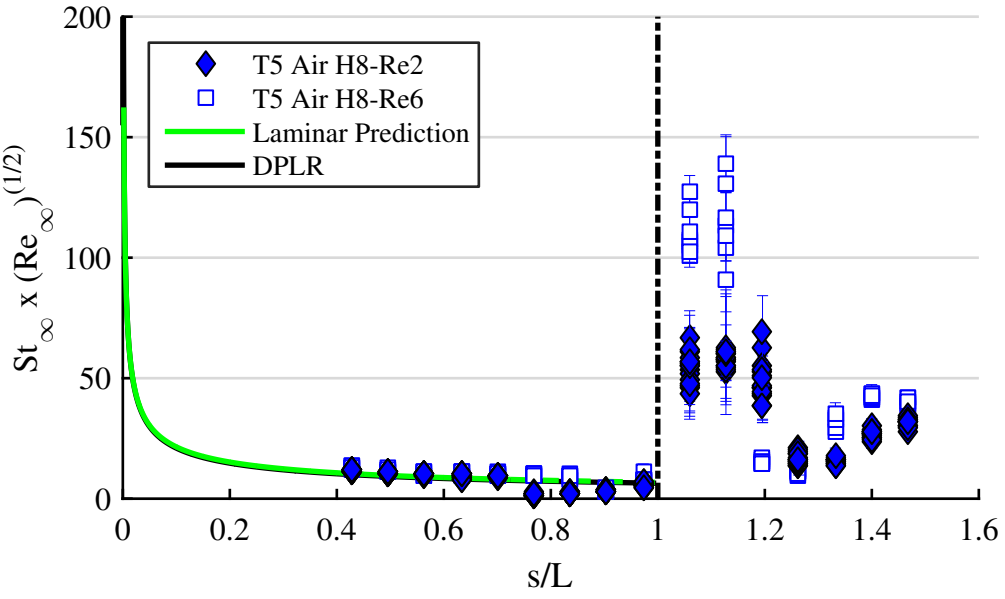

Figure 4.21: Normalized mean heat flux for double-cone in air for T5.

nitrogen test gas due to the impingement shock being located closer to the thermocouples than the air and carbon dioxide condition. At the higher Reynolds number the peak heating was equal between the two gases due to less of a difference in the location of the impingement shock for the air and nitrogen condition. Comparisons were also made by considering a varying Reynolds number. For nitrogen the normalized peak heating values are at the same relative magnitude while the normalized peak heating of air at the higher Reynolds number is approximately twice the lower Reynolds number normalized peak heating. The discrepancy has been shown to be possibly due to insufficient thermocouple resolution in the peak heating region. The shock boundary layer interaction structure is more compact in the nitrogen condition compared to air.

CHAPTER 5

SEPARATION LENGTH ANALYSIS

The separation length is analyzed in the scaling framework developed by Davis and Sturtevant [4] to study thermochemical effects of double-wedge flows. They studied effects that are internal and external to the viscous fluid regions, such as the boundary layer and separated shear layer. The external effects include how freestream dissociation affects the flow. Internal effects include the state of the incoming boundary layer and recombination effects near the wall in the separated region. The progress to the current separation scaling argument has been built on many steps and was specifically designed for the corner separation of a double-wedge geometry.

In this chapter we examine the theory of the separation scaling. Next, the impact of changing to a conical flow is considered. The experimental results for the double-wedge are reported. Lastly, the double-cone results are presented with analysis of geometric and gas composition effects.

5.1 Theory

5.1.1 Control Volume

One important part of modeling separated flow is predicting the pressure rise from separation to reattachment and is explained by Glick [70] as follows. A fluid element located near the separation point has negligible velocity and a total pressure equal to the local static pressure. The fluid element travels along the stagnation streamline to the reattachment point. Once at the reattachment location the fluid particle again has zero velocity but now has an increased total pressure. The increase in total

pressure is due to the work done on the fluid element from the external flow due to mixing within the separated flow.

A momentum balance relating the pressure rise from separation to reattachment to the shear stress within the separated region was made by Sychev [19] who described the flow behind a blunt body. Roshko [18] applied this momentum balance to describe subsonic and supersonic base flows. The model was developed with a backward facing step by considering the momentum balance on the fluid underneath the stagnation streamline. Davis and Sturtevant related this model to the double-wedge geometry. A labeled diagram of the double-wedge flow field is shown in Fig. 5.1 where 1 is the region behind the oblique shock, 2 is the region behind the separation shock and outside the separation region, and 3 is the region behind the reattachment shock. If a rotated frame of reference with respect to the forward wedge is considered, a model for the separation streamline at the hinge is formed by considering the second wedge as a forward step, shown in Fig. 5.2. The equation for the momentum balance of this separation streamline is given as

$$\int_0^{y_R} (p_{\psi^*} - p_2)\,\mathrm{d}y = \int_{x_1}^{x_R} \tau_{\psi^*}\,\mathrm{d}x \tag{5.1}$$

where the shear stress along the walls is neglected. This can be slightly rewritten if we consider a few assumptions. First, the pressure along the streamline is found to be equal to p_2 along a majority of the streamline, rising to the p_R near the reattachment point. Additionally, we assume that p_R scales with p_3 for this flow field. This model for the reattachment pressure has been seen to hold for previous work [4] so its use will be continued in the current work. With these assumptions we can rewrite the equation as

$$\int_{x_1}^{x_R} \left(\mu \frac{\partial u}{\partial y}\right)_{\psi^*} \mathrm{d}x \propto y_R(p_3 - p_2) \tag{5.2}$$

This form of the equation will be used with the triple-deck asymptotic solution to form the separation length scaling relation.

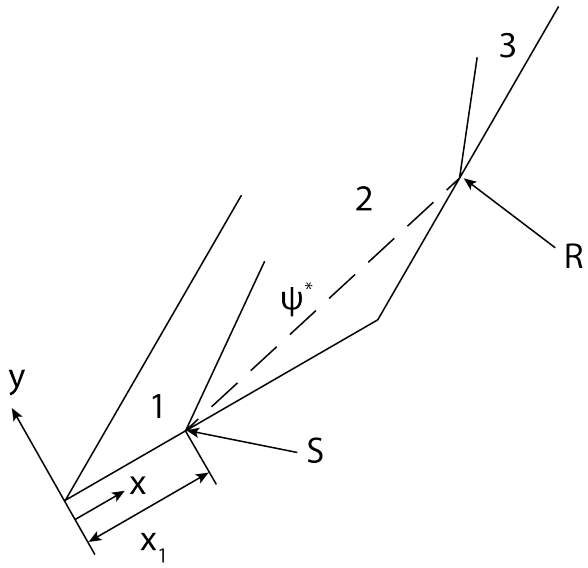

Figure 5.1: Labeled diagram of the double-wedge flow field. This diagram shows only the flow structures relevant to the separation scaling theory.

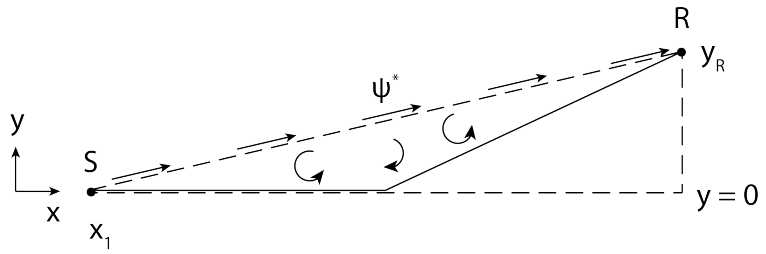

Figure 5.2: Diagram of control volume proposed by Sychev [19] and Roshko [18].

5.1.2 Triple-Deck Asymptotic Theory

Triple-deck theory describes the flow of a laminar boundary layer near a separation point caused by a small disturbance using asymptotic analysis. This theory was first described by Stewartson and Williams [20]. The flow is split into three different regions or "decks": lower, main, and upper. These decks are illustrated in the diagram shown in Fig 5.3. The decks can be described by reducing the Navier-Stokes equations based on scaling arguments. The decks are scaled based on a small perturbation parameter: $\epsilon = Re_{x^*}^{-1/8}$ where x^* is the location of the perturbation.

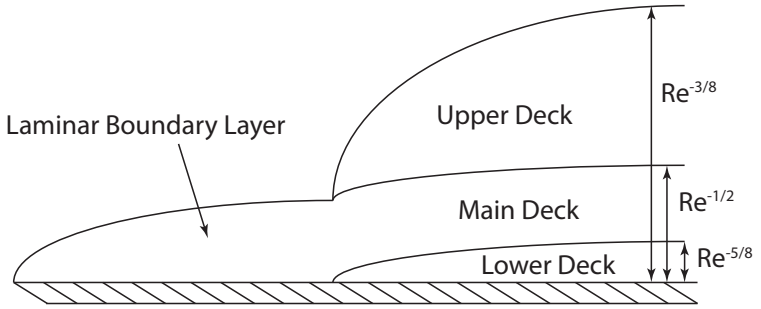

Figure 5.3: Diagram of laminar boundary layer transitioning to triple-deck structure. The names of the decks are shown along with height written in terms of the scaling parameter.

Each deck has its own properties. The upper deck is inviscid and irrotational. The main middle deck is considered inviscid and rotational. The lower deck is viscous and rotational. When the triple-deck problem is solved in a planar two-dimensional frame, the upper and main decks can be solved analytically. The lower deck cannot and must be numerically solved. When the lower deck is reduced it turns into the incompressible boundary layer equations with novel boundary conditions due to the other two decks. The two-dimensional lower deck scaled parameters are shown in Equation 5.4 and Equation 5.5.

The basic idea of triple-deck theory as presented by Stewartson and Williams [20] is as follow. The Navier-Stokes equations are solved in three different regions based on the perturbation parameter, ϵ, above. First, the free interaction region (main deck) is considered. Previous work by Lighthill suggests that the interaction length in the x-direction should be scaled by a factor of ϵ^3 along with other details regarding the

flow structure [71]. Using this scaling factor, the Navier-Stokes equations reduce to inviscid equations for the main deck. The boundary conditions for the main deck are that as $X \to -\infty$ the perturbation terms of the variable expansions go to zero. The boundary conditions for this deck are then used to find values for the expanded u, v, p, and ρ terms (e.g. $u_1 = A_1(X)\frac{\mathrm{d}U_0}{\mathrm{d}Y} + f_1(Y)$ and $v_1 = -U_0(Y)\frac{\mathrm{d}A_1}{\mathrm{d}X}$). The upper deck is analyzed next by considering the limit as $Y \to \infty$ of the main deck results. At this limit we get that both velocity and pressure have second order and higher perturbations.

A final lower deck is needed since boundary conditions for u, v, and ρ for $Y \to 0$ are not specified in the main deck. By considering additional perturbation terms a transformation can be made to reduce the equations to the following

$$\begin{aligned} u\frac{\partial u}{\partial x} + v\frac{\partial u}{\partial y} &= -1/R_0(0)\frac{\mathrm{d}p_2}{\mathrm{d}x} + \frac{\mu_w}{R_0(0)}\frac{\partial^2 u}{\partial y^2}, \\ \frac{\partial u}{\partial x} + \frac{\partial v}{\partial y} &= 0 \end{aligned} \tag{5.3}$$

These equations are then rescaled using the following

$$\begin{aligned} x &= \epsilon^3 a x^*, \\ y &= \epsilon^5 b y^*, \\ p &= p_\infty + \epsilon^2 c p^*, \\ u &= \frac{\epsilon d}{b} u^*, \\ v &= \frac{\epsilon^3 d}{a} v^*, \\ \alpha &= \epsilon^2 \frac{b}{a} \alpha^* \end{aligned} \tag{5.4}$$

where a, b, c, and d are defined as

$$\begin{aligned} a &= x_0 C^{3/8} \lambda^{-5/4} \left(M_\infty^2 - 1\right)^{-3/8} \left(\frac{T_w}{T_\infty}\right)^{3/2} \\ b &= x_0 C^{5/8} \lambda^{-3/4} \left(M_\infty^2 - 1\right)^{-1/8} \left(\frac{T_w}{T_\infty}\right)^{3/2} \\ c &= \rho_\infty U_\infty^2 C^{1/4} \lambda^{1/2} \left(M_\infty^2 - 1\right)^{-1/4} \\ d &= x_0 U_\infty C^{3/4} \lambda^{-1/2} \left(M_\infty^2 - 1\right)^{-1/4} \left(\frac{T_w}{T_\infty}\right)^{2} \end{aligned} \tag{5.5}$$

where $C = \frac{\mu_w T_\infty}{\mu_\infty T_w}$ and λ is the slope of the incoming boundary layer velocity at the wall. Equation 5.3 can be reduced using Equation 5.4 and Equation 5.5 to get

$$\begin{aligned} u^* \frac{\partial u^*}{\partial x^*} + v^* \frac{\partial u^*}{\partial y} &= -\frac{\mathrm{d}p^*}{\mathrm{d}x^*} + \frac{\partial^2 u^*}{\partial {y^*}^2}, \\ \frac{\partial u^*}{\partial x^*} + \frac{\partial v^*}{\partial y^*} &= 0 \end{aligned} \tag{5.6}$$

which is a form of the incompressible boundary-layer equations. The boundary conditions are determined from the analytical solution of the upper and main decks and from wall conditions and are given as

$$\begin{aligned} u^* = v^* = 0 \quad &\text{at} \quad y^* = 0 \\ u^* \to y^* \quad &\text{as} \quad x^* \to -\infty \\ u^* - y^* \to \int_{-\infty}^{x^*} p^*(t)\, \mathrm{d}t \quad &\text{as} \quad y^* \to \infty \end{aligned} \tag{5.7}$$

At this point the solution of the boundary layer near the disturbance can be solved by numerically solving the lower deck equations with the given boundary conditions.

5.1.3 Double-Wedge Separation Length Scaling

Davis and Sturtevant combined the base flow model with triple-deck theory to form the separation length scaling with the goal of being able to account for "real-gas" effects. The scaling was built by substituting the lower deck normalized terms from

Equation 5.4 into Equation 5.2. The constants from Equation 5.5 are then used to simplify further obtaining the final scaling relation

$$\frac{L_{\text{sep}}}{x_1} \propto \frac{\Lambda_1}{\gamma_1^{3/2} M_1^3} \left(\frac{p_3 - p_2}{p_1} \right)^{3/2} \tag{5.8}$$

where

$$\Lambda = \left(\frac{\mu}{\mu^*} \right) \left(\frac{T^*}{T_e} \right) \left(\frac{T_w}{T_e} \right)^{1/2} \tag{5.9}$$

where T^* is the reference temperature as given previously by Equation 4.11. The λ term incorporates effects due to the temperature gradient within the boundary layer and viscosity changes.

These two relations are used to scale the separation length after experiments have been completed. This is completed by first measuring the separation length (L_{sep}) and the location of the separation (x_1) and reattachment points. The other parameters used for the scaling are determined through computational and theoretical means. The stagnation streamline within the separated boundary layer is assumed to form an impenetrable boundary forming an intermediate wedge between the fore and aft body. Using this assumption Davis performed inviscid triple-wedge simulations using the calculated inflow conditions for a selection of their experiments. From the simulation the values for the other parameters, e.g. p_1 and M_1, were extracted. It is important to note that this scaling has no predictive capability due to the fact that the separation length is needed first so that the inviscid triple-wedge simulations can be completed to find the other required parameters.

5.1.4 Double-Cone Scaling

The scaling developed by Davis and Sturtevant was created specifically using an assumption of a two-dimensional flowfield with the triple deck theory. While planer geometries allow for simplified theoretical analysis compared to three-dimensional bodies, they require special treatment to ensure good experimental results. The

double-cone is a related geometry which alleviates some of the experimental issues such as finite span effects and flow spillage. Conical geometries introduce complications in theoretical analysis due to the non-constant flowfield behind an oblique shock as discussed in the previous chapters. The effect of the three-dimensional nature of the flowfield on the underlying triple-deck theory must be considered in order to have confidence in the application of the scaling.

Triple-deck theory applied to axisymmetric bodies has been the focus of numerous studies. The axisymmetric triple-deck analysis starts with the axisymmetric Navier-Stokes equations. Scaling arguments are used to reduce the equations in similar manner to the two-dimensional version. The inherent three-dimensionality of the axisymmetric flow field prevents them from being reduced as fully as the two-dimensional version. The object's radius remains in the equations and becomes an important parameter that must be considered before proceeding further.

Three possible solutions for the triple-deck theory are determined based on the relation between the radius of the object and the perturbation parameter, ϵ. Here we follow the explanation of the three solutions by Huang and Inger [25], however, similar analyses are made in the other studies. The perturbation parameter for axisymmetric bodies is again defined as $\epsilon = Re_{x^*}^{-1/8}$. We first consider the relationship between the perturbation parameter and the normalized radius of the cylindrical body to be $r/L = O(\epsilon^{\beta})$ where L is the distance from the front of the body to the interaction and β is to be determined. This links the state of the boundary layer through the Reynolds number to the radius of the body at the disturbance. The three general cases can then be defined by considering the value of β. When $\beta < 3$ the radius of the body is sufficiently large such that the equations reduce to the two-dimensional equations. For this condition only the incoming boundary layer profile is affected by the three-dimensionality and can be accounted for easily. When $\beta = 3$ the upper deck is affected by the three-dimensionality while the lower and main decks collapse to the two-dimensional versions. The upper deck in this case is governed by the axisymmetric wave equation in supersonic flow [24]. When $\beta > 3$ the main deck may also be affected by curvature and the full axisymmetric equations should be

used. The limit for cases are found through asymptotic analysis of the continuity and momentum equations for all three decks.

The value of beta for the current work is calculated for the HET and T5 results and shown in Table 5.1. For all conditions in both the HET and T5 the value of $\beta << 3$. Thus, the axisymmetric triple deck theory reduces to the two-dimensional triple deck theory for all three decks. The only change comes through transforming the boundary layer profile at the wall from a cone to a flat plate through the Lees-Illingworth transformation [72]. This results in an additional $\sqrt{3}$ factor to the value of $U_0'(0)$ such that,

$$U_0'(0) = 0.332\sqrt{3}\frac{u_e\mu^*\rho^*}{x_1\mu_w\rho_w}\sqrt{\frac{1}{C^*}} \tag{5.10}$$

As the scaling factor in Equation 5.10 is a constant it may be dropped as was done previously for the double-wedge scaling. Thus for $\beta < 3$ the separation scaling argument developed by Davis and Sturtevant based on the triple deck theory should hold for the double-cone geometry at these conditions.

Table 5.1: Values of axisymmetric asymptotic triple-deck parameters to determine flow regime.

Facility	Condition	Gas	Re_{x^*}	ϵ	β
HET	M78	Air	23 608	0.284	0.684
T5	H8-Re2	N2	176 348	0.221	0.570
T5	H8-Re2	Air	175 103	0.221	0.571
T5	H8-Re2	CO2	274 508	0.209	0.550
T5	H8-Re6	N2	587 036	0.190	0.519
T5	H8-Re6	Air	543 573	0.192	0.522

It is straightforward to show that $\beta < 3$ for any sufficiently high Reynolds number for a cone geometry. For an axisymmetric body the terms that appear for the triple deck scaling are determined by the body radius and Reynolds number. As discussed previously, axisymmetric terms become important for $r/L >= O(\epsilon^\beta), \beta = 3$ where $\epsilon = Re^{-1/8}$. Isolating β reveals the following relation for a general axisymmetric body,

$$\beta = -8\frac{\ln(r/x^*)}{\ln(Re_{x^*})} \tag{5.11}$$

where r is body radius, x^* is the distance to the interaction, and Re_{x^*} is the Reynolds number at the interaction. For example, for flow over a cylindrical body with constant radius there will be location where x^* grows large enough such that $\beta = 3$. For a cone we can transform r into a function of the surface distance,

$$r = x^* \sin(\theta) \tag{5.12}$$

which when substituted into Equation 5.11 yields,

$$\beta \propto -\frac{\ln(\sin(\theta))}{\ln(Re_x x^*)} \tag{5.13}$$

after dropping the constant factor of eight and after assuming a constant unit Reynolds number. By recognizing that $0 < \sin(\theta) < 1$, the numerator is bounded to values less than zero. The means that for a cone the value of beta has the following relation,

$$\beta \propto \frac{1}{\ln(Re_x x^*)} \tag{5.14}$$

Thus, for a sufficiently large Re_x, as x^* grows the value of β decreases and thus the two-dimensional triple deck scaling law is applicable anywhere along the body. Note that this analysis only holds when $x^* > r$ which should be true for practical applications of this scaling law.

5.2 Experimental Separation Scaling Results

5.2.1 Double-Wedge

The experimental scaling results for the double-wedge are presented here. The purpose of these double-wedge experiments was to ensure consistency with the previous double-wedge work completed in T5 by Davis and Sturtevant. Experiments are made using air and nitrogen as the test gas. However, nitrogen results for the double-wedge are not included in the figures below due to the flow unsteadiness observed in the

shadowgraph images as discussed in section 4.2. Single-frame and high-speed schlieren images are obtained and measurement of the flow separation parameters completed after steady flow was achieved. The parameters measured from the schlieren images include the distance to separation (x_1), the separation length (L_{sep}), and the separated boundary layer deflection angle (θ_{sep}). The reattachment shock angle, (θ_{re}), was also measured but not used in this analysis. These measurements are labeled for the double-wedge in Figure 5.4.

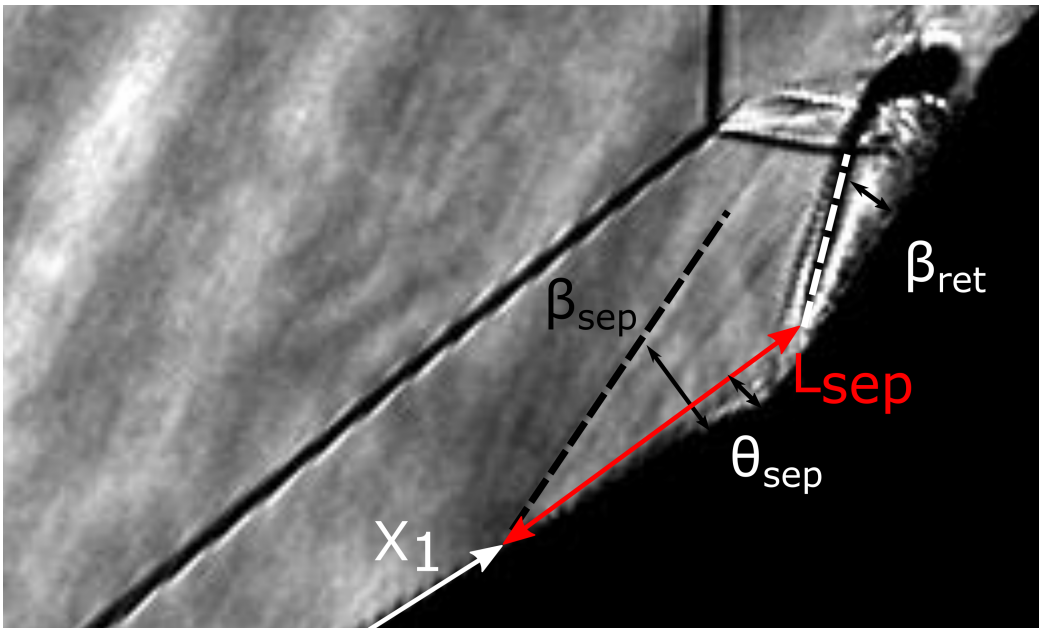

Figure 5.4: Measured separation scaling parameters labeled on shadowgraph image of double-wedge flow

The method to calculating the other parameters required for the scaling is inspired by the triple-wedge simulations. For the current work a triple wedge geometry is assumed where the stagnation streamline is replaced by a solid wall which is defined using the measured parameters, θ_{sep} and L_{sep}. A series of frozen and equilibrium oblique shock calculations are performed to determine the properties of the three regions, also labeled on Figure 5.4. The conditions in region 1 are calculated by performing a frozen post-oblique shock calculation using the freestream conditions and the wedge deflection angle. Next, the properties for region 2 are found using the frozen oblique shock calculation by assuming the flow deflects perfectly over

the separated boundary layer. A frozen post-shock flow for regions one and two is a reasonable assumption based on results from the nonequilibrium single wedge computations which showed negligible change in the species mass fractions at the boundary layer edge along the length of the front wedge. We perform one last oblique shock calculation by assuming the flow is compressed to match the aft wedge angle. The shock calculations are made using Cantera [38] and the SDToolbox [39].

The separation length scaling correlated against the pressure scaling for the double-wedge in T5 and HET is shown in Figure 5.5. The current results are shown by the filled symbols and the previous mid-enthalpy Davis and Sturtevant results are indicated by the open black circles. Their previous mid-enthalpy results span in stagnation enthalpy from 7 MJ/kg to 11 MJ/kg. The air results for both facilities are in good agreement with the previous nitrogen results. The higher normalized pressure rise for the HET results is due to the change in freestream Mach number between T5 and the HET.

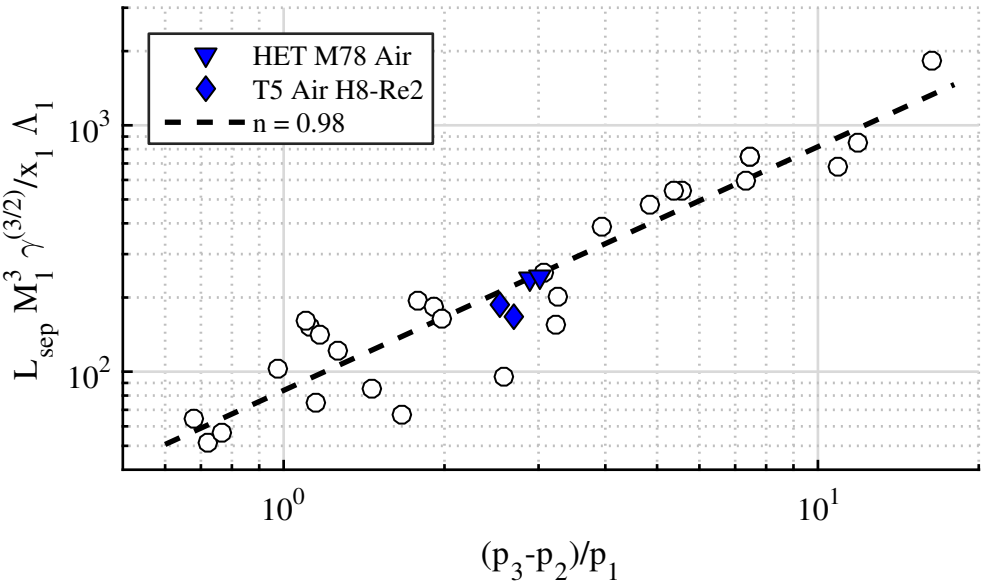

Figure 5.5: Separation length for double-wedge in T5.

The other major different between the HET and T5 run condition is the freestream Reynolds number is much higher for T5. Previous experimental results [73] have shown the separation length to be a function of the Reynolds number typically grow-

ing like $\sqrt{Re}$. Davis and Sturtevant show that the separation length to not be a function of the Reynolds number for a purely laminar interaction. The scaled separation length correlated to the Reynolds number at the separation location is shown in Figure 5.6. Again the historical mid-enthalpy data are shown by the open circles. The open squares show the historical low-enthalpy data. These data are included to show the magnitude of the decrease due to a transitional interaction found at the low-enthalpy condition. The current data show minimal dependence of the separation size against Reynolds number in agreement with the historical data as presented.

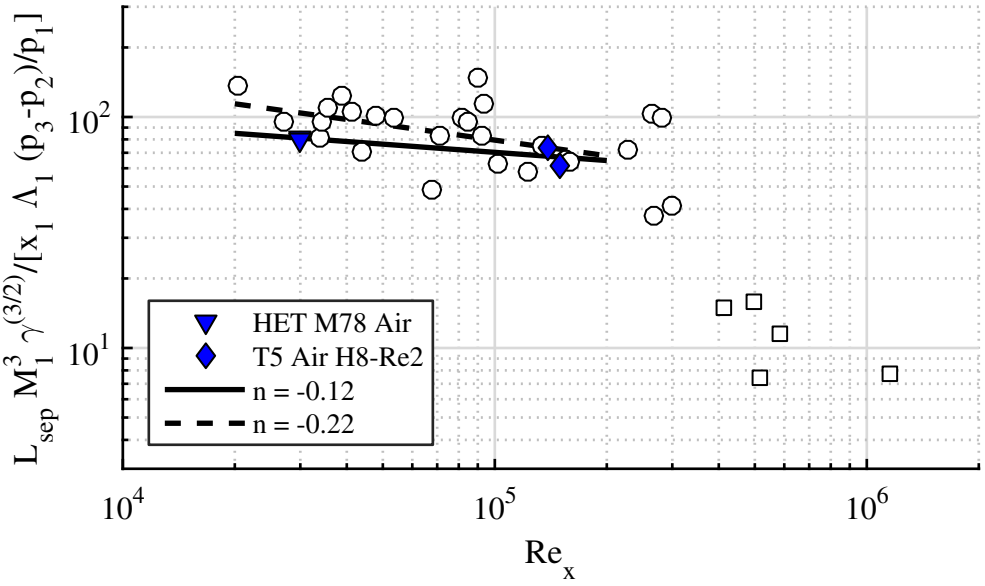

Figure 5.6: Separation length for double-wedge in T5.

It should be noted that in the double-wedge results frozen flow was assumed to exist behind the reattachment shock. This assumption may not necessarily be correct so an equilibrium shock calculation for the reattachment shock was also performed. However, the difference in the results was negligible as the impact of the reattachment shock is only seen in the reattachment pressure which did not change appreciably for the double-wedge.

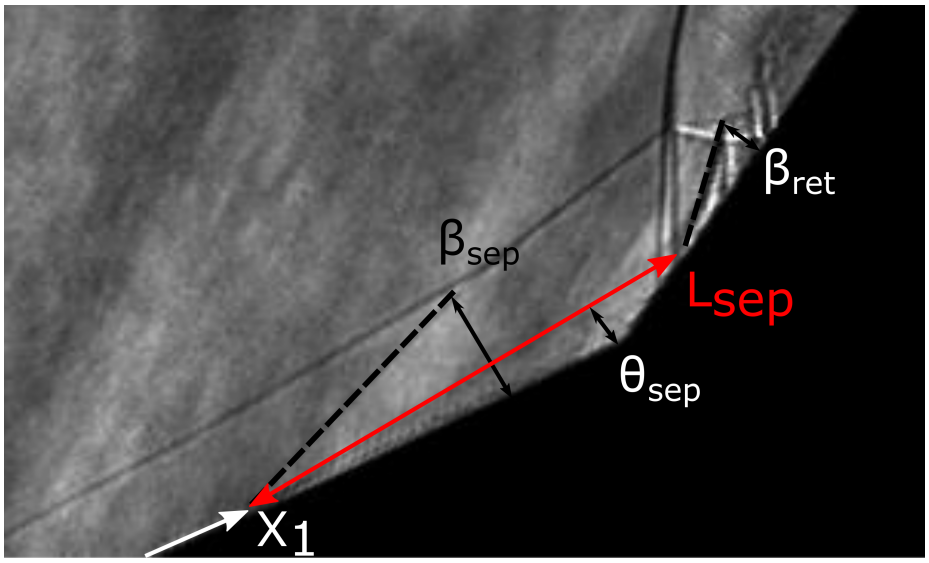

Figure 5.7: Labeled measured variables used for separation scaling for the double-cone flowfield.

5.2.2 Double-Cone Experimental Results

The separation length for the double-cone is also analyzed using the scaling developed by Davis and Sturtevant. However, due to the change in geometry certain considerations must be made regarding the choice for the parameters used in the normalization. Unlike the wedge geometry, the cone does not have constant properties behind the leading oblique shock. Instead properties are constant along rays emanating from the cone tip. The Taylor-Maccoll solution method may be used to solve for the properties behind the oblique shock and along the cone surface [74].

As with the wedge condition the measured parameters used are length to separation (x_1), separation length (L_{sep}), and the separated boundary layer deflection angle (θ_{sep}). These parameters in the context of the double-cone are shown in Figure 5.7. Again it is assumed that the stagnation streamline acts as a solid boundary to form a triple-cone geometry. The separation length and deflection angle are used to form the third cone.

Inviscid non-equilibrium triple-cone simulations are performed to determine the remaining separation parameters using the DPLR code. After each run the measured separation was used to build a triple cone grid to model the separated boundary layer.

The conditions for each region were extracted near the wall after the simulation had converged. These simulations were performed as the standard shock calculations cannot be used to calculate the cone surface properties due to the non-constant properties behind a conical shock. The Taylor-Maccoll solution could be used instead but uses a perfect gas formulation which may not be appropriate for this flowfield.

The double-cone separation length results shown in Figure 5.8 include experimental results from T5 and HET experiments. Previous HET results for the double-cone are shown by the open blue and red circles. New experiments were not completed with the double-cone in the HET, rather these results are a reinterpretation of previous experimental results collected by Swantek [17]. The historical T5 data for the mid-enthalpy range are shown by the open black circles. Note that while these data were collected using a planar geometry, the results for the double-cone for the current conditions should be in agreement due to the triple deck analysis in Section 5.1.4.

The current results are separated into two groups corresponding to the two different double-cone flap deflection angles due to the difference in the reattachment pressure. Within each group the data are spread out across a range of normalized pressure rises due to the difference in Mach number for each gas. The fit shown is the slope of the data as plotted on the log-log graph and thus shows the power dependence on the x-axis variable. The fit includes the experiments completed in T5. Additionally, the H8-Re6 nitrogen data was excluded as no corresponding experiments were completed with the 25-48 cone as were done for the other four conditions. The fit shown shows that for a double-cone geometry there is a power-law fit with a coefficient of 0.96 of the separation length by the normalized reattachment shock pressure difference. This shows there is nearly a linear pressure dependence which is in good agreement with the historical double-wedge data.

The H8-Re2 T5 data show the separation length is a function of the Reynolds number to the -0.31 power. In making this fit we exclude the H8-Re6 data from the fit due to a probable transitional boundary layer at reattachment. The behavior of the boundary layer at reattachment is determined through comparing the heat flux with the laminar and turbulent theoretical heat flux levels (see Appendix B

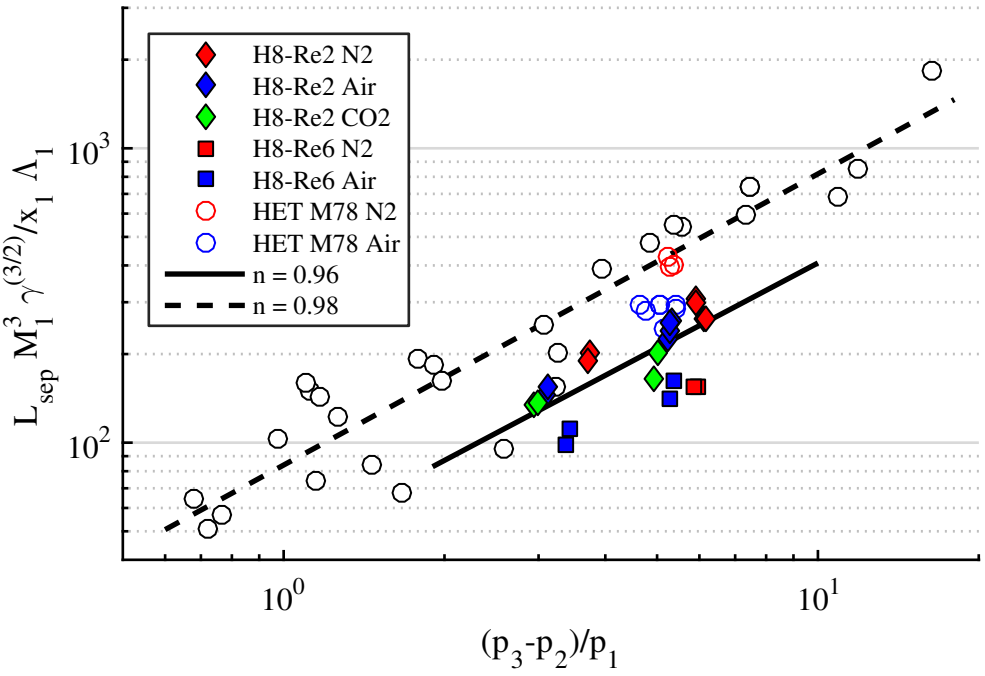

Figure 5.8: Scaled separation length versus normalized pressure rise for the double-cone in T5 and the HET. The open black circles indicate mid-enthalpy results from Davis and Sturtevant [4]. The value listed for the lines are the coefficients for a power law fit. The fit for the current data excludes the HET and the T5 H8-Re6 nitrogen data.

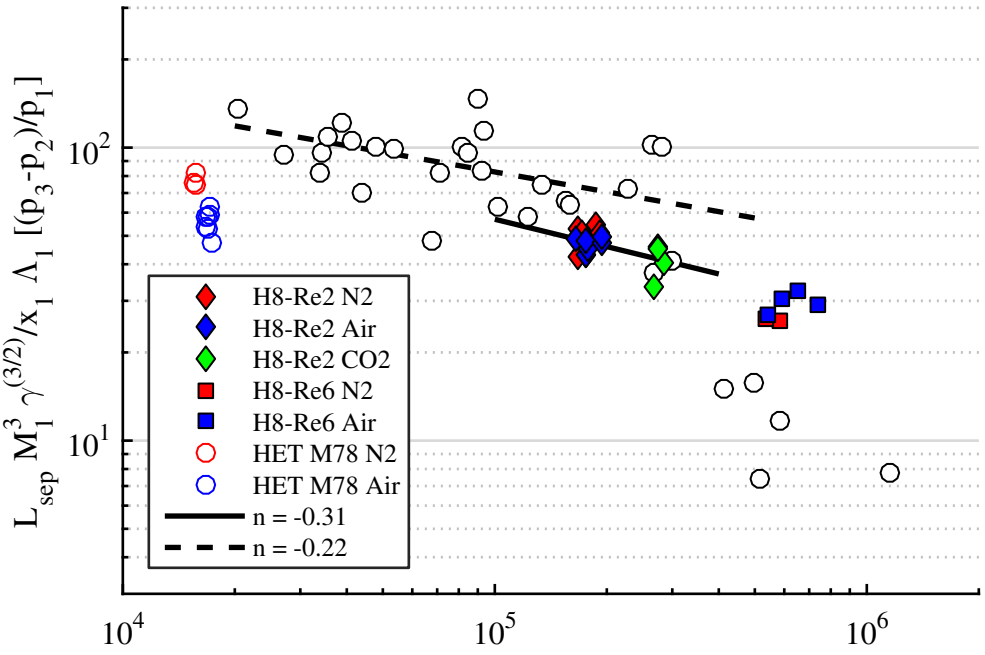

Figure 5.9: Scaled separation length against Reynolds number for the double-cone in T5 and the HET. The black open symbols indicate the low-enthalpy (triangles) and mid-enthalpy (circles) results from Davis and Sturtevant [4]. The value listed for the lines are the coefficients for a power law fit. The fit for the current data only includes the T5 H8-Re2 data.

for mean heat flux results). If the heat flux is higher than 25% of the difference between the laminar and turbulent heat flux correlations we consider the this to be a transitional interaction. We know that transitional shear layers exhibit reduced separation lengths compared to laminar interactions. The carbon dioxide heat flux points to a possibly transitional reattached boundary layer although the shadowgraph images look relatively "clean". If we include the HET air results and exclude the 25-55 double-cone carbon dioxide results we get a scaling in which the separation length is not a function of Reynolds number. This is consistent with the experimental results of Davis and Sturtevant but not consistent with other experimental results from other studies which show separation length growing with increasing Reynolds number [73].

Transition of a compressible shear layer has been studied for supersonic conditions by Birch and Keys [75] and by King, Creel, and Bushnell [76]. Their results show that for a separated shear layer the transition Reynolds number increases with increasing Mach number. Birch and Keys show the transition Reynolds number within the range of $3.0 \times 10^4 < Re_T < 6.5 \times 10^4$ at $M = 2.3$ and King et al. show a transition Reynolds number, $3.6 \times 10^5 < Re_T < 5.3 \times 10^5$ at $M = 3.5$. We can examine the present experiments in the compressible shear layer frame of reference where the length of the shear layer is given as L_{sep} and the properties for calculating the Reynolds number are obtained from region 2 of the inviscid triple cone simulations. The scaled separation length plotted against Re_{Lsep} is shown in Figure 5.10. The Mach number in the current work is between 2.85 and 3.1. Knowing this we expect a shear layer transition Reynolds number in between the historical results. The figure show a delineation between the laminar and transitional results at $Re_{Lsep} = 10^5$ which is consistent with the historical results. In the case of air and nitrogen a clear separation is seen between high and low Reynolds number conditions. However, the carbon dioxide results show possible transitional behavior for the 25-55 double-cone model but not the 25-48 double-cone. This helps to explain Figure 5.8 where the higher pressure difference carbon dioxide results show a deviation from the fit.

The current results highlight the need to be careful when interpreting experimental results of non-planer geometries. Preview experiments with the double-cone in the

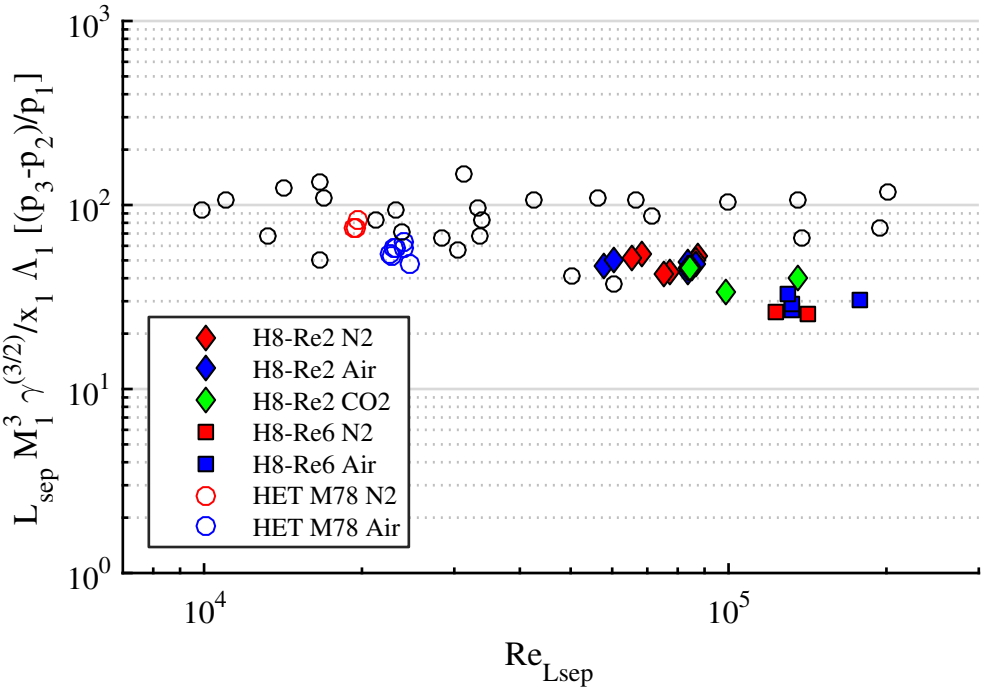

Figure 5.10: Scaled separation length plotted against separated shear layer Reynolds number. The shear layer Reynolds number is based on the properties of region 2 calculated by the inviscid triple cone simulation and the length of the separation, L_{sep}.

HET inferred a different functional dependence of the pressure on the scaled separation length [17]. In double-cone images that contain a bow shock a nearly vertical line can been seen emanating from the triple point, an example of which is shown in Figure 5.11a. This is not a physical wave but rather is an out-of-plane artifact from using a line-of-sight image technique with an axisymmetric flowfield. The artifact is from the bow shock as it is revolved around the model which results from the strong density gradient in the streamwise direction. This artifact is only observable since the termination of the normal shock is not located at the axis of symmetry and is not observed in other axisymmetric flows, e.g. spheres or blunted cones. Due to this imaging artifact, incorrect measurements of the separation length and the reattachment shock angle were made. In the previous results it was assumed that the vertical line was the reattachment shock and the separation was measured as if it terminated at the vertical line. This caused the separation length to be measured shorter than

it actually was. Additionally, due to the mistake in the reattachment shock angle measurement the reattachment pressure was incorrectly calculated.

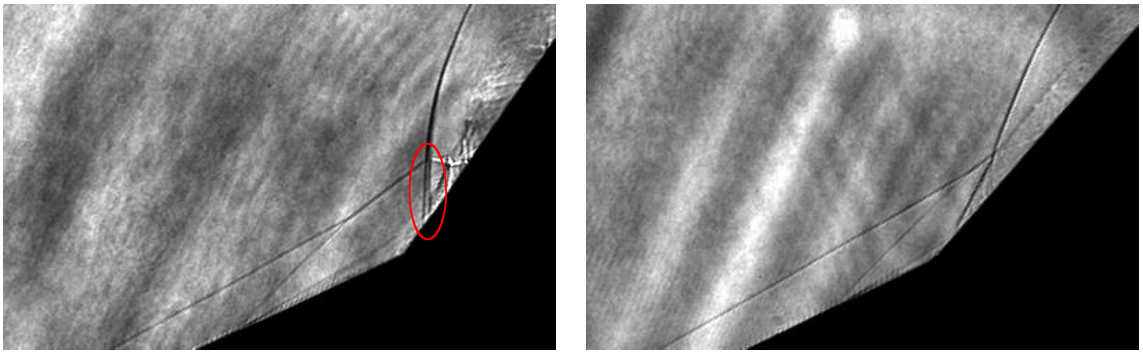

(a) Artifact present (b) No artifact present

Figure 5.11: Two shadowgraph images highlighting the artifact present with the double-cone geometry when the bow shock is perpendicular to the axis of revolution and terminates away from the body. In the left image the out-of-plane artifact is circled in red. No out of plane artifact is observed in the right image as the out-of-plane density gradient in the streamwise direction is noticeably weaker due to the lack of a revolved normal shock.

In summary we find that the double-wedge separation scaling for the HET and T5 are in agreement with historical results giving confidence that the methods used are correct. The separation scaling was applied to the double cone results and correlation of the pressure rise across the reattachment was found in agreement with the double-wedge results. The test gas composition is seen to have only minor effects on the scaling. The freestream Mach number is the primary cause of the differences that are observed between the various gases. The increase in Mach number between air and nitrogen has a direct impact through the separation scaling and has a secondary effect of increasing the pressure rise for a given flap deflection angle. We also show that the separation length drops for the high Reynolds number cases are mostly likely due to a transitional separated boundary layer.

CHAPTER 6

CONCLUSION

In this work hypervelocity flow over large deflection angle bodies is investigated experimentally. The shock boundary-layer interaction that forms is sensitive to thermal and chemical nonequilibrium. High-speed shadowgraph and surface heat flux measurements have been obtained for three model geometries in two different facilities over a range of freestream conditions and gas compositions. The run conditions for the T5 experiments were selected to complement the capabilities of the HET. Double-wedge experiments in T5 were run utilizing the same model used in previous HET studies. Two new double-cone models were designed and instrumented with fast-response thermocouples to study boundary-layer separation over an axisymmetric body and the effects due to a varying flap angle.

A finite startup time is observed in T5 and the HET through high-speed shadowgraph and heat flux data. The startup process for each facility is different and must be accounted for in order to be accurately replicated by simulations. In T5 the nozzle reservoir pressure experiences a finite rise time to a steady stagnation value. This rise time must be taken into consideration when defining a flow startup time. No transient shock structures are observed with the double-cone model in T5 after the stagnation pressure within the nozzle reaches a constant level. Any large scale fluctuation in the heat flux was found to be directly correlated to flow structures seen in the high-speed images. Steady flow is also observed with the double-wedge for an air test gas in T5. Good correlation of the scaled heat flux for the laminar region of the double-wedge was found to exist between the HET and T5 experiments. However, the boundary-layer separation with a nitrogen test gas was seen to be unsteady. It is currently unclear why this is the case as previous studies with the same geometry,

flow conditions, and aspect ratio have observed steady flow.

Type V and type VI shock interactions were observed with the 25-55 and 25-48 double-cone respectively. Shock polar diagrams of the type VI shock interaction were used to accurately describe the flow around the triple point. The shock polar diagrams were used to describe qualitatively the type V interaction by making several major assumptions regarding the post conical shock properties. Reasonable agreement of the shock polar diagram with the inviscid triple cone simulations was found despite the assumptions used.

The measured heat flux for the double-cone laminar boundary layer was found to be in agreement with analytical predictions and viscous single-cone simulations. Peak heating was measured for the double-cone for both models. With the 25-48 double-cone heating on the aft body was well predicted by the laminar correlations for air and nitrogen test gas. Peak heating was found to be slightly higher for the nitrogen than air. However, when the heat flux levels are normalized by the post-reattachment conditions the air and nitrogen are in good correlation to each other. Augmented peak heating was measured on the aft body of the 25-55 double-cone due to the post-reattachment impinging shock of the type V interaction. Higher heat flux was measured with the nitrogen test gas. However, transient heat flux traces show that the heating is highly localized to the region around the impinging shock. Very high heating is measured when the impinging shock passes over the thermocouples. In the air condition the impinging shock is located directly between two of the thermocouples. In the nitrogen condition the shock is located just upstream of the thermocouple leading to the high heat flux measurements. These results show that there must be a sufficiently high density of thermocouples in order to resolve the highly localized heat flux in the impinging interactions. Additionally, the impingement location is seen to be directly related to the location of the triple point which is partially determined by the bow shock standoff for the high-deflection angle double-cone model. One observable effect of the nonequilibrium is an increase in the post bow shock density ratio which has been seen to increase the stand off distance which affects the shock impingement location.

The separation length for the double-wedge was analyzed and found to match with historical results. Further analysis was not completed for the double-wedge due to the unsteadiness associated with the nitrogen results. The axisymmetric triple deck analysis showed that for the current conditions the equations simplify to the two dimensional form allowing for the previous scaling arguments to be considered without major modification. The separation length parameters were measured from the shadowgraph images. The double-cone separation length maintains its linear dependence on pressure ($n = 0.96$) as was observed previously for planar geometries. Good correlation is seen between the air and nitrogen results for the double-cone. The heat flux also is used to determine the nature of the boundary layer after reattachment on the aft cone. Transitional interactions occur for the higher Reynolds number condition and the carbon dioxide experiments at the higher flap angle. While the carbon dioxide aft heat flux is elevated from the laminar correlation for the 25-48 double-cone, the shadowgraph images and separation scaling results signal toward a laminar interaction.

Two possible directions for future research are to go to an intermediate stagnation enthalpy and to study additional flap angles. In the current work thermochemical non-equilibrium was primarily confined to the post-bow shock region. At increased enthalpies the differences between the gas compositions may become more apparent as the thermochemical nonequilibrium becomes important at different stagnation enthalpy levels. At the conditions considered here the pressure is dominated by the body geometry specifically through the flap angle. Changing the deflection angle will allow for a wider range of pressure conditions to be studied. While the double-cone has many benefits over the double-wedge, a major drawback is the need for new models to study any change in deflection angle compared to the double-wedge. However, finite span effects can impact the line-of-sight measurement techniques even if they are local to the edges. To gain a better understanding of the two-dimensional flowfield, planer diagnostics, e.g. focused schlieren, planar laser induced scattering ,and Rayleigh scattering, could be implemented.

APPENDIX A

T5 SHOT CONDITIONS

This appendix contains individual shot conditions completed in T5 included in this work. Table A.1 contains the measured quantities used to determine the nozzle reservoir conditions. The measured quantities in this table are the primary shock speed, U_s, the shock tube fill pressure, P_1, the nozzle reservoir pressure, P_{res}, and the primary diaphragm burst pressure, P_4. Table A.2 contains the calculated freestream conditions from the DPLR nozzle simulations.

Tables A.3–A.8 contain the surface conditions for regions 1, 2, and 3 for the double-cone shots in which the separation scaling was performed. The values in these tables are found from the DPLR inviscid triple cone simulations where the separation is assumed to act as a solid wall.

Table A.1: Measured shot conditions and calculated nozzle reservoir conditions.

Shot	Gas	Condition	U_s (m/s)	P_1 (kPa)	P_{res} (MPa)	P_4 (MPa)	T_{res} K	ρ_{res} kg/m^3	h_0 MJ/kg
2836	N2	H8-Re2	3115	45.0	17.6	42.3	6508	9.0	8.74
2837	N2	H8-Re2	3140	44.9	17.6	42.5	6557	8.9	8.86
2838	N2	H8-Re2	3010	52.0	17.6	42.6	6204	9.6	8.07
2839	N2	H8-Re2	3003	52.1	17.5	42.1	6162	9.4	7.99
2842	N2	H8-Re2	2915	45.0	17.2	37.9	6103	9.4	7.87
2843	N2	H8-Re2	2947	45.0	17.2	38.2	6159	9.2	7.99
2844	N2	H8-Re2	2969	45.0	17.2	39.3	6188	9.0	8.05
2845	N2	H8-Re2	2976	45.0	16.8	38.1	6200	9.0	8.07
2846	N2	H8-Re2	2897	45.0	16.9	38.0	6049	9.3	7.77
2847	Air	H8-Re2	2947	45.0	16.7	37.7	5058	10.6	7.84
2848	Air	H8-Re2	2984	45.0	16.9	40.0	5126	10.6	8.01
2849	Air	H8-Re2	3190	45.6	17.2	41.6	5482	9.8	8.92
2850	Air	H8-Re2	2947	45.0	18.6	38.2	5142	11.6	8.00
2851	Air	H8-Re2	3171	45.3	19.8	38.7	5573	11.1	9.07
2852	N2	H8-Re2	3199	45.1	19.8	38.1	6762	9.6	9.33
2853	N2	H8-Re2	2991	45.3	19.5	37.8	6374	10.1	8.41
2854	N2	H8-Re2	2973	45.0	19.6	38.7	6364	10.4	8.38
2855	N2	H8-Re2	3003	45.0	19.8	40.0	6445	10.5	8.55
2856	N2	H8-Re2	2995	45.0	18.9	36.1	6354	9.9	8.37
2857	Air	H8-Re2	2912	45.0	19.5	37.8	5124	12.2	7.93
2858	Air	H8-Re2	2965	45.0	19.3	40.5	5203	11.8	8.14
2859	Air	H8-Re2	2940	45.0	20.4	39.8	5206	12.5	8.12
2860	Air	H8-Re2	2940	45.0	20.5	38.5	5210	12.6	8.13
2861	Air	H8-Re6	2915	130.0	57.6	99.9	5355	35.0	7.99
2862	N2	H8-Re6	2976	130.0	61.4	111.1	6568	31.1	8.54
2863	Air	H8-Re6	2969	115.3	53.7	104.3	5475	31.7	8.31
2864	N2	H8-Re6	3079	120.0	60.4	98.3	6845	29.3	9.11
2874	CO2	H8-Re2	2793	22.1	18.8	36.3	3846	21.2	7.38
2875	CO2	H8-Re2	3048	22.0	19.3	39.7	4108	19.3	8.61
2876	N2	H8-Re2	2944	45.0	18.6	37.4	6239	9.9	8.13
2877	N2	H8-Re2	2944	45.0	19.5	39.2	6289	10.3	8.23
2878	Air	H8-Re2	2901	45.0	19.3	39.8	5097	12.2	7.87
2879	Air	H8-Re2	2933	45.0	19.9	41.8	5175	12.3	8.05
2880	CO2	H8-Re2	3052	22.0	18.9	38.9	4102	18.8	8.61
2881	CO2	H8-Re2	3029	23.0	17.9	39.4	4051	18.3	8.40
2882	Air	H8-Re6	2880	130.3	64.5	102.1	5391	39.0	8.03
2883	Air	H8-Re6	2887	129.9	58.6	105.9	5321	35.9	7.90

Table A.2: Freestream shot conditions

Shot	Gas	Condition	M_∞ –	ρ_∞ (kg/m^3)	T_∞ (K)	$T_{v,\infty}$ (K)	P_∞ (kPa)	u_∞ (m/s)	$Re_{x,\infty}$ 10^6/m
2836	N2	H8-Re2	6.6	0.0178	817	3114	4.34	3866	1.945
2837	N2	H8-Re2	6.6	0.0178	829	3128	4.40	3892	1.938
2838	N2	H8-Re2	6.7	0.0197	752	3021	4.40	3729	2.188
2839	N2	H8-Re2	6.7	0.0194	744	3022	4.30	3711	2.166
2842	N2	H8-Re2	6.7	0.0194	732	3016	4.23	3685	2.170
2843	N2	H8-Re2	6.7	0.0189	742	3032	4.17	3711	2.111
2844	N2	H8-Re2	6.7	0.0185	748	3044	4.12	3724	2.063
2845	N2	H8-Re2	6.7	0.0184	749	3048	4.09	3727	2.045
2846	N2	H8-Re2	6.7	0.0193	721	3013	4.13	3663	2.164
2847	Air	H8-Re2	5.5	0.0216	1050	1059	6.61	3601	1.823
2848	Air	H8-Re2	5.5	0.0214	1077	1085	6.74	3634	1.799
2849	Air	H8-Re2	5.4	0.0200	1207	1215	7.10	3801	1.625
2850	Air	H8-Re2	5.5	0.0235	1081	1089	7.41	3638	1.969
2851	Air	H8-Re2	5.4	0.0226	1239	1247	8.24	3836	1.823
2852	N2	H8-Re2	6.6	0.0190	881	3166	4.98	3987	2.031
2853	N2	H8-Re2	6.6	0.0205	787	3033	4.79	3805	2.253
2854	N2	H8-Re2	6.6	0.0210	785	3022	4.89	3801	2.307
2855	N2	H8-Re2	6.6	0.0211	803	3038	5.04	3837	2.308
2856	N2	H8-Re2	6.6	0.0199	783	3039	4.64	3796	2.195
2857	Air	H8-Re2	5.5	0.0248	1072	1079	7.76	3626	2.084
2858	Air	H8-Re2	5.4	0.0240	1104	1111	7.75	3666	2.002
2859	Air	H8-Re2	5.5	0.0255	1103	1110	8.20	3664	2.121
2860	Air	H8-Re2	5.4	0.0255	1105	1111	8.22	3666	2.122
2861	Air	H8-Re6	5.5	0.0725	1106	1106	23.17	3679	6.051
2862	N2	H8-Re6	6.6	0.0635	835	2713	15.73	3873	6.843
2863	Air	H8-Re6	5.4	0.0654	1161	1162	21.98	3737	5.370
2864	N2	H8-Re6	6.5	0.0586	897	2792	15.60	3989	6.205
2874	CO2	H8-Re2	4.4	0.0397	1445	1445	12.37	2906	2.133
2875	CO2	H8-Re2	4.4	0.0361	1573	1572	12.65	3088	1.935
2876	N2	H8-Re2	6.7	0.0202	759	3015	4.55	3745	2.241
2877	N2	H8-Re2	6.7	0.0210	770	3008	4.79	3767	2.318
2878	Air	H8-Re2	5.5	0.0247	1062	1069	7.65	3613	2.081
2879	Air	H8-Re2	5.5	0.0250	1092	1099	7.96	3650	2.087
2880	CO2	H8-Re2	4.4	0.0353	1566	1566	12.32	3085	1.894
2881	CO2	H8-Re2	4.4	0.0342	1536	1535	11.68	3052	1.845
2882	Air	H8-Re6	5.5	0.0809	1112	1112	26.01	3689	6.755
2883	Air	H8-Re6	5.5	0.0744	1090	1090	23.45	3661	6.247

Table A.3: Region 1 calculated shot conditions

Shot	Cond.	Gas	M_1 –	ρ_1 kg/m^3	T_1 K	$T_{v,1}$ K	p_1 kPa	u_1 m/s	$Re_{x,1}$ 10^6/m
2853	H8-Re2	N2	3.36	0.08704	2379	3017	61.59	3345	4.031
2854	H8-Re2	N2	3.36	0.08926	2368	3005	62.86	3341	4.143
2855	H8-Re2	N2	3.36	0.08958	2422	3021	64.53	3372	4.128
2856	H8-Re2	N2	3.36	0.08476	2367	3023	59.67	3337	3.931
2857	H8-Re2	Air	3.15	0.09790	2472	1749	70.54	3173	4.057
2858	H8-Re2	Air	3.15	0.09457	2532	1803	69.91	3208	3.893
2859	H8-Re2	Air	3.15	0.1002	2530	1823	73.95	3204	4.124
2860	H8-Re2	Air	3.15	0.1005	2529	1824	74.12	3208	4.141
2861	H8-Re6	Air	3.24	0.2990	2434	2245	210.5	3222	12.74
2862	H8-Re6	N2	3.35	0.2685	2488	2688	198.3	3404	12.25
2863	H8-Re6	Air	3.23	0.2690	2523	2353	196.5	3273	11.34
2864	H8-Re6	N2	3.34	0.2470	2651	27706	194.5	3505	11.07
2874	H8-Re2	CO2	3.13	0.1629	2191	2191	76.83	2547	6.585
2875	H8-Re2	CO2	3.11	0.1464	2417	2417	78.86	2706	5.785
2876	H8-Re2	N2	3.36	0.08599	2302	3000	58.85	3292	4.017
2877	H8-Re2	N2	3.36	0.08918	2331	2992	61.82	3311	4.151
2878	H8-Re2	Air	3.16	0.09763	2450	1749	69.70	3162	4.058
2879	H8-Re2	Air	3.16	0.09876	2498	1832	71.95	3194	4.089
2880	H8-Re2	CO2	3.11	0.1431	2410	2410	76.92	2704	5.660
2881	H8-Re2	CO2	3.11	0.1431	2410	2410	76.92	2704	5.660
2882	H8-Re6	Air	3.26	0.3363	2431	2314	236.4	3231	14.39
2883	H8-Re6	Air	3.24	0.3065	2423	2265	214.7	3206	13.04

Table A.4: Region 1 calculated mass fractions

Shot	$Y_{N_2,1}$	$Y_{O_2,1}$	$Y_{NO,1}$	$Y_{N,1}$	$Y_{O,1}$	$Y_{CO_2,1}$	$Y_{CO,1}$
2853	0.9979	0	0	2.080e-3	0	0	0
2854	0.998	0	0	1.989e-3	0	0	0
2855	0.9978	0	0	2.166e-3	0	0	0
2856	0.9979	0	0	2.113e-3	0	0	0
2857	0.7314	0.1795	7.643e-2	6.216e-7	1.268e-2	0	0
2858	0.7318	0.1781	7.566e-2	8.745e-7	1.444e-2	0	0
2859	0.7317	0.179	7.580e-2	8.085e-7	1.347e-2	0	0
2860	0.7317	0.179	7.576e-2	8.079e-7	1.352e-2	0	0
2861	0.7316	0.1885	7.602e-2	1.612e-7	3.841e-3	0	0
2862	0.9995	0	0	4.575e-4	0	0	0
2863	0.7322	0.1878	7.377e-2	3.000e-7	5.232e-3	0	0
2864	0.9993	0	0	6.863e-4	0	0	0
2874	0	0.09793	0	0	1.729e-3	0.7259	0.1745
2875	0	0.1214	0	0	4.631e-3	0.6534	0.2206
2876	0.9982	0	0	1.818e-3	0	0	0
2877	0.9982	0	0	1.826e-3	0	0	0
2878	0.7361	0.1797	7.661e-2	5.609e-7	1.237e-2	0	0
2879	0.7316	0.1791	7.598e-2	7.155e-7	1.331e-2	0	0
2880	0	0.1219	0	0	4.686e-3	0.6518	0.2216
2881	0	0.1219	0	0	4.686e-3	0.6518	0.2216
2882	0.7317	0.1892	7.572e-2	1.405e-7	3.390e-3	0	0
2883	0.7315	0.1887	7.632e-2	1.417e-7	3.513e-3	0	0

Table A.5: Region 2 calculated shot conditions

Shot	Cond.	Gas	M_2 –	ρ_2 kg/m^3	T_2 K	$T_{v,2}$ K	p_2 kPa	u_2 m/s	$Re_{x,2}$ 10^6/m
2853	H8-Re2	N2	3.08	0.1129	2672	3009	89.75	3252	4.666
2854	H8-Re2	N2	3.03	0.1172	2721	2994	94.83	4128	4.745
2855	H8-Re2	N2	3.05	0.1191	2752	3009	97.45	3268	4.835
2856	H8-Re2	N2	3.07	0.1115	2678	3013	88.82	3238	4.579
2857	H8-Re2	Air	2.83	0.1411	2803	2116	115.3	3036	5.112
2858	H8-Re2	Air	2.90	0.1262	2790	2080	102.8	3104	4.687
2859	H8-Re2	Air	2.92	0.1332	2773	2100	107.7	3106	4.975
2860	H8-Re2	Air	2.92	0.1324	2767	2100	106.8	3111	4.959
2861	H8-Re6	Air	3.02	0.3861	2664	2423	297.4	3135	15.00
2862	H8-Re6	N2	3.12	0.3290	2730	2688	266.6	3328	13.70
2863	H8-Re6	Air	3.04	0.3308	2722	2491	260.8	3199	12.91
2864	H8-Re6	N2	3.08	0.3124	2950	2780	273.7	3413	12.59
2874	H8-Re2	CO2	2.92	0.2207	2353	2352	111.8	2461	8.179
2875	H8-Re2	CO2	2.83	0.2146	2661	2661	127.3	2582	7.547
2876	H8-Re2	N2	3.01	0.1194	2668	2994	94.70	3174	4.820
2877	H8-Re2	N2	3.01	0.1240	2701	2986	99.55	3192	4.986
2878	H8-Re2	Air	2.83	0.1370	2808	1930	112.1	3031	4.950
2879	H8-Re2	Air	2.86	0.1367	2819	2070	112.4	3072	4.991
2880	H8-Re2	CO2	2.85	0.2109	2635	2634	123.9	2590	7.492
2881	H8-Re2	CO2	2.88	0.2043	2614	2613	119.1	2601	7.331
2882	H8-Re6	Air	3.00	0.4389	2697	2451	342.2	3136	16.90
2883	H8-Re6	Air	3.06	0.3711	2601	2360	279.0	3142	14.70

Table A.6: Region 2 calculated mass fractions

Shot	$Y_{N_2,2}$	$Y_{O_2,2}$	$Y_{NO,2}$	$Y_{N,2}$	$Y_{O,2}$	$Y_{CO_2,2}$	$Y_{CO,2}$
2853	0.9979	0	0	2.079e-3	0	0	0
2854	0.998	0	0	1.987e-3	0	0	0
2855	0.9978	0	0	2.164e-3	0	0	0
2856	0.9979	0	0	2.112e-3	0	0	0
2857	0.7315	0.1797	7.618e-2	1.818e-6	1.264e-2	0	0
2858	0.7319	0.1783	7.545e-2	1.993e-6	1.440e-2	0	0
2859	0.7318	0.1792	7.559e-2	1.763e-6	1.344e-2	0	0
2860	0.7318	0.1791	7.555e-2	1.737e-6	1.349e-2	0	0
2861	0.7316	0.1886	7.593e-2	3.504e-7	3.830e-3	0	0
2862	0.9995	0	0	4.573e-4	0	0	0
2863	0.7322	0.1879	7.465e-2	5.733e-7	5.218e-3	0	0
2864	0.9993	0	0	6.859e-4	0	0	0
2874	0	0.09792	0	0	1.729e-3	0.7259	0.1745
2875	0	0.1213	0	0	4.649e-3	0.6535	0.2205
2876	0.9982	0	0	1.818e-3	0	0	0
2877	0.9982	0	0	1.825e-3	0	0	0
2878	0.7314	0.1798	7.650e-2	1.803e-6	1.235e-2	0	0
2879	0.7317	0.1792	7.582e-2	2.003e-6	1.329e-2	0	0
2880	0	0.1218	0	0	4.698e-3	0.6519	0.2215
2881	0	0.1219	0	0	4.695e-3	0.6519	0.2215
2882	0.7318	0.1892	7.565e-2	3.436e-7	3.383e-3	0	0
2883	0.7315	0.1887	7.627e-2	2.621e-7	3.506e-3	0	0

Table A.7: Region 3 calculated shot conditions

Shot	Cond.	Gas	M_3 –	ρ_3 kg/m^3	T_3 K	$T_{v,3}$ K	p_3 kPa	u_3 m/s	$Re_{x,3}$ 10^6/m
2853	H8-Re2	N2	1.78	0.3200	4753	3206	452.4	2507	6.626
2854	H8-Re2	N2	1.52	0.3111	5198	3508	480.9	2231	5.358
2855	H8-Re2	N2	1.77	0.3325	4829	3292	477.5	2514	6.819
2856	H8-Re2	N2	1.75	0.3216	2027	3181	456.4	2475	6.532
2857	H8-Re2	Air	1.78	0.3833	4338	3247	484.8	2365	7.890
2858	H8-Re2	Air	1.75	0.3617	4503	3228	475.6	2382	7.292
2859	H8-Re2	Air	1.82	0.3932	4339	3414	498.0	2425	8.292
2860	H8-Re2	Air	1.77	0.3867	4426	3457	499.6	2384	7.904
2861	H8-Re6	Air	1.89	1.214	4023	4035	1429.	2424	27.04
2862	H8-Re6	N2	1.74	1.009	4853	3838	1454.	2471	20.27
2863	H8-Re6	Air	1.88	1.100	3955	4044	1296.	2424	24.71
2864	H8-Re6	N2	1.77	0.9465	5042	4256	1417.	2558	19.14
2874	H8-Re2	CO2	1.98	0.7216	3197	3197	497.2	1940	16.90
2875	H8-Re2	CO2	1.97	0.6569	3494	3495	514.9	2062	15.16
2876	H8-Re2	N2	2.14	0.2706	3909	3085	314.5	2736	7.081
2877	H8-Re2	N2	2.15	0.2799	3953	3043	329.0	2758	7.323
2878	H8-Re2	Air	2.15	0.3088	3647	3130	328.3	2627	8.004
2879	H8-Re2	Air	2.15	0.3116	3717	3239	337.9	2652	8.043
2880	H8-Re2	CO2	2.28	0.4903	3199	3199	350.0	2280	13.34
2881	H8-Re2	CO2	2.27	0.4894	3202	3202	349.7	2277	13.29
2882	H8-Re6	Air	2.19	1.074	3661	3621	1140.	2676	28.30
2883	H8-Re6	Air	2.17	0.9592	3663	3591	1018.	2648	25.02

Table A.8: Region 3 calculated mass fractions

Shot	$Y_{N_2,3}$	$Y_{O_2,3}$	$Y_{NO,3}$	$Y_{N,3}$	$Y_{O,3}$	$Y_{CO_2,3}$	$Y_{CO,3}$
2853	0.9979	0	0	2.078e-3	0	0	0
2854	0.998	0	0	1.987e-1	0	0	0
2855	0.9978	0	0	2.164e-3	0	0	0
2856	0.9979	0	0	2.112e-3	0	0	0
2857	0.7307	0.1784	7.784e-2	5.487e-5	1.304e-2	0	0
2858	0.7308	0.1769	7.748e-2	8.073e-5	1.475e-2	0	0
2859	0.7306	0.1772	7.795e-2	5.999e-5	1.419e-2	0	0
2860	0.7306	0.1769	7.812e-2	6.950e-5	1.435e-2	0	0
2861	0.7301	0.1743	7.926e-2	4.061e-5	1.632e-2	0	0
2862	0.9995	0	0	4.572e-4	0	0	0
2863	0.7273	0.1512	8.477e-2	8.577e-5	3.664e-2	0	0
2864	0.9993	0	0	6.866e-4	0	0	0
2874	0	0.0974	0	0	2.523e-3	0.7251	0.1749
2875	0	0.1196	0	0	8.344e-3	0.648	0.224
2876	0.9982	0	0	1.817e-3	0	0	0
2877	0.9982	0	0	1.824e-3	0	0	0
2878	0.7311	0.1793	7.695e-2	1.494e-5	1.261e-2	0	0
2879	0.7313	0.1783	7.663e-2	1.881e-5	1.372e-2	0	0
2880	0	0.1215	0	0	5.140e-3	0.6518	0.2216
2881	0	0.1214	0	0	5.241e-3	0.6517	0.2217
2882	0.7315	0.1852	7.623e-2	8.470e-6	7.075e-3	0	0
2883	0.7312	0.1855	7.678e-2	7.718e-6	6.430e-3	0	0

APPENDIX B

ADDITIONAL MEAN HEAT FLUX FIGURES

Shot-by-shot mean heat flux figures for the double-cone models are shown in this section. The symbols indicate the measured mean heat flux through the test time with the error bars indicating the standard deviation of the heat flux fluctuations. The laminar prediction, plotted as solid green line, is a theoretical prediction based on the fore cone surface properties. The solid black line indicates the extracted heat flux from the DPLR single cone simulations. The hinge location is indicated by the dot-dashed black line. On the aft section two green lines are plotted indicating a laminar and turbulent boundary layer heat flux prediction. The aft heat flux predictions are made using the conditions found for post re-attachment shock, region 3, using the inviscid triple cone simulations. An assumption is made that the boundary layer begins at the hinge.

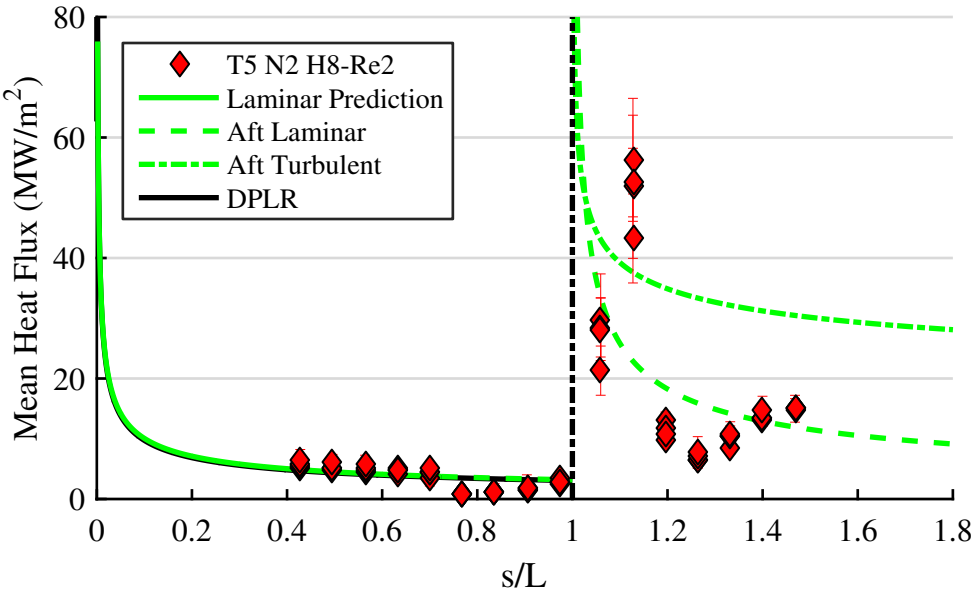

Figure B.1: Mean heat flux results for Shot 2853, H8-Re2 N2

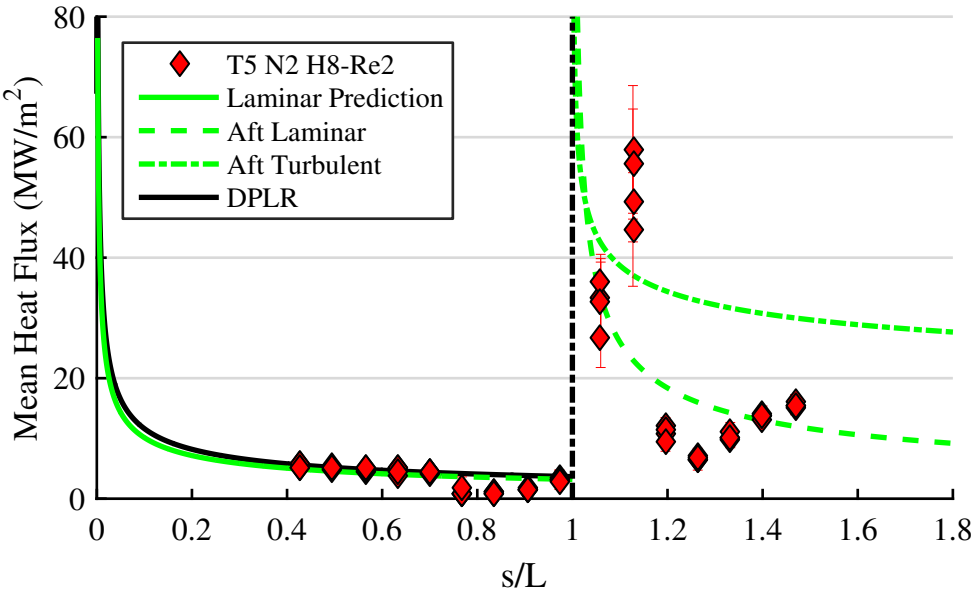

Figure B.2: Mean heat flux results for Shot 2854, H8-Re2 N2

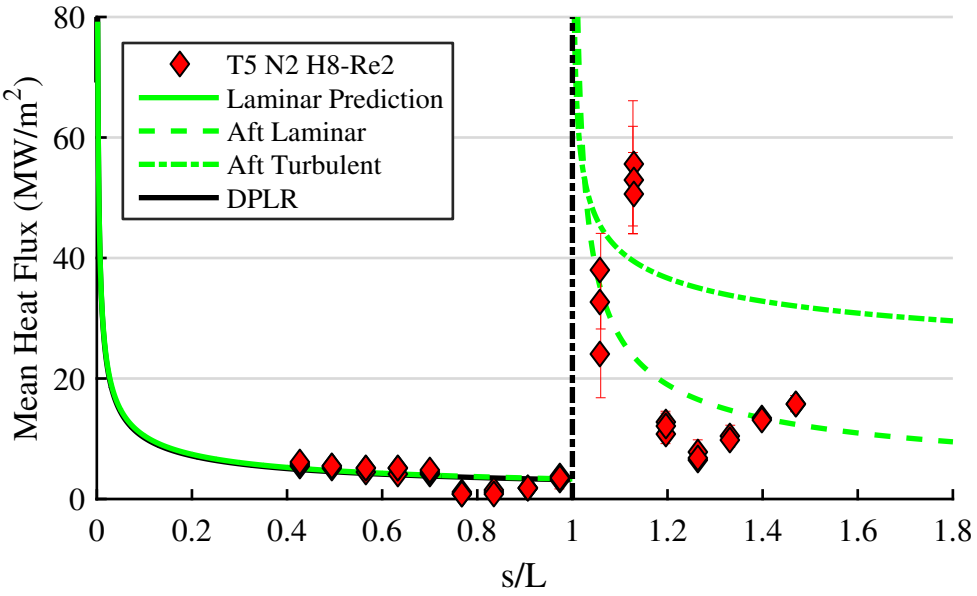

Figure B.3: Mean heat flux results for Shot 2855, H8-Re2 N2

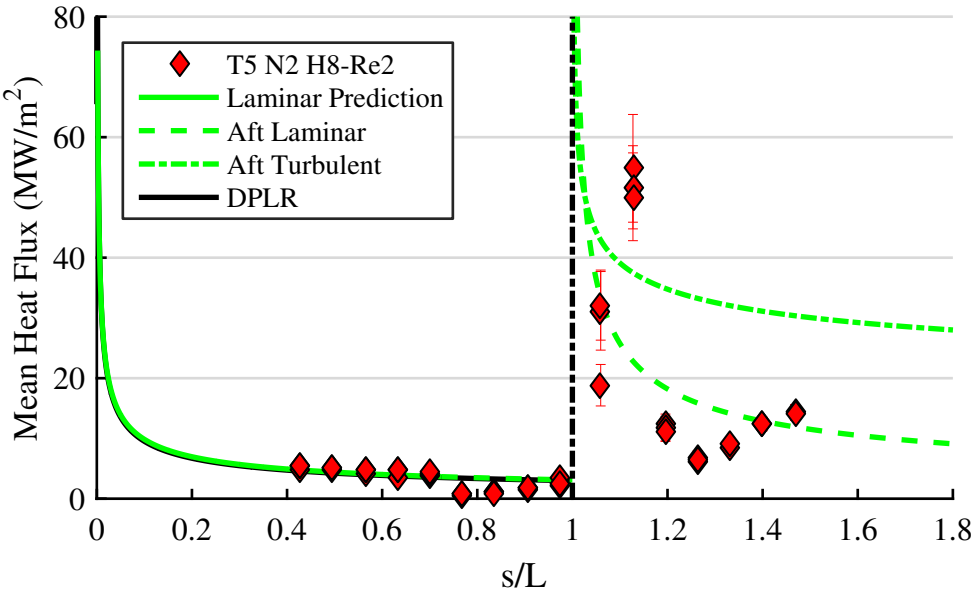

Figure B.4: Mean heat flux results for Shot 2856, H8-Re2 N2

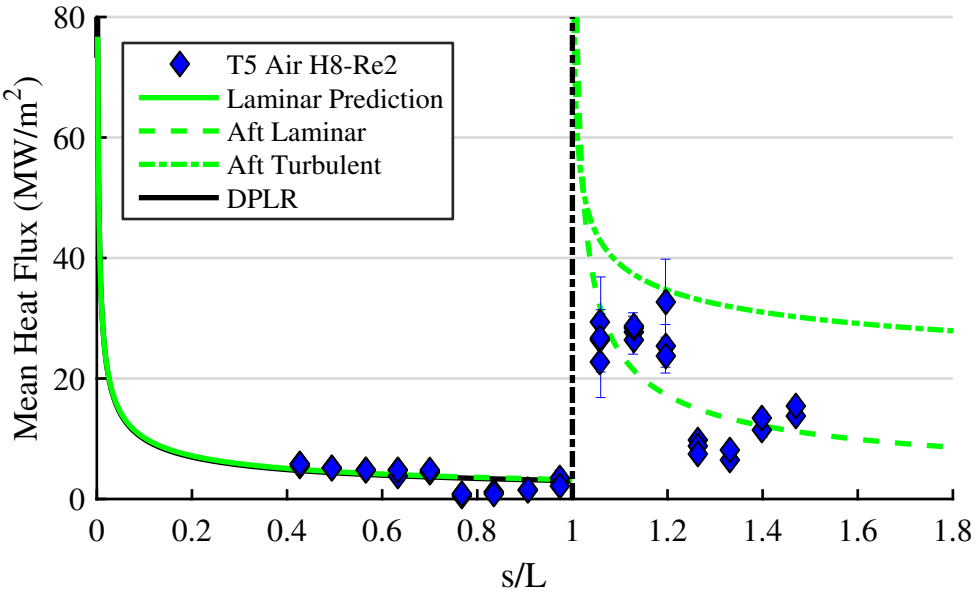

Figure B.5: Mean heat flux results for Shot 2857, H8-Re2 Air

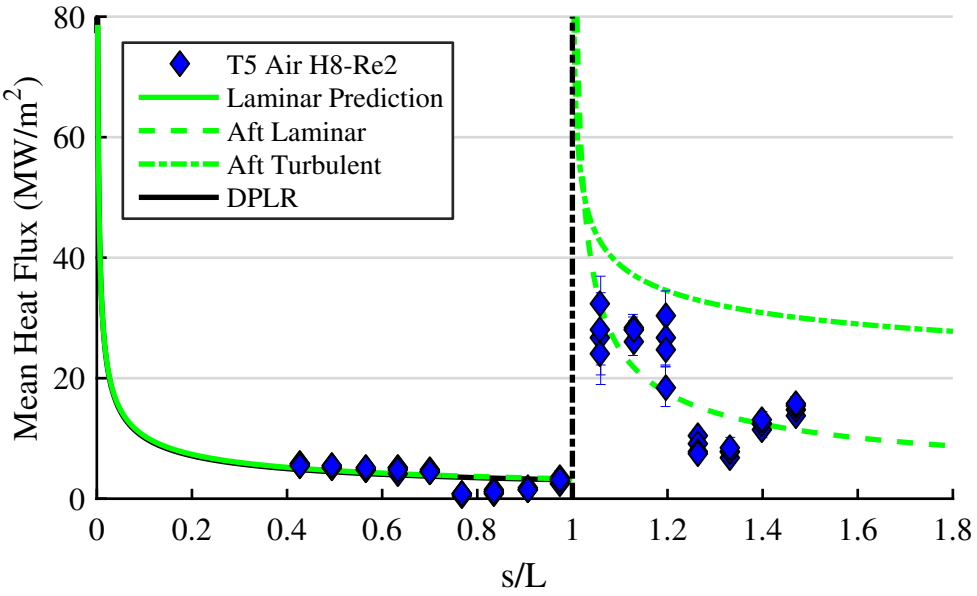

Figure B.6: Mean heat flux results for Shot 2858, H8-Re2 Air

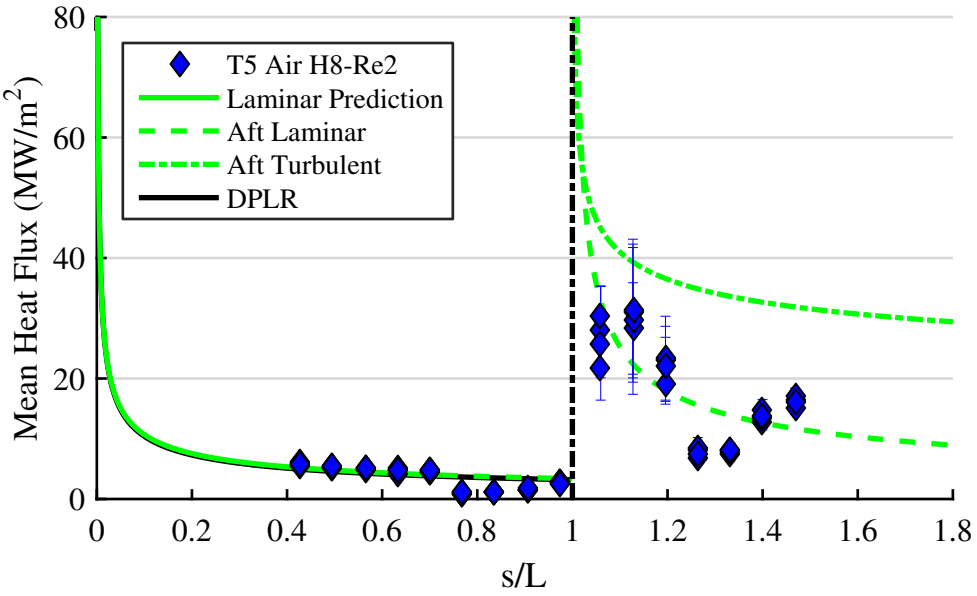

Figure B.7: Mean heat flux results for Shot 2859, H8-Re2 Air

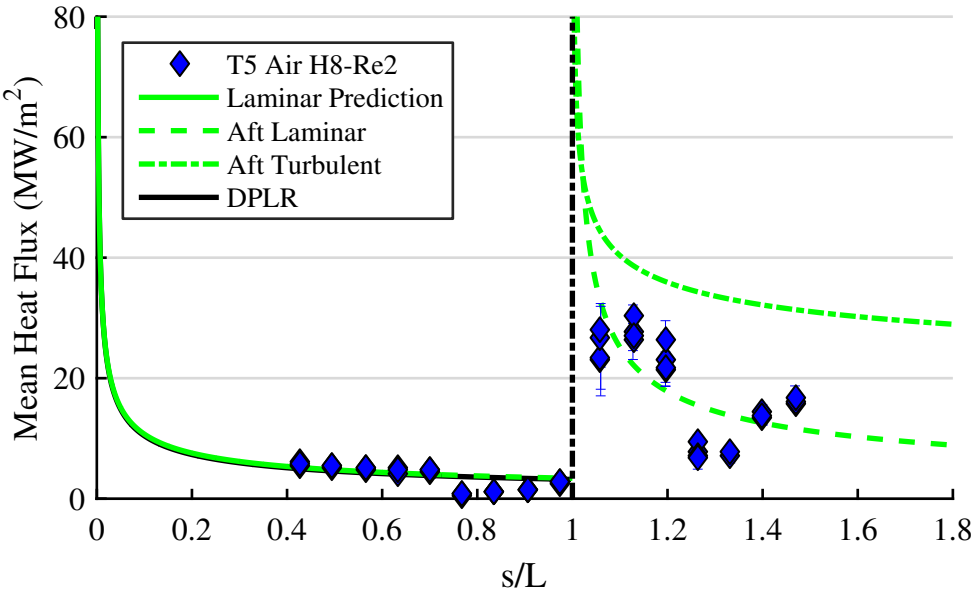

Figure B.8: Mean heat flux results for Shot 2860, H8-Re2 Air

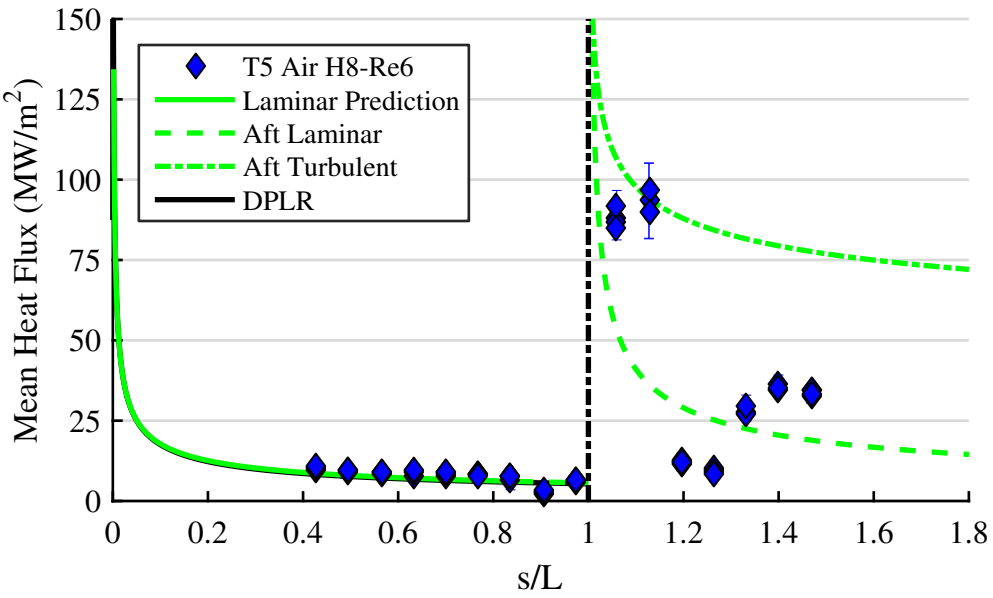

Figure B.9: Mean heat flux results for Shot 2861, H8-Re6 Air

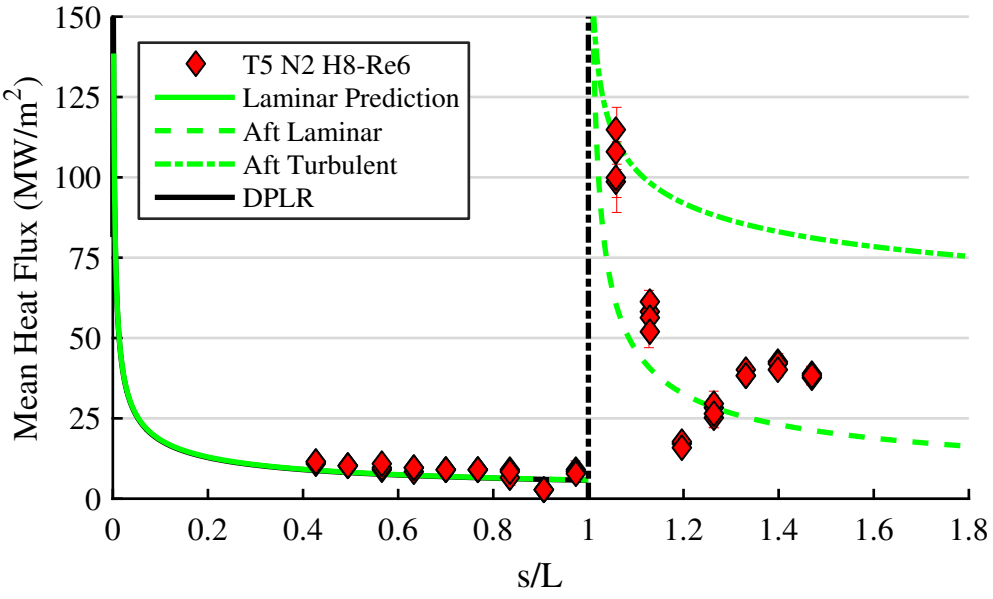

Figure B.10: Mean heat flux results for Shot 2862, H8-Re6 N2

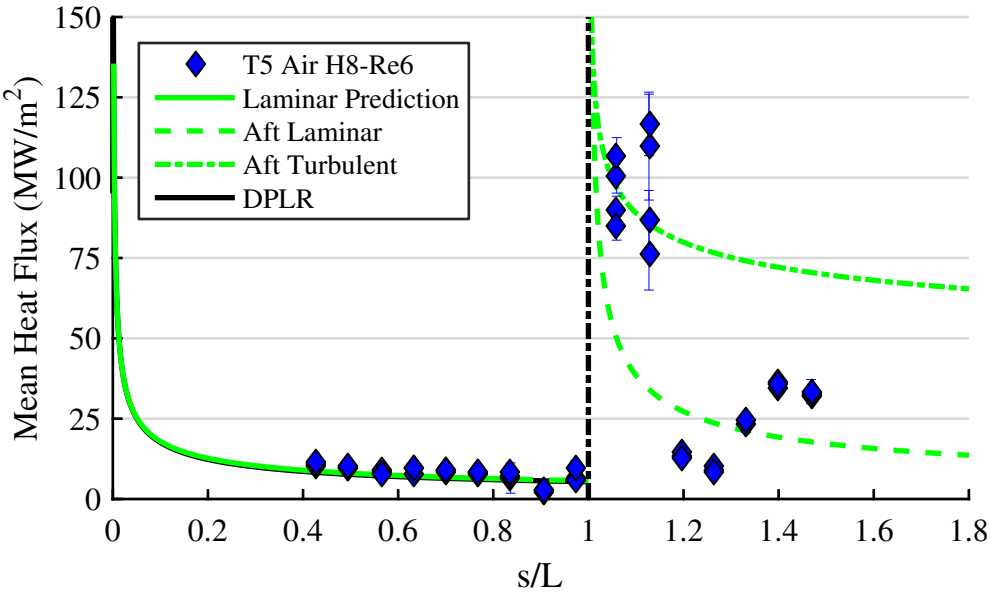

Figure B.11: Mean heat flux results for Shot 2863, H8-Re6 Air

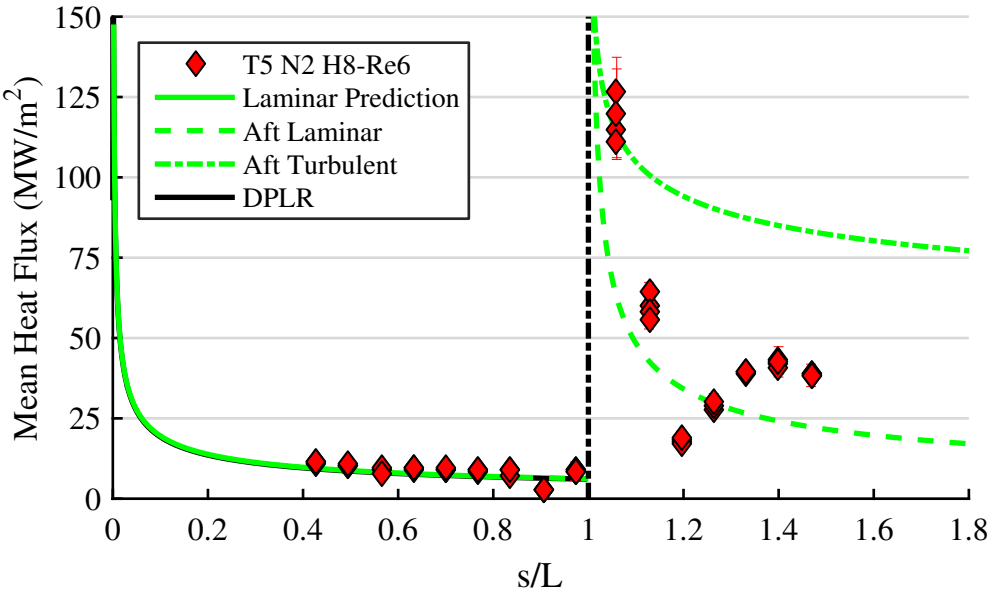

Figure B.12: Mean heat flux results for Shot 2864, H8-Re6 N2

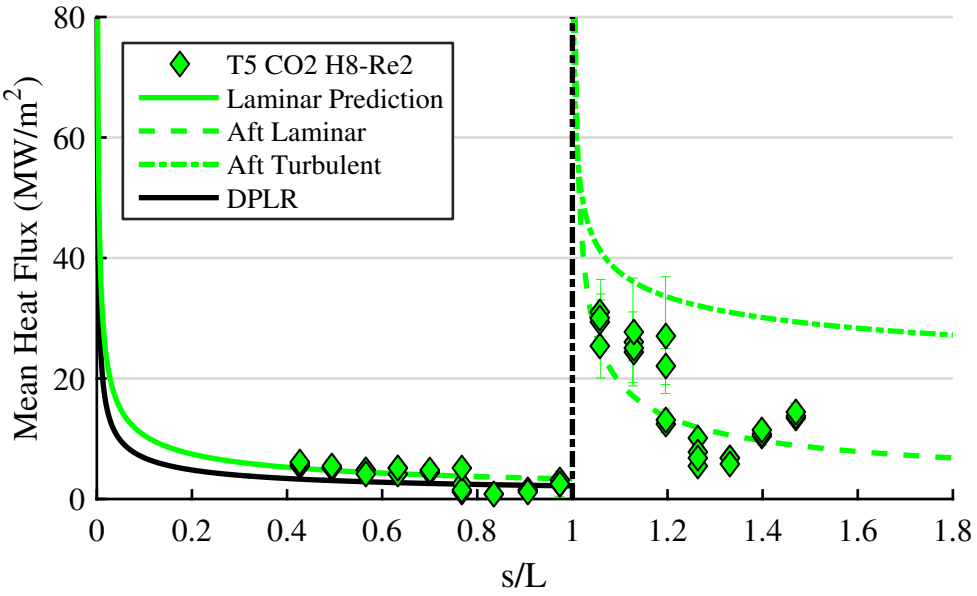

Figure B.13: Mean heat flux results for Shot 2874, H8-Re2 CO2

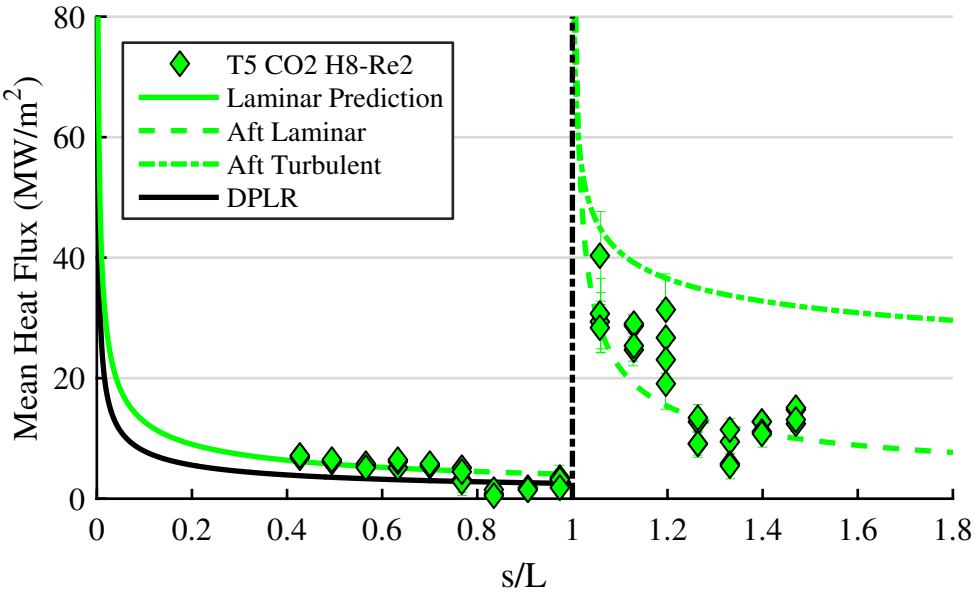

Figure B.14: Mean heat flux results for Shot 2875, H8-Re2 CO2

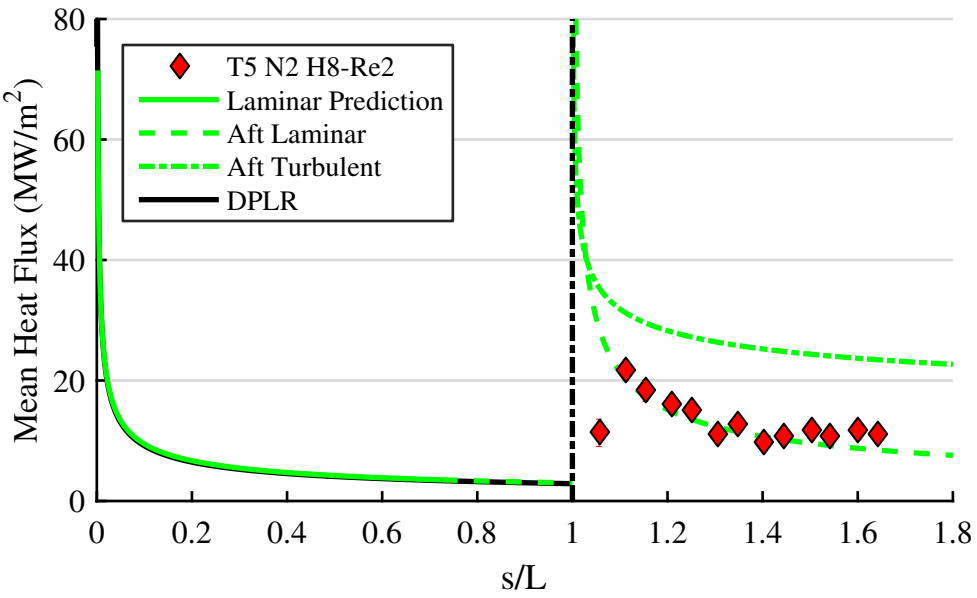

Figure B.15: Mean heat flux results for Shot 2876, H8-Re2 N2

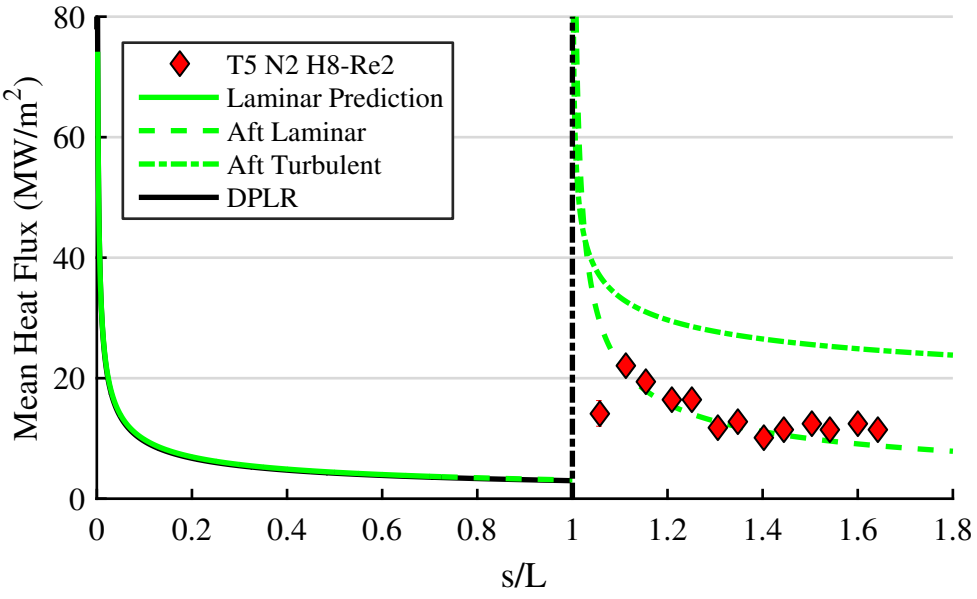

Figure B.16: Mean heat flux results for Shot 2877, H8-Re2 N2

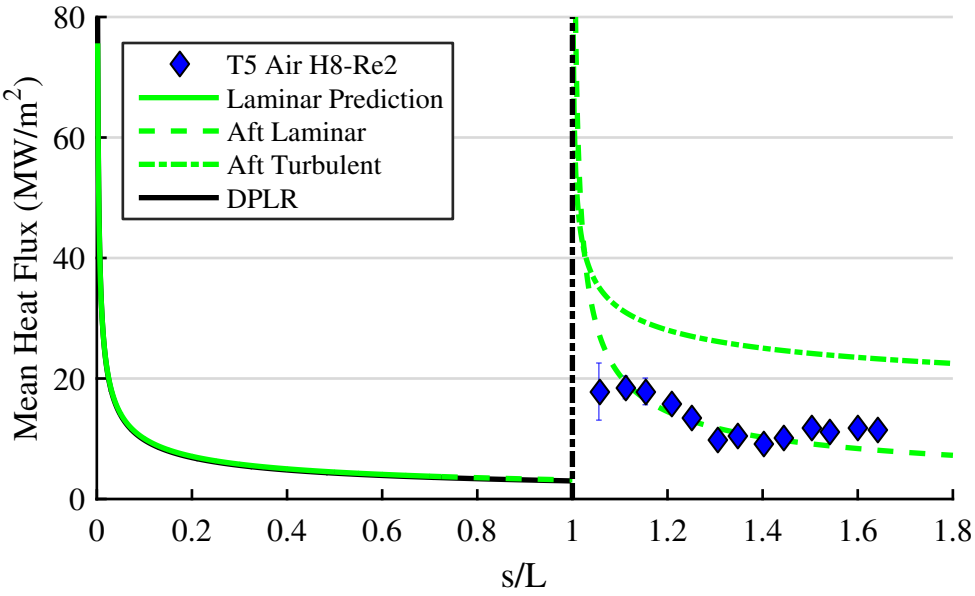

Figure B.17: Mean heat flux results for Shot 2878, H8-Re2 Air

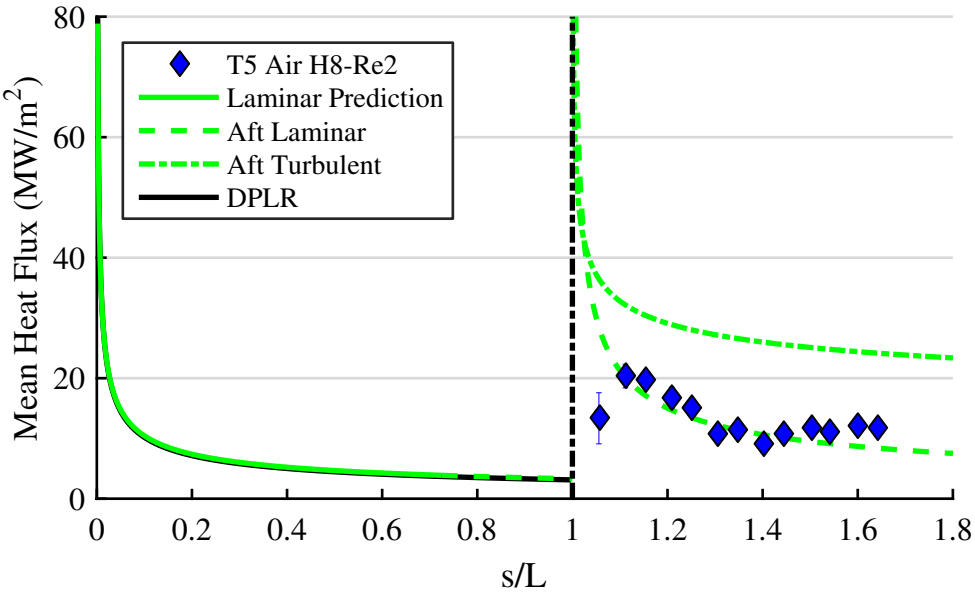

Figure B.18: Mean heat flux results for Shot 2879, H8-Re2 Air

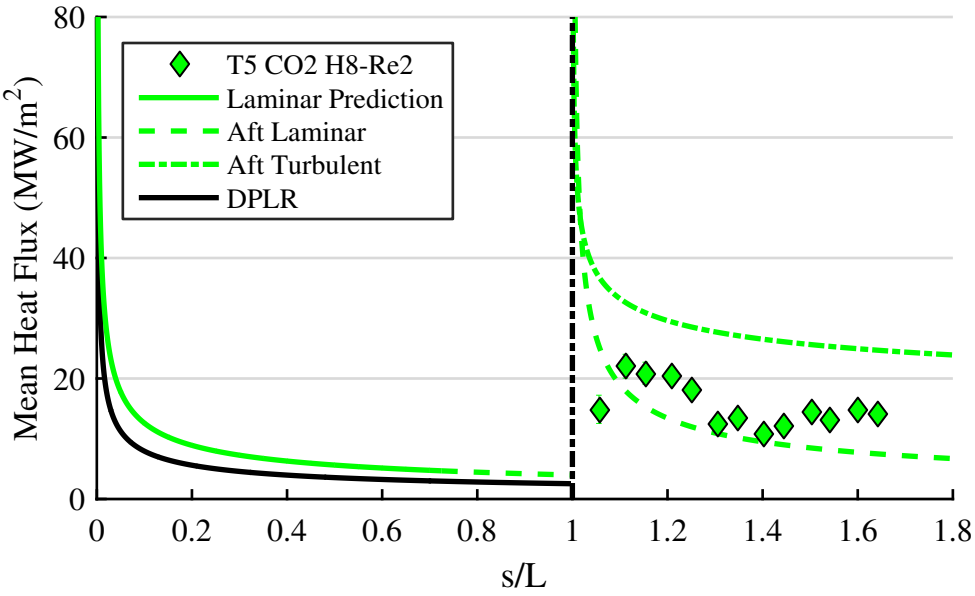

Figure B.19: Mean heat flux results for Shot 2880, H8-Re2 CO2

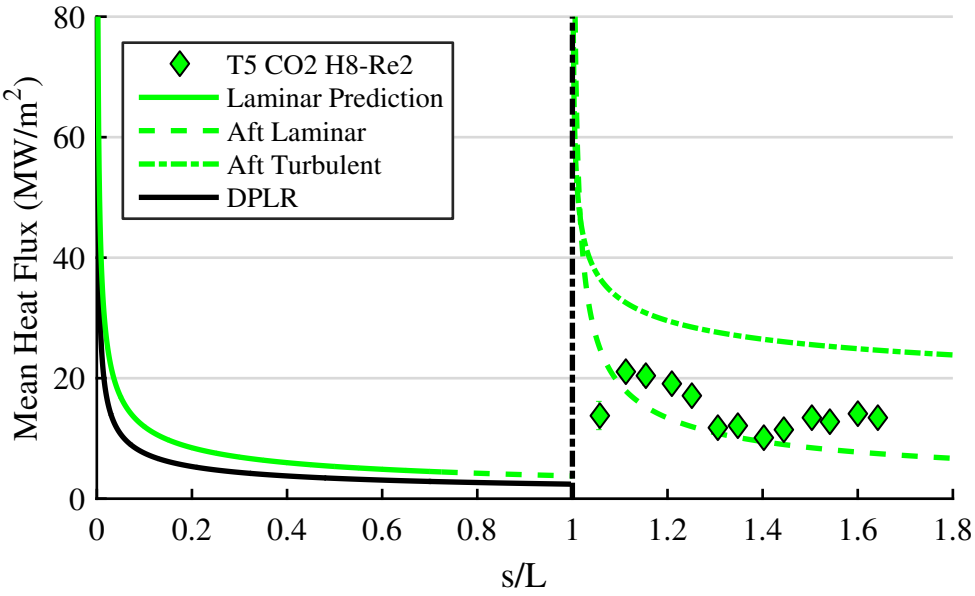

Figure B.20: Mean heat flux results for Shot 2881, H8-Re2 CO2

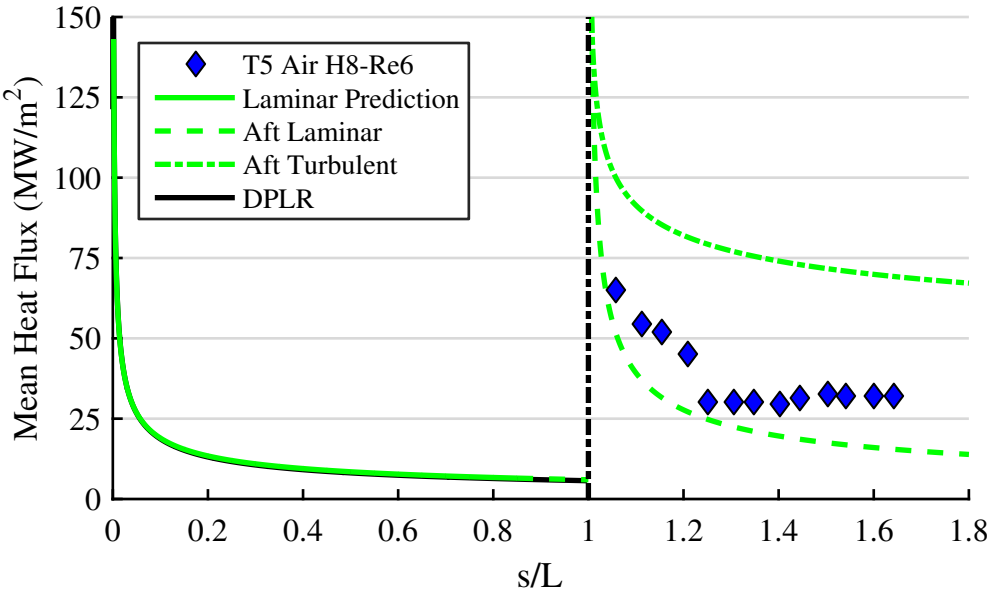

Figure B.21: Mean heat flux results for Shot 2882, H8-Re6 Air

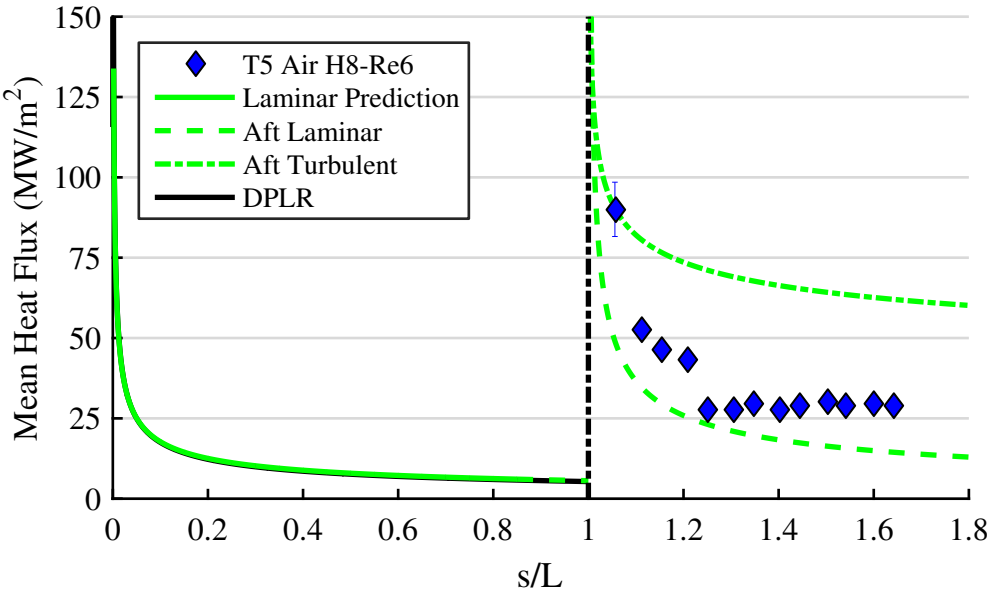

Figure B.22: Mean heat flux results for Shot 2883, H8-Re6 Air

APPENDIX C

T5 DOUBLE-CONE DRAWINGS

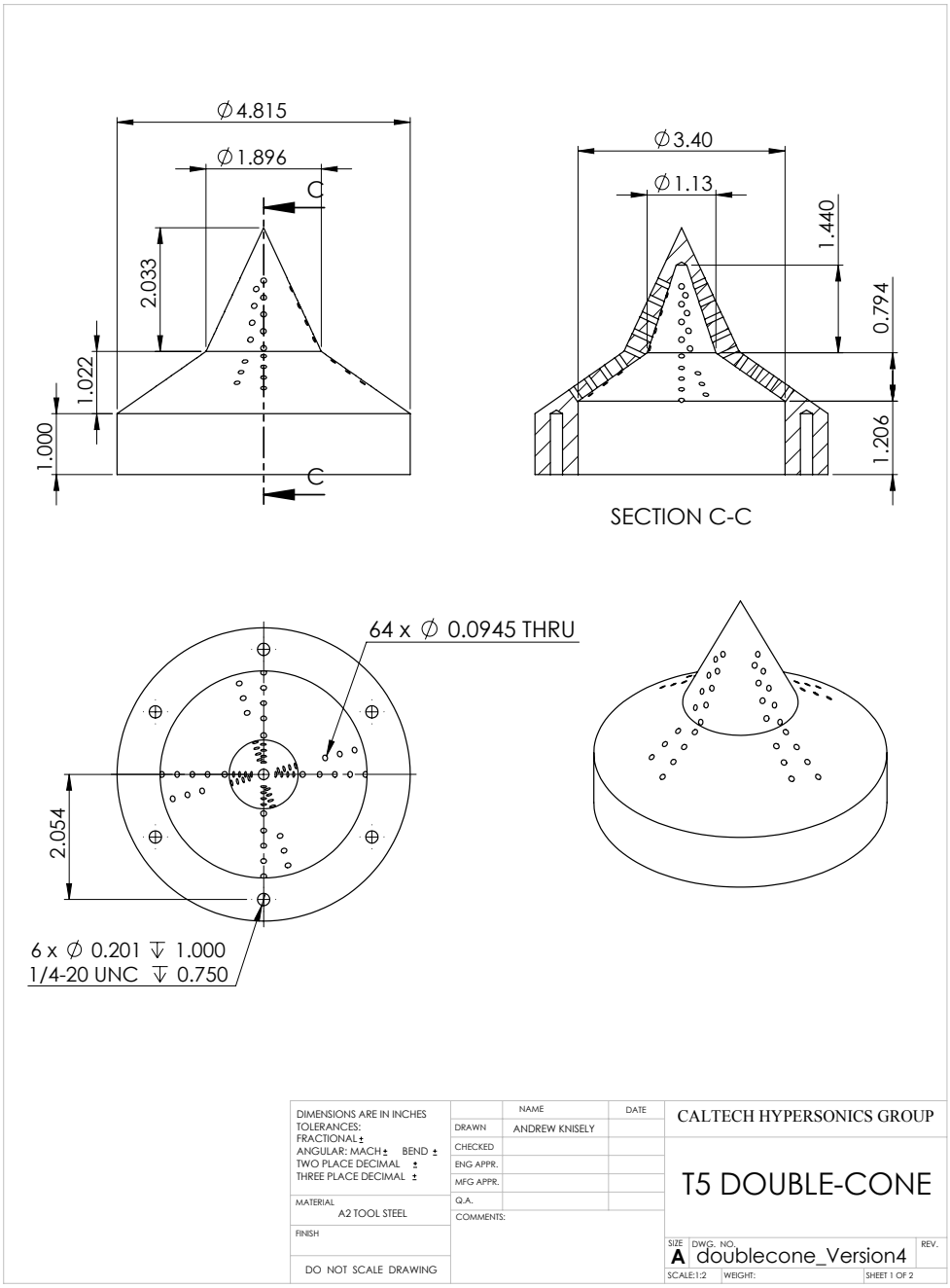

Figure C.1: T5 25-55 double-cone

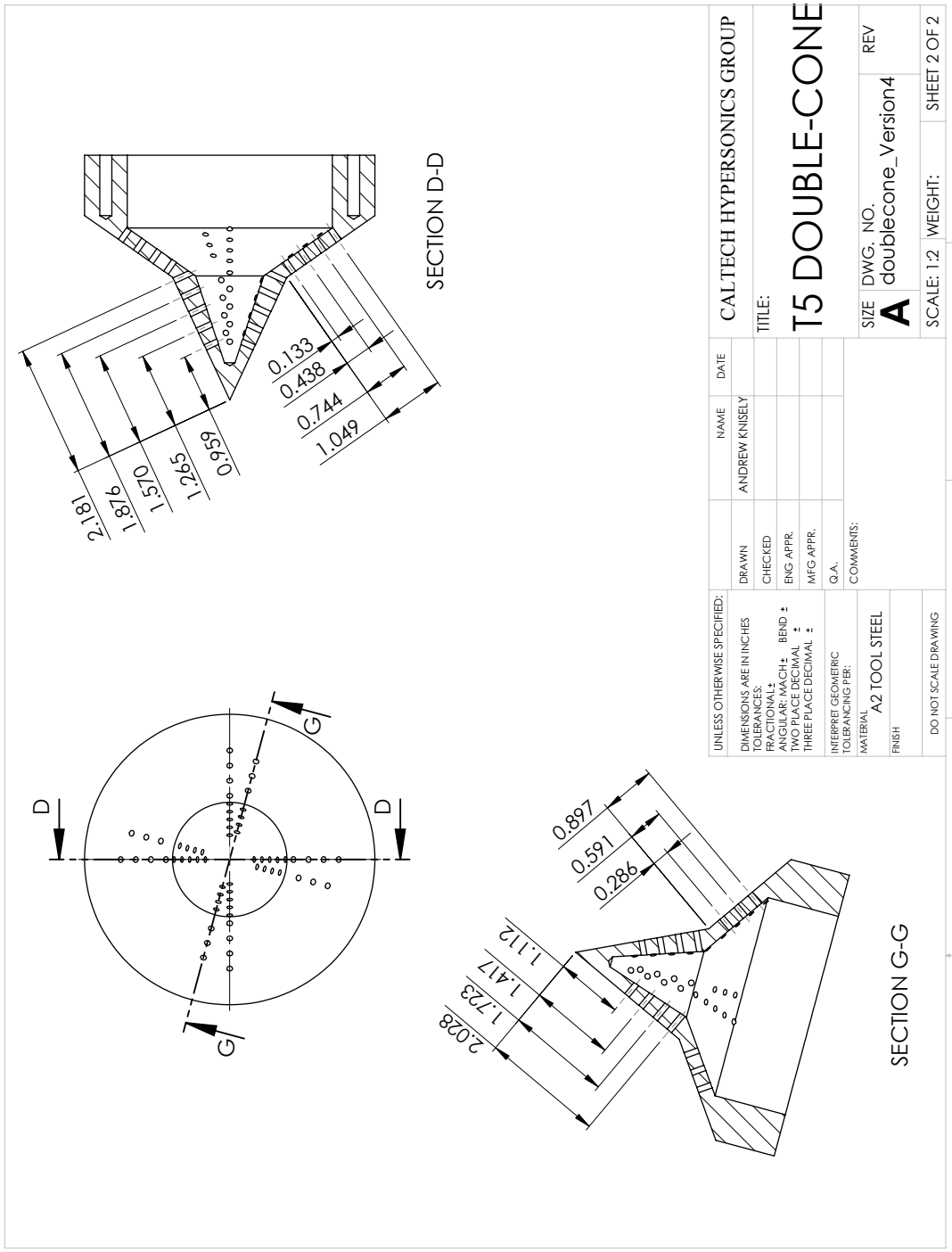

Figure C.2: T5 25-55 double-cone thermocouple hole locations

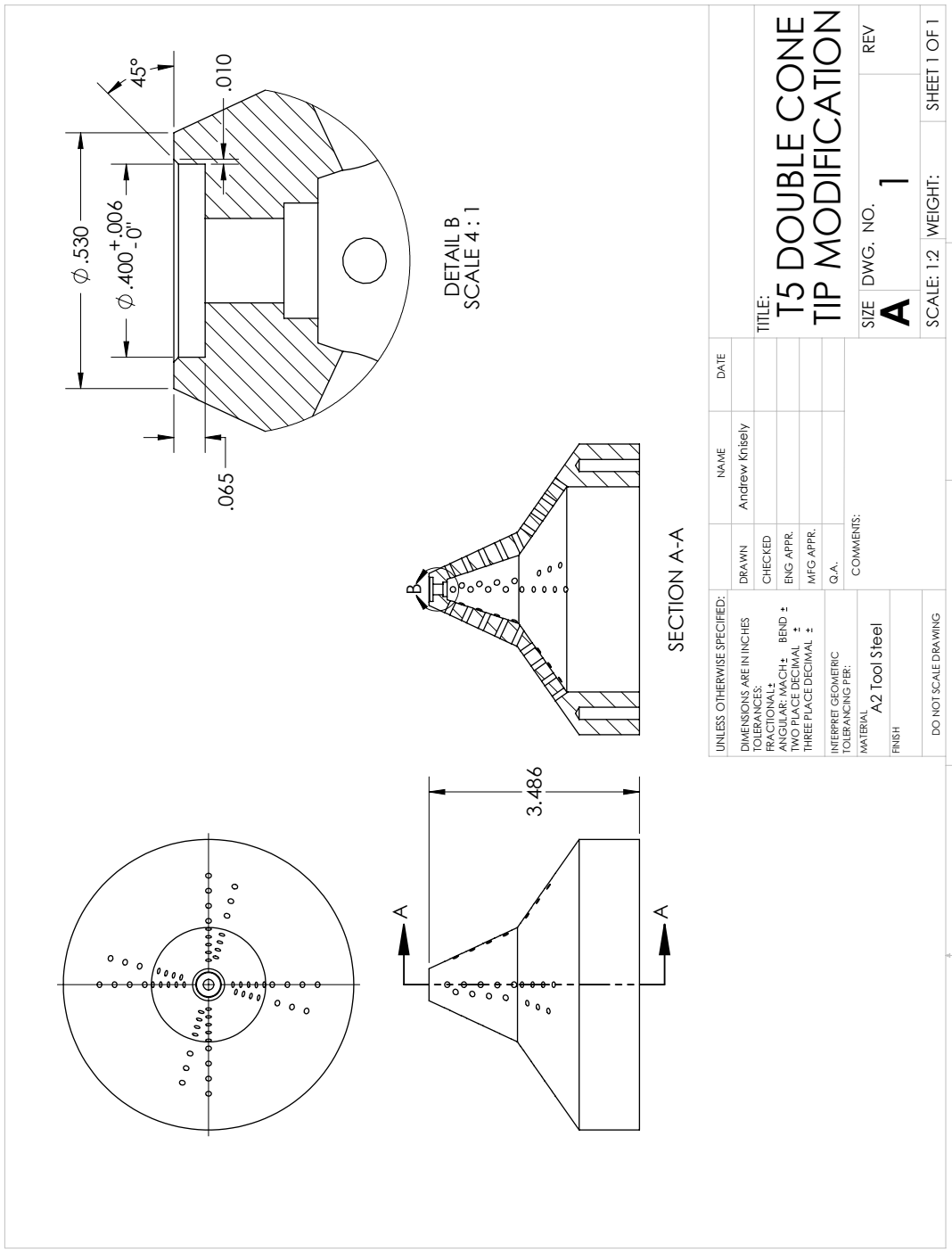

Figure C.3: T5 25-55 double-cone tip modification

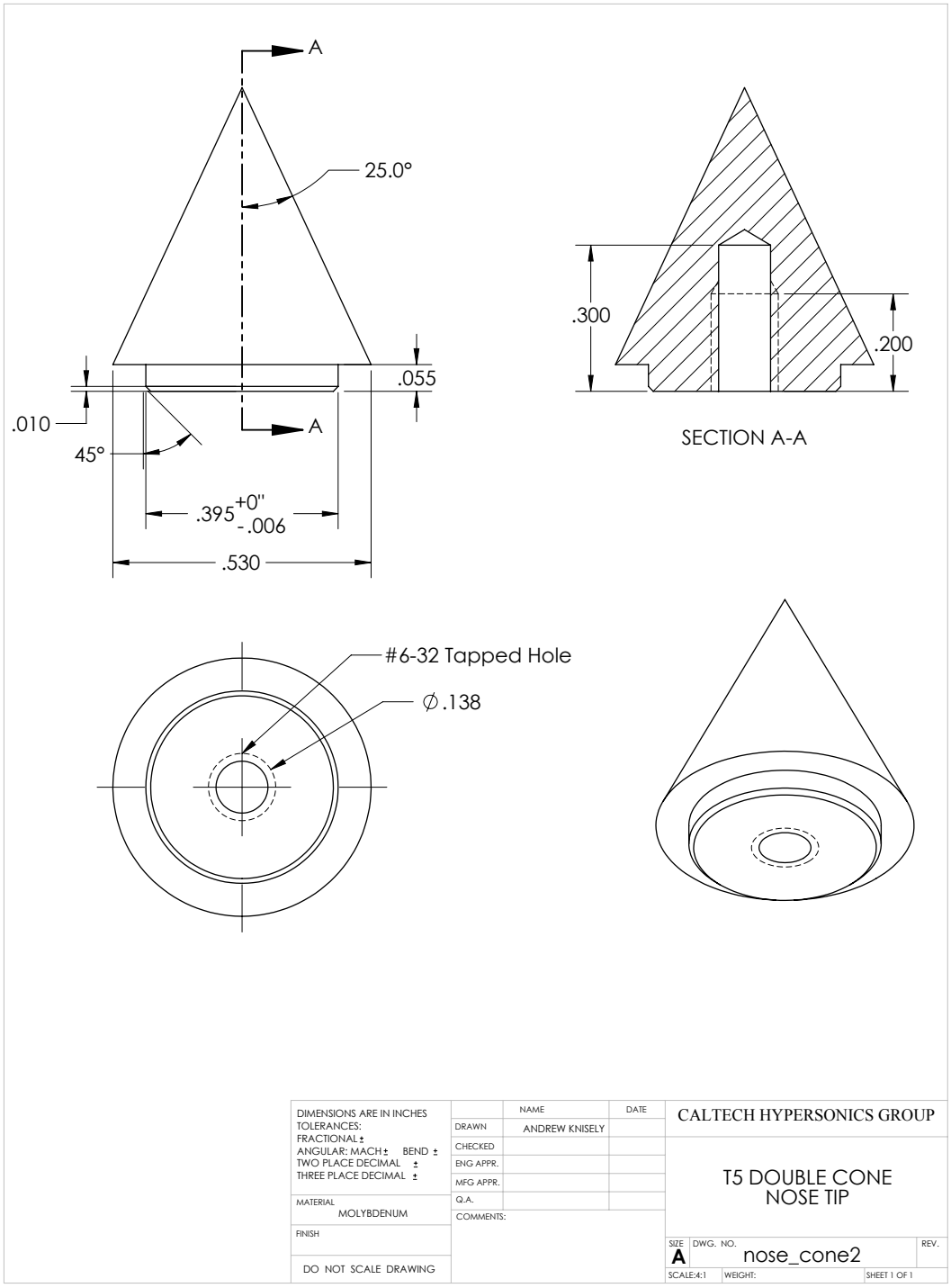

Figure C.4: T5 double-cone tip

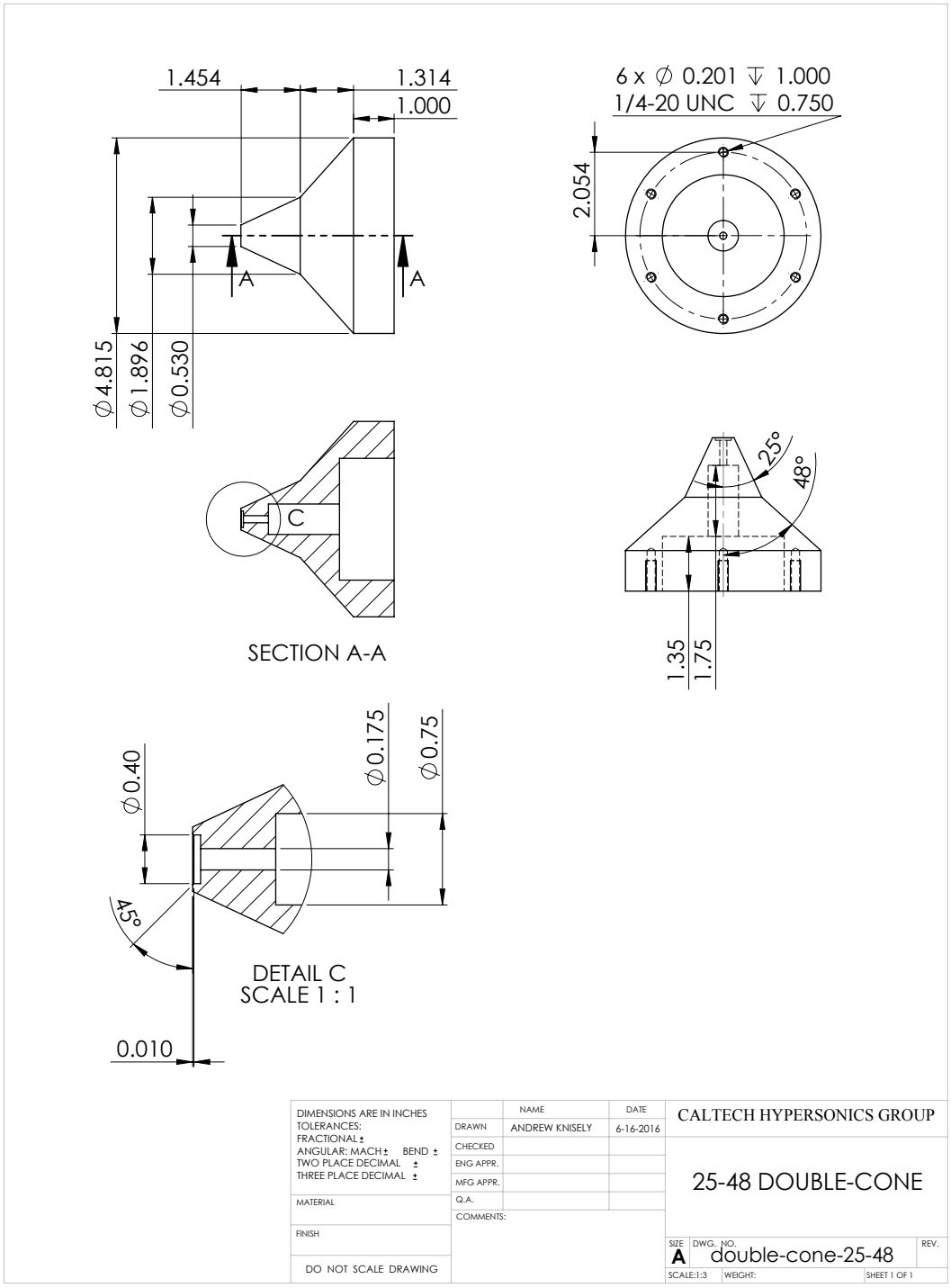

Figure C.5: T5 25-48 double-cone

REFERENCES

[1] Dolling, D. S., "Fifty Years of Shock-Wave/Boundary-Layer Interaction Research: What Next?" *AIAA Journal*, Vol. 39, No. 8, Aug. 2001, pp. 1517–1531.

[2] Gaitonde, D. V., Canupp, P. W., and Holden, M. S., "Heat Transfer Predictions in a Laminar Hypersonic Viscous/Inviscid Interaction," *Journal of Thermophysics and Heat Transfer*, Vol. 16, No. 4, Oct. 2002, pp. 481–489.

[3] Knight, D. and Longo, J., "Shock Interactions Investigations Associated with AVT-136," *Proceedings of the 48th AIAA Aerospace Sciences Meeting*, American Institute of Aeronautics and Astronautics, Jan. 2010.

[4] Davis, J.-P. and Sturtevant, B., "Separation length in high-enthalpy shock/boundary-layer interaction," *Physics of Fluids*, Vol. 12, No. 10, 2000, pp. 2661.

[5] Nompelis, I., Candler, G. V., and Holden, M. S., "Effect of Vibrational Nonequilibrium on Hypersonic Double-Cone Experiments," *AIAA Journal*, Vol. 41, No. 11, Nov. 2003, pp. 2162–2169.

[6] Nompelis, I., Candler, G., MacLean, M., Wadhams, T. P., and Holden, M. S., "Numerical Investigation of Double-Cone Flow Experiments with High-Enthalpy Effects," American Institute of Aeronautics and Astronautics, Jan. 2010.

[7] Druguet, M.-C., Candler, G. V., and Nompelis, I., "Effects of Numerics on Navier-Stokes Computations of Hypersonic Double-Cone Flows," *AIAA Journal*, Vol. 43, No. 3, March 2005, pp. 616–623.

[8] Olejniczak, J., Candler, G., Wright, M., Hornung, H., and Leyva, I., "High enthalpy double-wedge experiments," American Institute of Aeronautics and Astronautics, June 1996.

[9] Olejniczak, J., Candler, G., and Hornung, H., "Computation of Double-Cone Experiments in High Enthalpy Nitrogen," *32nd Thermophysics Conference*, American Institute of Aeronautics and Astronautics, June 1997.

[10] Bose, D. and Candler, G. V., "Thermal rate constants of the O2+N→NO+O reaction based on the $A^{2\prime}$ and $A^{4\prime}$ potential-energy surfaces," *The Journal of Chemical Physics*, Vol. 107, No. 16, Oct. 1997, pp. 6136–6145.

[11] Candler, G., Doraiswamy, S., and Kelley, J., "The Potential Role of Electronically-Excited States in Recombining Flows," American Institute of Aeronautics and Astronautics (AIAA), Jan. 2010.

[12] Edney, B. E., "Effects of shock impingement on the heat transfer around blunt bodies," *AIAA Journal*, Vol. 6, No. 1, Jan. 1968, pp. 15–21.

[13] Sanderson, S. R., *Shock wave interaction in hypervelocity flow*, Ph.D. thesis, California Institute of Technology, Pasadena, California, 1995.

[14] Olejniczak, J., Wright, M. J., and Candler, G. V., "Numerical study of inviscid shock interactions on double-wedge geometries," *Journal of Fluid Mechanics*, Vol. 352, 12 1997, pp. 1–25.

[15] Wright, M., Sinha, K., Olejniczak, J., Candler, G., Magruder, T., and Smits, A., "Numerical and experimental investigation of double-cone shock interactions," *AIAA Journal*, Vol. 38, No. 12, 2000, pp. 2268–2276.

[16] Jagadeesh, G., Hashimoto, T., Naitou, K., Sun, M., and Takayama, K., "Visualization of unsteady shock oscillations in the high-enthalpy flow field around double cones," *Journal of visualization*, Vol. 6, No. 2, 2003, pp. 195–203.

[17] Swantek, A. B., *The Role of Aerothermochemistry in Double Cone and Double Wedge Flows*, Ph.D. thesis, University of Illinois at Urbana-Champaign, 2012.

[18] Roshko, A., "Free shear layers, base pressure and bluff-body drag," Tech. rep., DTIC Document, 1993.

[19] Sychev, V. V., "Asymptotic theory of separation flows," *Fluid Dynamics*, Vol. 17, No. 2, 1982, pp. 179–188.

[20] Stewartson, K. and Williams, P. G., "Self-Induced Separation," *Proceedings of the Royal Society of London. Series A, Mathematical and Physical Sciences*, Vol. 312, No. 1509, Sept. 1969, pp. 181–206.

[21] Stewartson, K. and Williams, P. G., "On self-induced separation II," *Mathematika*, Vol. 20, No. 01, 1973, pp. 98–108.

[22] Rizzetta, D. P., Burggraf, O. R., and Jenson, R., "Triple-deck solutions for viscous supersonic and hypersonic flow past corners," *Journal of Fluid Mechanics*, Vol. 89, No. 03, 1978, pp. 535–552.

[23] Burggraf, O. R., "Asymptotic Theory of Separation and Reattachment of a Laminar Boundary Layer on a Compression Ramp," Tech. Rep. 168, AGARD, 1975.

[24] Kluwick, A., Gittler, P., and Bodonyi, R. J., "Viscous-inviscid interactions on axisymmetric bodies of revolution in supersonic flow," *Journal of Fluid Mechanics*, Vol. 140, 1984, pp. 281–301.

[25] Huang, M.-K. and Inger, G. R., "Application of the triple-deck theory of viscous-inviscid interaction to bodies of revolution," *Journal of Fluid Mechanics*, Vol. 129, 1983, pp. 427–441.

[26] Duck, P. W., "The effect of a surface discontinuity on an axisymmetric boundary layer," *The Quarterly Journal of Mechanics and Applied Mathematics*, Vol. 37, No. 1, 1984, pp. 57–74.

[27] Kluwick, A., Gittler, P., and Bodonyi, R. J., "Freely interacting axisymmetric boundary layers on bodies of revolution," *The Quarterly Journal of Mechanics and Applied Mathematics*, Vol. 38, No. 4, 1985, pp. 575–588.

[28] Gittler, P. and Kluwick, A., "Triple-deck solutions for supersonic flows past flared cylinders," *Journal of Fluid Mechanics*, Vol. 179, June 1987, pp. 469–487.

[29] Holden, M. S. and Moselle, J. R., "Theoretical and Experimental Studies of the Shock Wave-Boundary Layer Interaction on Compression Surfaces in Hypersonic Flow," Tech. Rep. ARL 70-0002, Aerospace Research Laboratories (ARR) Wright-Patterson AFB, Ohio 45433, Jan. 1970.

[30] Rudy, D. H., Thomas, J. L., Kumar, A., Gnoffo, P. A., and Chakravarthy, S. R., "Computation of laminar hypersonic compression-corner flows," *AIAA Journal*, Vol. 29, No. 7, July 1991, pp. 1108–1113.

[31] Lee, J. Y. and Lewis, M. J., "Numerical study of the flow establishment time in hypersonic shock tunnels," *Journal of Spacecraft and Rockets*, Vol. 30, No. 2, March 1993, pp. 152–163.

[32] Mallinson, S. G., Gai, S. L., and Mudford, N. R., "High-enthalpy, hypersonic compression corner flow," *AIAA Journal*, Vol. 34, No. 6, June 1996, pp. 1130–1137.

[33] Mallinson, S. G., Gai, S. L., and Mudford, N. R., "The interaction of a shock wave with a laminar boundary layer at a compression corner in high-enthalpy flows including real gas effects," *Journal of fluid mechanics*, Vol. 342, 1997, pp. 1–35.

[34] Swantek, A. B. and Austin, J. M., "Flowfield Establishment in Hypervelocity Shock-Wave/Boundary-Layer Interactions," *AIAA Journal*, Sept. 2014, pp. 1–10.

[35] Dufrene, A., Sharma, M., and Austin, J. M., "Design and Characterization of a Hypervelocity Expansion Tube Facility," *Journal of Propulsion and Power*, Vol. 23, No. 6, Nov. 2007, pp. 1185–1193.

[36] Hornung, H., "Performance data of the new free-piston shock tunnel at GALCIT," *28th Joint Propulsion Conference and Exhibit*, American Institute of Aeronautics and Astronautics (AIAA), July 1992.

[37] Jewell, J. S., *Boundary-layer transition on a slender cone in hypervelocity flow with real gas effects*, Ph.D. thesis, California Institute of Technology, 2014.

[38] Goodwin, D. G., Moffat, H. K., and Speth, R. L., "Cantera: An object-oriented software toolkit for chemical kinetics, thermodynamics, and transport processes. Version 2.1.1," 2014, available at http://www.cantera.org.

[39] Browne, S., Ziegler, J., and Shepherd, J. E., "Numerical Solution Methods for Shock and Detonation Jump Conditions," Tech. rep., California Institute of Technology, Pasadena, CA, July 2008, GALCIT Report FM2006.006.

[40] Candler, G., "Hypersonic Nozzle Analysis Using an Excluded Volume Equation of State," *38th AIAA Thermophysics Conference*, American Institute of Aeronautics and Astronautics (AIAA), June 2005.

[41] Spalart, P. and Allmaras, S., "A one-equation turbulence model for aerodynamic flows," *30th Aerospace Sciences Meeting and Exhibit*, American Institute of Aeronautics and Astronautics (AIAA), Jan. 1992.

[42] Catris, S. and Aupoix, B., "Density corrections for turbulence models," *Aerospace Science and Technology*, Vol. 4, No. 1, 2000, pp. 1–11.

[43] Steger, J. L. and Warming, R., "Flux vector splitting of the inviscid gasdynamic equations with application to finite-difference methods," *Journal of computational physics*, Vol. 40, No. 2, 1981, pp. 263–293.

[44] Liou, M.-S. and Van Leer, B., *Choice of implicit and explicit operators for the upwind differencing method*, National Aeronautics and Space Administration, 1988.

[45] Wright, M. J., Candler, G. V., and Bose, D., "Data-Parallel Line Relaxation Method for the Navier-Stokes Equations," *AIAA Journal*, Vol. 36, No. 9, Sept. 1998, pp. 1603–1609.

[46] Flaherty, W. P., *Experimental surface heat flux measurement in hypervelocity flows*, Ph.D. thesis, University of Illinois at Urbana-Champaign, 2010.

[47] Davis, J.-P., *High-enthalpy shock/boundary-layer interaction on a double wedge*, Ph.D. thesis, California Institute of Technology, 1999.

[48] Sundqvist, B., "Thermal diffusivity and thermal conductivity of Chromel, Alumel, and Constantan in the range 100–450 K," *Journal of Applied Physics*, Vol. 72, No. 2, 1992, pp. 539–545.

[49] "Specification and Temperature-Electromotive Force (EMF) Tables for Standardized Thermocouples," Standard ASTM-E230, ASTM International, 2009.

[50] Parziale, N. J., Schmidt, B. E., Damazo, J. S., Wang, P. S., Hornung, H. G., and Shepherd, J. E., "Pulsed Laser Diode for use as a Light Source for Short-Exposure, High-Frame-Rate Flow Visualization," *53rd AIAA Aerospace Sciences Meeting. AIAA*, 2015.

[51] Marineau, E. and Hornung, H., "High-Enthalpy Nonequilibrium Nozzle Flow of Air: Experiments and Computations," *39th AIAA Fluid Dynamics Conference*, American Institute of Aeronautics and Astronautics (AIAA), June 2009.

[52] Bertin, J. J. and Hinkle, J. C., "Experimental Investigation of Supersonic Flow Past Double-Wedge Configurations," *AIAA Journal*, Vol. 13, No. 7, July 1975, pp. 897–901.

[53] Schneider, C. A., Rasband, W. S., and Eliceiri, K. W., "NIH Image to ImageJ: 25 years of image analysis," *Nature Methods*, Vol. 9, No. 7, July 2012, pp. 671–675.

[54] Wen, C.-Y. and Hornung, H., "Non-equilibrium dissociating flow over spheres," *Journal of Fluid Mechanics*, Vol. 299, 1995, pp. 389–405.

[55] Leyva, I. A., *Shock detachment process on cones in hypervelocity flows*, Ph.D. thesis, California Institute of Technology, 1999.

[56] Hornung, H. G., Schramm, J. M., and Hannemann, K., *Sonic Line and Stand–Off Distance on Re–entry Capsule Shapes*, Springer Berlin Heidelberg, Berlin, Heidelberg, 2012, pp. 605–611.

[57] Gupta, R. N., Yos, J. M., Thompson, R. A., and Lee, K.-P., "A review of reaction rates and thermodynamic and transport properties for an 11-species air model for chemical and thermal nonequilibrium calculations to 30000 K," Aug.

[58] Anderson, Jr, J. D., *Hypersonic and High-Temperature Gas Dynamics*, American Institute of Aeronautics and Astronautics, Inc., 1801 Alexander Bell Drive, Reston,, Virginia 20191-4344, 2nd ed., 2006.

[59] Meador, W. E. and Smart, M. K., "Reference Enthalpy Method Developed from Solutions of the Boundary-Layer Equations," *AIAA Journal*, Vol. 43, No. 1, Jan. 2005, pp. 135–139.

[60] Eckert, E. R. G., "Engineering relations for friction and heat transfer to surfaces in high velocity flow," *Journal of the Aeronautical Sciences*, Vol. 22, No. 8, 1955, pp. 585–587.

[61] Dorrance, W. H., *Viscous Hypersonic Flow*, McGraw–Hill, New York, 1962.

[62] Hayne, M. J., Mee, D. J., Gai, S. L., and McIntyre, T. J., "Boundary layers on a flat plate at sub-and superorbital speeds," *Journal of Thermophysics and Heat Transfer*, Vol. 21, No. 4, 2007, pp. 772–779.

[63] Young, G. B. W. and Janssen, E., "The Compressible Boundary Layer," *Journal of the Aeronautical Sciences (Institute of the Aeronautical Sciences)*, Vol. 19, No. 4, April 1952, pp. 229–236.

[64] Ott, J. D. and Anderson, J. D., "Effects of nonequilibrium chemistry on the reference temperature method and Reynolds analogy," *Journal of thermophysics and heat transfer*, Vol. 8, No. 2, 1994, pp. 381–384.

[65] Anderson, J. D., *Modern Compressible Flow: With Historical Perspective*, McGraw-Hill series in aeronautical and aerospace engineering, McGraw-Hill, Boston, 2003.

[66] White, F. M., *Viscous fluid flow*, McGraw-Hill series in mechanical engineering, McGraw-Hill, New York, 1991.

[67] White, F. M. and Christoph, G. H., "A Simple Theory for the Two-Dimensional Compressible Turbulent Boundary Layer," *Journal of Basic Engineering*, Vol. 94, No. 3, 1972, pp. 636.

[68] Van Driest, E., "The problem of aerodynamic heating," *Aeronautical Engineering Review*, Vol. 15, No. 10, 1956, pp. 26–41.

[69] Johnson, H. and Candler, G., "Hypersonic Boundary Layer Stability Analysis Using PSE-Chem," *35th AIAA Fluid Dynamics Conference and Exhibit*, American Institute of Aeronautics and Astronautics (AIAA), June 2005.

[70] Glick, H. S., "Modified Crocco-Lees Mixing Theory for Supersonic Separated and Reattaching Flows," *Journal of the Aerospace Sciences*, Vol. 29, No. 10, 1962, pp. 1238–1249.

[71] Lighthill, M. J., "On Boundary Layers and Upstream Influence. II. Supersonic Flows without Separation," *Proceedings of the Royal Society of London. Series A, Mathematical and Physical Sciences*, Vol. 217, No. 1131, May 1953, pp. 478–507.

[72] Lees, L., "Laminar Heat Transfer Over Blunt-Nosed Bodies at Hypersonic Flight Speeds," *Journal of Jet Propulsion*, Vol. 26, No. 4, April 1956, pp. 259–269.

[73] Needham, D. and Stollery, J., "Boundary layer separation in hypersonic flow," *3rd and 4th Aerospace Sciences Meeting*, American Institute of Aeronautics and Astronautics (AIAA), Jan. 1966.

[74] Taylor, G. I. and Maccoll, J. W., "The Air Pressure on a Cone Moving at High Speeds. I," *Proceedings of the Royal Society of London A: Mathematical, Physical and Engineering Sciences*, Vol. 139, The Royal Society, 1933, pp. 278–297.

[75] Birch, S. F. and Keyes, J. W., "Transition in Compressible Free Shear Layers," *Journal of Spacecraft and Rockets*, Vol. 9, No. 8, Aug. 1972, pp. 623–624.

[76] King, R. A., Creel, T. R., and Bushnell, D. M., "Experimental Transition Investigation of a Free-Shear Layer Above a Cavity at Mach 3.5," *Journal of Propulsion and Power*, Vol. 7, No. 4, July 1991, pp. 626–634.